

“Tumor Necrosis Factor Superfamily 14 drives the depletion of tissue-resident alveolar macrophages upon influenza A virus infection enabling the establishment of secondary pneumococcal pneumonia”

Inaugural dissertation
submitted to the Faculty of Medicine
in partial fulfillment of the requirements
for the PhD-Degree
of the Faculties of Veterinary Medicine and Medicine
of the Justus Liebig University Giessen

by
Malainou, Christina
of
Amarousio, Greece

Giessen, October 12th, 2023

From the Department of Medicine V, Infectious Diseases and Infection Control
of the Faculty of Medicine of the Justus Liebig University Giessen

Director: Prof. Dr. med. Susanne Herold, PhD

Chair: Prof. Dr. Martin Diener

Vice-chair and Co-Supervisor: Prof. Dr. Friedemann Weber

First Reviewer and Supervisor: Prof. Dr. med. Susanne Herold, PhD

Second Reviewer: Prof. David Dockrell

Date of Doctoral Defense: 12th October 2023

Table of Contents

1. Introduction	7
Lung microanatomy and physiology	7
Pulmonary physiology and development	7
Alveolar structure	7
Development of the lung-resident macrophage pool	8
Concepts of macrophage ontogeny	8
Alveolar macrophage development	10
Alveolar macrophage characterization	11
Acute Respiratory Distress Syndrome (ARDS)	12
Influenza A virus	15
Taxonomy and structure	16
Antigen drift and antigen shift	17
Transmission and viral replication	17
Initiation of intracellular anti-viral mechanisms	19
Inflammatory response to IV infection	19
TR-AM	19
Immune cell recruitment	20
Viral clearance and return to homeostasis	22
IV infection clinical course, treatment, and vaccination	23
Post-influenza bacterial infection	24
Cell death and death-inducing ligands	26
TNFSF and IV infection	29
TNFSF14/LIGHT	30
2. Aims of this work	33

3. Methods.....	34
Mouse strains.....	34
Cell culture	35
Cell lines.....	35
Primary alveolar macrophages	35
Influenza A virus propagation and titration	35
<i>In vivo</i> experiments and preparation of animal-derived samples	37
Influenza A virus and secondary <i>Streptococcus pneumoniae</i> infection.....	37
Orotracheal administration of recombinant tnfsf14/light.....	38
Adoptive transfer of TR-AM and co-infection experiments	38
Caspase inhibitor and neutralizing antibody treatment	39
Preparation of BALF and lung tissue single-cell suspension for further analyses.....	39
Preparation of BALF for cytokine and cell composition flow cytometry analysis.....	39
Calculation of absolute cell numbers in mouse BALF	40
Preparation of lung tissue single-cell suspension for cell composition analysis.....	40
Calculation of bacterial burden in the lungs of animals infected with IAV and <i>Streptococcus pneumoniae</i>	41
Fluorescence activated cell sorting (FACS) of BALF TR-AM	41
<i>In vitro</i> experiments	42
In vitro infection and ultraviolet light (UV) treatment of cultured MDCK II cells	42
Concentration of BALF from naïve and infected mice for ex vivo treatment of TR-AM.....	42
Viability analysis of ex vivo treated alveolar macrophages.....	42
Caspase activity assays.....	43
Analysis of gene expression.....	44
RNA isolation, cDNA synthesis, and quantitative polymerase chain reaction (qPCR).....	44

RT ² Profiler PCR Arrays.....	45
Single-cell RNA sequencing experiments.....	46
Analysis of protein expression	47
Enzyme Linked Immunosorbent Assay (ELISA) and Multiplex Assay	47
Flow cytometry analysis of immune cell populations in the BALF and in lung tissue single-cell suspension.....	48
Phagocytosis assay	49
Microscopy	50
Fixation and preparation of lung tissue for hematoxylin-and-eosin (HE) staining and histological analysis	50
Immunohistochemistry of lung tissue	51
Human samples	52
Statistics	52
4. Results	53
Pre-existing influenza A virus (IAV) infection enables the establishment of secondary pneumococcal pneumonia.....	53
IAV-induced pneumonia is characterized by the depletion of the TR-AM pool and the intra-alveolar influx of recruited immune cells at distinct time points over the infection course	54
Apoptosis drives TR-AM death upon IAV-induced pneumonia and is largely independent of direct viral infection	59
Post-influenza TR-AM depletion can be attenuated by the use of specific caspase inhibitors..	63
Tnfsf14/Light and its receptors are upregulated in the murine lung upon IAV-induced pneumonia	65
Tnfsf14/Light drives TR-AM depletion upon IAV-induced pneumonia and TR-AM loss can be abrogated through genetic deletion or therapeutic targeting of the ligand.....	71
Neutrophils are the main cellular source of tnfsf14/light upon IAV infection and neutrophil depletion attenuates TR-AM loss	83

Tnfsf14/Light exerts its pro-apoptotic effect on TR-AM mainly via the $l\beta r$ receptor following IAV infection.....	89
Loss of tnfsf14/light improves clinical outcome following post-IAV pneumococcal pneumonia	91
5. Discussion	94
6. Summary	101
7. Zusammenfassung.....	103
8. References	104
9. Supplement.....	118
List of Figures	118
Materials.....	120
Chemicals and consumables.....	120
Reaction kits	122
Enzymes, recombinant proteins, and inhibitors	122
Antibodies	123
ELISA and Multiplex kits	124
Affirmation.....	133
Curriculum vitae.....	134
Acknowledgements	135

1. Introduction

Lung microanatomy and physiology

Pulmonary physiology and development

The main challenge aerobic life is faced with is the continuous supply of tissues with oxygen. Unlike fuels, carbohydrates, or fat, which can be stored in the liver, in the fatty tissue, or within the cytoplasm itself, oxygen has to be continuously supplied to the mitochondria, proportionally to the needs of the cells at any given moment [1]. In higher organisms, including humans, this procedure involves taking in oxygen from environmental air through the alveoli, binding it to the hemoglobin of circulating erythrocytes, and finally transporting it to all cells of the organism via the cardiovascular system [1]. At the same time, CO₂, a by-product of the energy-generating Krebs cycle, gets eliminated from the body, following the opposite route [1].

The coordination of such a complex procedure requires a large exchange surface, where air and blood can come in close-to-immediate contact [2]. In mammals, reptiles, and amphibians, this task is undertaken by the alveolar lung structure, where air moves in a large area of parenchyma, driven by the movement of the chest and the diaphragm [1]. The alveolar lung can thus be divided into two categories: the proximal, or conducting zone, and the distal, or respiratory zone. While the first one involves bronchi, arteries and veins, the latter consists of the cul-de-sac-shaped gas exchange units, the alveoli, where air can be directly exposed to blood [1]. A versatile connective tissue scaffold provides mechanical support and connectivity throughout the continuum of the respiratory tree [1, 2].

Alveolar structure

Two continuous cell layers, the alveolar epithelium and the capillary endothelium, comprise the air-blood barrier, being supported by an interstitial space of varying composition. Around 95% of the total 220,000µm² of alveolar surface in humans is covered by the thin cytoplasmic leaflets of type I epithelial cells. These cells are responsible for oxygen uptake and diffusion to capillary endothelial cells [3, 4]. A shared basal lamina separates type I epithelial cells from endothelial cells, creating the blood-air barrier [5]. Approximately twice as many type II epithelial cells complete the mosaic of the alveolar epithelium. These cuboidal cells are filled with secretory granules of the phospholipid surfactant component (known as lamellar bodies) and an endoplasmic

reticulum, where surfactant apoproteins are produced [3]. Surfactant production is pivotal to homeostasis maintenance. Not only does surfactant reduce surface tension during respiratory movements, but surfactant-associated proteins such as surfactant protein -A (SP-A) and SP-D are also known to possess antimicrobial properties. Various soluble factors which are found in the airway fluid further contribute to the establishment of this primary line of defense. These factors involve mucins, lysozyme, lactoferrin, the immunoglobulins A and G, and defensins [6-8].

Stromal cells migrate within the interstitium of the alveolar septum, where they differentiate into lipofibroblasts, myofibroblasts, pericytes, or commit to other lineages [5]. Through the production of collagen and elastic fibers they remain in close contact both with the alveolar epithelium and with the capillaries, providing mechanical support and nutritional factors [3, 5]. Tissue-resident alveolar macrophages (TR-AM) complete the cellular composition of the gas exchange unit, serving as an intermediate sentinel between the outside world and the distal lung parenchyma.

Development of the lung-resident macrophage pool

Concepts of macrophage ontogeny

Several studies over the last years have focused on the development of the mononuclear phagocyte system. This is a gradual, multi-stage process, which starts during embryonic life and continues over adulthood. It is currently understood that mammalian embryonic hematopoiesis occurs in successive waves, which lead to the acquisition of erythroid, myeloid, and lymphoid lineage progenitors in a sequential manner [9-11].

In mice, the first wave of hematopoiesis (*primitive hematopoiesis*) begins at embryonic day E7.25 within the blood islands of the extra-embryonic yolk sac (YS). This leads to the production of primitive erythroblasts, megakaryocytes, and macrophages [9, 12]. Erythro-myeloid precursors (EMPs) develop within the YS during the second wave of hematopoiesis (E8.0 to E8.5, *transient definitive hematopoiesis*). These EMPs give rise to YS macrophages locally or migrate to the fetal liver upon establishment of blood circulation (E9.5) [9, 13]. Almost concomitantly with their emergence, immature progenitors arise in the para-aortic splanchnopleura (P-Sp) region, which eventually give rise to mature fetal hematopoietic stem cells (HSC) in the aorta, gonads, and mesonephros regions at E10.5 [9, 12, 14-16]. During the third wave of hematopoiesis (*definitive hematopoiesis*), these progenitors colonize the fetal liver, which becomes the main hematopoietic organ during embryonic life from E12.5 onward [9, 17]. Progenitors from the P-Sp region seed the

bone marrow from E17.5 onward and eventually give rise to adult HSC, which will continue to seed the blood stream with monocytes/macrophages throughout adult life (**Figure 1**) [13].

Depending on their emergence during the time course of organ development, tissue-resident macrophages differ regarding their embryonic origin. Microglia, for instance, derives from YS macrophages, whereas Langerhans cells present a mixed contribution of YS and fetal liver macrophages [13]. Alveolar macrophages and Kupffer cells, in contrast, arise mostly from fetal liver monocytes [9, 13]. Tissues that display a constant accessibility of the local macrophage niche from the blood stream such as the heart, pancreas, dermis, and gut, are seeded with bone marrow-derived monocytes [9, 13]. Although macrophage precursors share an almost identical potential of giving rise to resident macrophages, precursor timing, niche availability and accessibility, as well as tissue-specific signals, determine the origin of distinct macrophage populations [13, 18, 19].

In contrast to murine findings, the specific progenitors of human alveolar macrophages still remain largely unknown. Post-natal alveolar niche establishment and the presence of the granulocyte-macrophage colony-stimulating factor (GM-CSF or CSF2) have, however, been shown to be the prerequisites for TR-AM development [16]. Alveolar macrophages can be detected in the alveoli approximately 48h after birth, thus implying that oxygen intake is required for their maturation [16].

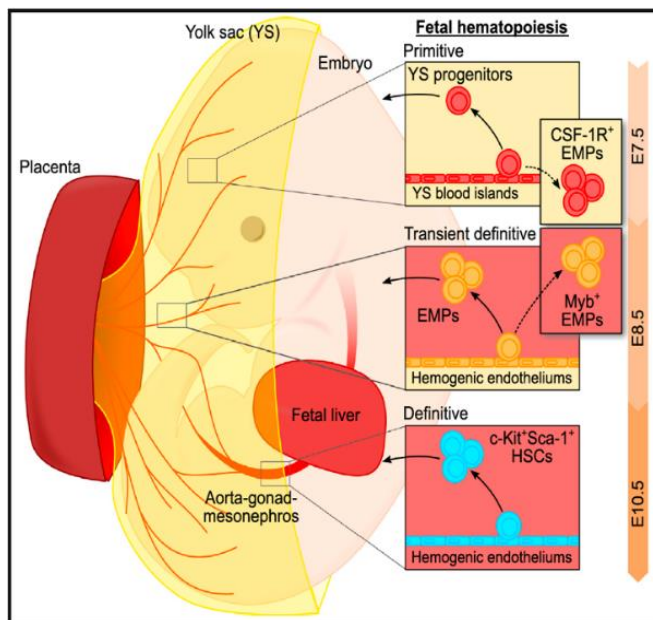


Figure 1. Depiction of the successive waves of fetal hematopoiesis. Primitive hematopoiesis begins at E7.25 in the extra-embryonic yolk sac (YS). Erythromyeloid precursors give rise to YS macrophages during the second wave of hematopoiesis (E8.0 to E8.5) or migrate to the fetal liver (E9.5). During the third wave (E8.5-E10.5) immature hematopoietic stem cells colonize the fetal liver and bone marrow. Embryonic progenitors from the fetal liver migrate to the lung and give rise to tissue-resident alveolar macrophages post-partum. Ginhoux and Guilliams, 2016, reproduced with permission of Elsevier [20].

Alveolar macrophage development

Fetal liver-derived monocytes that seed the mouse lung around the time of alveolar development (E18.5) differentiate after birth into TR-AM within the course of one week. A well-defined transcriptional program involving transcription factors such as PU.1, V-maf musculoaponeurotic fibrosarcoma oncogene homolog (c-Maf), myeloblastosis proto-oncogene (Myb), and proto-oncogene tyrosine-protein kinase MER (Mertk), orchestrates the commitment of these monocytes to the macrophage lineage [21].

GM-CSF is the driving force behind TR-AM differentiation and development. Its production has been traditionally linked to alveolar type II epithelial cells. Recent studies have highlighted the role of innate lymphoid cells (ILC) and basophils as additional GM-CSF sources [16, 17, 22, 23]. GM-CSF instructs monocyte differentiation into macrophages through activation of peroxisome proliferator-activated receptor γ (PPAR- γ), a nuclear receptor involved in the regulation of cholesterol metabolism, fatty acid β -oxidation, as well as lipid transport, storage, and degradation [16, 21, 24]. Mice lacking GM-CSF (*Csf2*^{-/-}) or the GM-CSF receptor (*Csf2rb*^{-/-}) fail to drive monocyte commitment towards TR-AM differentiation. Their alveolar niche consists of only a few dysfunctional alveolar macrophages [13, 25]. *Ppar- γ* ^{-/-} mice present a similar phenotype, with TR-AM differentiation being arrested at an immature stage or completely abrogated [26]. Alveoli of these mice present abnormally enlarged TR-AM containing a plead of lipids, pointing out the deficit of these cells in surfactant catabolism [24]. In humans, mutations in the genes encoding GM-CSF receptor chains or the presence of autoantibodies against GM-CSF cause severe pulmonary alveolar proteinosis (PAP) [13]. This condition is characterized by an abundance of surfactant within the alveoli, leading to impaired gas exchange and increased susceptibility to infection [27].

Other factors that regulate TR-AM development and differentiation involve the B lymphoid transcriptional repressor broad complex tramtrack bric-à-brac and Cap'n'collar homology 2 (BACH2), which controls lipid and cholesterol metabolism in mature TR-AM [24, 28], and the transforming growth factor β (TGF- β), which supports TR-AM development and homeostasis in an autocrine manner [16]. Furthermore, low levels of colony-stimulating factor 1 (M-CSF or *Csf1*) are required for TR-AM survival, whereas higher levels support their proliferation [19]. Recent findings further support the role of the zinc finger E box binding homeobox 2 transcription factor (ZEB2) in the

establishment of tissue-specific macrophage identity and continued macrophage presence over time [29].

Alveolar macrophage characterization

TR-AM constitute the major leukocyte population in the lung during homeostatic conditions [30]. In contrast to interstitial macrophages, which are located in the interstitium connecting the alveolar epithelium with blood vessels, or the recently described nerve- and airway-associated macrophages, which reside in close proximity to the sympathetic nerves of the bronchovascular bundle, TR-AM are strategically placed within the alveolar space [16, 24, 31-34]. Though detected approximately once every three alveoli, they can migrate between adjacent alveoli through the pores of Kohn [24, 35]. Their unique position establishes TR-AM as sentinels for tissue homeostasis, constantly responding to physiological and environmental fluctuations [36].

Morphologically, TR-AM are large, vacuolar cells, with an increased cytoplasm/nucleus ratio, and prominent pseudopodia, adapted to the phagocytosis of cellular debris, senescent cells, and pathogens [10, 37, 38]. Their secretory profile involves lysozymes, proteinases, chemokines, pro- and anti-inflammatory cytokines, arachidonate, growth factors, oxygen, and nitric oxide (NO) derivatives [7, 39]. They express a variety of membrane and cytosolic receptors, such as toll-like receptors, pathogen-associated molecular pattern (PAMP) and danger-associated molecular pattern (DAMP) receptors, nucleotide-binding oligomerization domain-containing protein (NOD)-like receptors, and retinoic acid inducible gene-1 (RIG-I)-like helicases at relatively high levels, which enables them to initiate a strong immune response, if necessary [37, 39, 40]. Inhaled particles and potential pathogens are recognized by the mannose receptor cluster of differentiation 206 (CD206) and the β -glucan specific receptor dectin-1, leading to their removal from the alveolar space [37]. TR-AM are further characterized by high expression levels of scavenger macrophage receptor with collagenous structure (MARCO), integrin CD11c, and sialic-acid binding lectin SiglecF, as opposed to low expression levels of the phagocytic receptor CD11b and pattern recognition receptor CD14. This characteristic phenotype not only separates TR-AM from other tissue-resident macrophage populations, but also enables the identification of TR-AM among other lung leukocyte cell populations [16, 25, 30, 37].

Like most resident macrophages, TR-AM are equipped with a mild stem cell-like proliferation capacity, which enables their self-maintenance without the contribution of bone marrow-derived

macrophages (BMDM) during homeostasis [16, 19, 30, 41]. However, proliferation rates are normally rather low, as TR-AM are long-lived cells (40% turnover rate over one year) [31]. This pattern can be abrogated upon injury and depletion of the TR-AM pool, which is subsequently replenished through the combination of local proliferation and input of circulating BMDM, depending on the nature and degree of injury [16, 30]. BMDM, which present a more pro-inflammatory phenotype, progressively outcompete TR-AM with every new injurious event (**Figure 2**) [42]. Parallel to that, a gradual decrease in total TR-AM numbers can be observed with aging [16]. This has a significant impact on host defense, which may partially explain the higher severity of lung infection or injury observed in the elderly population [43, 44].

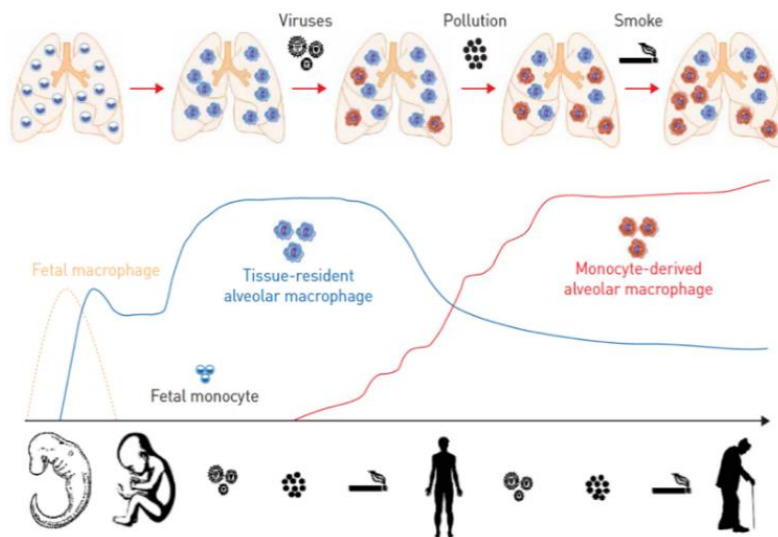


Figure 2. Composition of the TR-AM pool during life. Fetal-derived monocytes give rise to TR-AM over the first days of life. During steady state, TR-AM are preserved due to their long half-life and self-renewal capacity but decrease over time following different types of injury. BMDM are then recruited, creating an alveolar macrophage mosaic through an individual's lifespan. Morales-Nebreda et al., 2015, reproduced with permission of the European Respiratory Society 2022 [33].

Acute Respiratory Distress Syndrome (ARDS)

Originally defined in 1967, Acute Respiratory Distress Syndrome (ARDS) describes respiratory failure within one week of a known insult, or new and/or worsening respiratory symptoms, according to the current, 'Berlin' definition (established in 1992, revised in 2012) [45, 46]. This failure cannot be fully explained by cardiac function or volume overload, and it involves bilateral opacities on chest radiograph or computer tomography, which cannot be fully explained by effusion, collapse, or nodules linked to cardiac failure [45, 46].

ARDS is characterized by the acute onset of arterial hypoxemia, which is the joint result of ventilation-to-perfusion mismatch and right-to-left intrapulmonary shunting [45, 47]. The severity

of hypoxemia can be estimated using the ratio of arterial oxygen concentration in the blood divided by the inspired oxygen fraction ($\text{PaO}_2/\text{FiO}_2$), which in ARDS patients is lower than 300 on a minimum of 5cm H_2O positive end-expiratory pressure (PEEP) [45-47]. Based on the value of this fraction, ARDS can be further divided into mild ($\text{PaO}_2/\text{FiO}_2$ 201-300), moderate ($\text{PaO}_2/\text{FiO}_2$ 101-200), and severe ($\text{PaO}_2/\text{FiO}_2 < 100$) [45, 46]. Following a different classification, ARDS can be divided into a hyperinflammatory (30%) and a hypoinflammatory (70%) subphenotype. This classification depends on the levels of inflammatory biomarkers and protein C in the plasma, metabolic acidosis prevalence, as well as the need for vasopressor drugs [45, 48]. Increased mortality has been shown to positively correlate with the presence of the hyperinflammatory subphenotype in a series of clinical trials [45].

ARDS is primarily a clinical diagnosis and the potential outcome of a variety of disorders [46]. Clinical manifestations involve cyanosis, increased respiratory rate and work of breathing, tachycardia, and profound respiratory distress with decreased oxygen saturation in room air. In case of irreparable injury, patients develop respiratory failure, which may further progress to multiorgan failure and eventually death [49].

The majority of patients with ARDS present themselves with an underlying pulmonary or extrapulmonary infection, with primary bacterial or viral pneumonia being the most frequent causes [45, 47]. Influenza virus (IV) and respiratory syncytial virus (RSV) are considered major inducers of virus-induced ARDS [45]. The importance of viral pathogens as causative agents for severe lung injury has been recently highlighted by the SARS-CoV-2 pandemic, which has placed an enormous toll on public health over the last two years. Sepsis due to severe pneumonia or non-pulmonary infection is the second most common cause of ARDS, while other causes include aspiration of gastric or esophageal contents, post-traumatic hemorrhage and shock, as well as less common disorders, such as pancreatitis, transfusion-associated lung injury, smoke inhalation, near-drowning, and severe drug reactions [45-47].

Accumulation of edema fluid in the alveoli and disruption of the air-blood barrier leading to impaired gas exchange are the underlying mechanisms behind the development of ARDS (**Figure 3**) [47, 49]. Transepithelial ion transport is impaired during severe lung injury due to the decreased activity, expression, or mislocalization of the epithelial Na^+ or Cl^- channels or of the Na,K-ATPase , leading to reduced fluid clearance [50]. During the *acute* phase (days 1-6), inflammatory cells and erythrocytes infiltrate the inflamed alveoli due to the increased permeability of the endothelial

barrier [45, 47]. Although endothelial injury is a prerequisite for ARDS development, it is not sufficient to upset the gas exchange equilibrium, unless epithelial injury is also present [46]. Extensive inflammatory cell influx, though necessary for pathogen clearance, can eventually lead to the creation of paracellular gaps by destroying tight junctions [47]. Another important aspect of leukocyte influx is their role as sources of soluble, death-inducing ligands, such as tumor necrosis factor alpha (TNF- α) and TNF-related apoptosis-inducing ligand (TRAIL). Though these ligands will be addressed in more detail in a following chapter, we need to briefly address their contribution to epithelial injury in this part. In short, ligation to the respective receptors on the surface of epithelial cells triggers intracellular pathways which culminate in epithelial cell death and barrier damage [47]. Toxin release by specific pathogens such as *Staphylococcus aureus* [45] and release of cell-free hemoglobin from destroyed erythrocytes further contribute to the increased barrier permeability [45]. Gas exchange is additionally impaired by fibrin formation and formation of hyaline membranes above the denuded basal membrane [47].

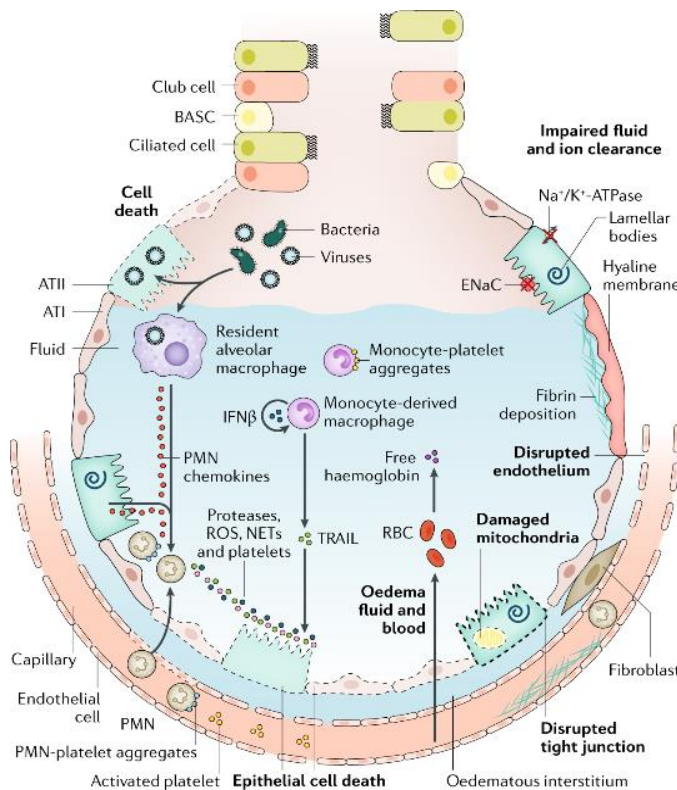


Figure 3. Different pathophysiological mechanisms contribute to ARDS pathology. ARDS can be the outcome of a multitude of insults. It is characterized by alveolar epithelial cell damage, influx of inflammatory cells, and extensive cytokine release. This leads to the disruption of the gas-blood barrier, impaired fluid clearance, and accumulation of intra-alveolar edema. Gas exchange is thus massively impaired. The resulting hypoxemia and hypercapnia clinically manifest as increased respiratory rate, dyspnea and, in case of severe ARDS, respiratory failure. Matthay et al, 2019, reproduced with permission of Springer Nature [45].

Resolution phase begins with the active transport of sodium and chloride through the apical and basolateral membrane of alveolar epithelial cells [47]. This transport creates a gradient for water reabsorption, leading to the clearance of intra-alveolar edema [47]. Cell debris and dead

inflammatory cells are cleared away through phagocytosis mechanisms, while resolution-driving lipid mediators, anti-inflammatory cytokines, and regulatory T lymphocytes mitigate tissue injury and restore homeostasis [47]. During the *subacute* phase (days 7-14), repair mechanisms involving proliferation of alveolar epithelial cells and infiltration of the alveoli by fibroblasts are intensified [47]. Complete resolution and return to homeostasis is achieved during the *chronic* phase (beyond day 14) [47]. In case of a persisting chronic phase, aberrant fibrosis formation and loss of functional lung tissue create a restrictive disorder pattern, which is translated into a diminished respiratory capacity [51]. This pattern can be often observed in severe coronavirus disease 2019 (COVID-19) cases, which, in their most extreme form, leave lung transplantation as the only therapeutic option [52, 53].

Despite decades of research, there is currently no targeted pharmacological treatment of ARDS [49]. Clinical trials applying a variety of potential treatment agents involving glucocorticoids, NO, antioxidants, or protease inhibitors, have failed to show an improvement in morbidity and mortality [47]. Current approaches to ARDS management involve the treatment of any underlying infections and mainly supportive treatment such as lung-protective ventilation, nutritional supplementation, and fluid-conservative therapy [45, 46]. Over the years, additional emphasis has been given to cell-based approaches, including mesenchymal stem cell administration, manipulation of host defense towards a less injurious phenotype, and restoration of the damaged epithelial barrier [45, 54].

Though ARDS-related studies have intensified in the backdrop of the COVID-19 pandemic, efficient therapeutic approaches are still lacking, and disease burden remains high [55]. Over the last 50 years, mortality has remained unchanged (ranging between 35% and 46%, depending on disease severity) [49], while patients present a higher need for discharge to rehabilitation and/or long-term care [56]. This signifies an unmet need to better understand the mechanisms driving this complex syndrome, of which IV infection is a prominent inducer.

Influenza A virus

Pneumonia caused by IV is the leading cause of infectious diseases-associated mortality in Europe, according to the European Center for Disease Control (ECDC) [57]. Even in the era of emerging viral pathogens such as SARS-CoV-2, IV remain one of the topmost causes of ARDS [45]. Historically, influenza has placed a significant burden on public health over time. The 1918 H1N1 pandemic (‘Spanish flu’) poses the best-known example, leading to the death of millions of people

during and at the aftermath of World War I [58, 59]. Over the course of the 20th century, smaller-scale pandemics, such as the H2N2 pandemic of 1957 (‘Asian flu’), the H3N2 pandemic of 1968 (‘Hong Kong flu’), the H1N1 pandemic of 1977 (‘Russian flu’) and, more recently, the H1N1 pandemic of 2009 (‘swine flu’, since then renamed ‘novel influenza A (H1N1) flu’) followed [58-60]. The toll of IV infection upon public health is, however, not limited to pandemics. Every year, up to 10% of the world’s adult and 20% of the children population is affected by influenza [58]. This reoccurrence highlights the continuous importance of IV as human pathogens even after decades of research.

Taxonomy and structure

IV belong to the family of *Orthomyxoviridae*, which are characterized by a multi-segmented, negative sense RNA genome. There are four genera of influenza viruses, influenza A, B, C, and D [58]. IV type A (IAV) are divided into subtypes (H_xN_x), according to their surface glycoprotein antigens, hemagglutinin (HA) and neuraminidase (NA) [61]. Until now 18 H antigens and 11 N antigens have been described, with subtypes H17N10 and H18N11 having so far only been found in Peruvian bats [62, 63]. Seasonal influenza waves are usually attributed to H1N1 and H3N2 IAV [58]. Although aquatic birds are the natural reservoir of IAV, these viruses can also infect domestic poultry and several members of the mammalian kingdom, including humans [61].

IAV genome consists of eight RNA segments of negative polarity which are numbered according to size (**Figure 4**) [64, 65]. They encode 11 different proteins: surface proteins HA and NA, matrix proteins 1 and 2 (M1, M2), polymerase proteins PB1, PB2 and PA, nucleocapsid protein (NP) and non-structural proteins 1 and 2 (NS-1, NS-2) [61, 65]. Alternative splicing or reading frames may result in slightly different products (e.g. NS-3, M4, PA-N155, PB1-F2) [66]. While some of these proteins have been well characterized, our knowledge of their potential functions remains rather limited for most [67]. Viral proteins are involved in different replication steps, from anchoring of the virus particle to the cell membrane and uncoating (HA, NA, M2), to genome transport into and out of the nucleus (NS-2), RNA replication (polymerases), and immune evasion (NS-1) [60, 68]. The viral genome and eight viral proteins comprise the ribonucleoprotein (RNP) core, which is surrounded by a lipid envelope. This envelope is derived from the cellular membrane of the host. Within its lipid bilayer, it contains the ion channel protein M2 as well as HA and NA, which serve as antigenic determinants of the virus [61].

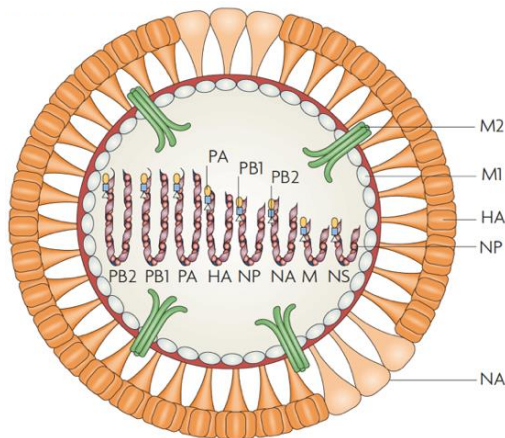


Figure 4. Influenza A virion structure. Depiction of a mature IAV particle containing eight negative-sense RNA segments, encoding for a total of eleven viral proteins. Eight viral proteins comprise the RNP core together with the RNA strands. A lipid, cell-membrane-derived envelope containing HA, NA, and the ion channel protein M2, surrounds the RNP core. Subbarao and Joseph, 2007, reproduced with permission of Springer Nature [61].

Antigen drift and antigen shift

Since viral polymerase lacks a proofreading function, punctual mutations arise in the HA and NA genes with every viral replication (*antigen drift*), creating new strains and making pre-existing immunity towards previous strains ineffective against any new ones. Due to this phenomenon, vaccination must be repeated anew with every influenza season [58, 60].

Another important aspect in the study of IAV infection is the genetic reassortment of different gene segments in cells simultaneously infected by two viral strains. This process leads to the creation of new viral strains, towards which there is no pre-existing immunity (*antigen shift*) [58]. This reassortment often takes place in the porcine host, which works as a vessel for porcine, avian, and human viruses, and can lead to pandemic outbreaks, as last observed during the novel influenza A (H1N1) flu pandemic of 2009 [58, 60]. This lack of pre-existing immunity may explain the higher virus transmissibility and disease severity which is observed in younger patients compared to older individuals during pandemics, as opposed to seasonal waves [60].

Transmission and viral replication

Similar to most respiratory pathogens, IV are transmitted through respiratory droplets of a medium size of 5 μ m which are created during coughing, sneezing, and occasionally even during normal speech in close contact with an infected person [58].

Once in the respiratory tract, IV target the epithelial cells of the upper airways. There, viral HA binds to sialic acid residues, which function as glycan receptors of the cell membrane [60]. In human viruses this interaction is performed via α -2,6-linkage, whereas avian viruses use an α -2,3-

linkage [58, 60, 61, 69]. This interaction leads to binding and fusion of the viral particle (virion) with the cell membrane. Viral entry is then performed via endocytosis or micropinocytosis, followed by transport to the lysosomes [58, 60]. The acidic environment there activates the viral M2 protein, leading to membrane fusion and release of the viral RNP core, followed by NP- and PB2- assisted transport to the cell nucleus [58, 60]. Once in the nucleus, the negative-oriented viral RNA is transcribed into messenger RNA with the help of viral polymerases. Translation into new viral proteins finally takes place in the ribosomes of the cell [58, 60].

Parallel to protein translation, positive RNA copies function as matrix for the synthesis of new negative-oriented RNA strands [58]. After leaving the nucleus, RNA strands and newly synthesized viral proteins form new RNP cores in the cytosol, which then assembly with HA, NA, and other viral proteins in lipid drafts of the plasma membrane. Budding of these regions is the last step in viral replication. HA-sialic acid residue bonds are cleaved by NA, leading to the release of viral progeny, which is now capable of infecting new cells (**Figure 5**) [58, 60]. In recent years, direct cell-to-cell transmission of viral particles via tunneling nanotubes has been described as an additional mechanism of viral spread [70]. The latter mechanism could provide a potential explanation for the successful viral propagation in the presence of hemagglutination-inhibiting antibodies, which can be observed during re-infection of influenza-immune individuals [70].

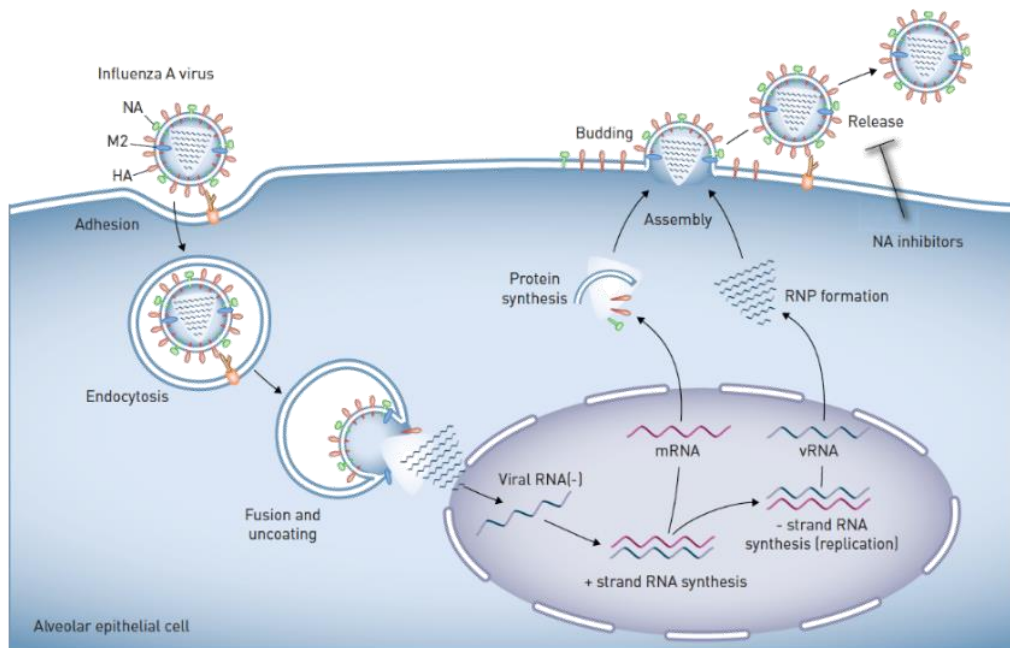


Figure 5. Replication cycle of influenza virus in the lung epithelium. Influenza viruses use the interaction between HA and sialic acid residues on the cell membrane as an anchoring mechanism, leading to endocytosis of the virion.

After being transferred to the lysosomes, activation of the viral M2 protein leads to uncoating of the viral RNP core and its transport to the nucleus. New RNP cores are synthesized and concentrated in lipid rafts of the cell membrane together with viral surface proteins. Newly synthesized virions are released with the help of NA, which cleaves the sialic acid residues, breaking their interaction with viral HA. Herold et al., 2015, reproduced with permission of the European Respiratory Society 2022 [60].

Initiation of intracellular anti-viral mechanisms

Viral presence in the cytoplasm initiates an immediate intracellular response, which mainly relies on three signaling pathways: Retinoic acid inducible gene I (RIG-I) proteins, Toll-like receptors (TLR), and the inflammasome [71]. More specifically, viral 5' triphosphorylated double-stranded RNA (5'-PPP dsRNA) leads to a conformational change of RIG-I, which enables its interaction with mitochondrial antiviral signaling proteins (MAVS) and the activation of NOD2 [7, 58-60, 72, 73]. This eventually leads to enhanced transcription of type I and type III interferons via activation of the interferon regulatory factor (IRF) as well as transcription of a variety of pro-inflammatory cytokines through the activation of nuclear factor kappa beta (NF- κ B) [58, 73]. TLR activation leads to the activation of IRF3 or IRF7, culminating in increased transcription of type I interferons (IFN- α/β). NF- κ B- induced transcription of pro-inflammatory cytokines can also be activated via this pathway [59, 60]. Finally, the presence of viral RNA leads to activation of the inflammasome and increased production of interleukins 1 β (IL-1 β) and 18 (IL-18) via cleavage and activation of cysteine-aspartic protease (caspase)-1 [58, 60, 71, 74, 75]. This intracellular antiviral response aims at limiting viral propagation, while at the same time initiating a systemic inflammatory host response to IV infection.

Inflammatory response to IV infection

TR-AM

The first line of innate immune defense against influenza virus is formed by TR-AM that phagocytose viral particles and apoptotic cells. Although TR-AM can get infected, they do not support viral replication in the same way alveolar epithelial cells do [76, 77]. Despite previous contradictory results, it is now considered that TR-AM infection with most IV strains remains abortive both in the commonly used mouse model and in humans, with the exception of highly pathogenic H5N1 and WSN H1N1 viruses [76-84]. TR-AM antiviral response heavily relies on type I IFN and IFN-stimulated genes. It involves upregulation of antiviral molecules and PAMP

receptors, alteration of endosome pH, as well as blocking of nuclear export [27, 69, 84-86]. Despite their inert anti-inflammatory phenotype [87], TR-AM can be major producers of pro-inflammatory cytokines and chemokines such as TNF- α , IL-6, monocyte chemoattractant protein-1 (MCP-1) and C-X-C motif chemokine ligand 10 (CXCL10) upon IV infection [76, 78, 88]. Additionally, TR-AM offer infection resistance to alveolar epithelial type I cells via regulation of the 5-lipoxygenase cysteinyl leukotriene pathway and suppression of leukotriene D4 production [89]. One of the hallmarks of IV-induced pneumonia is, therefore, the depletion of the TR-AM pool, which takes place early upon infection and has been linked to disease severity and increased mortality in various animal models [77, 89-94].

Immune cell recruitment

The abundant release of pro-inflammatory cytokines and chemokines leads to the recruitment of neutrophils [95], natural killer (NK) [59, 96], and natural killer T cells (NKT cells), [97] as well as BMDM, shortly after infection [59, 98]. The latter leave circulation mainly under the C-C motif chemokine ligand/receptor 2 (CCL2/CCR2) axis and enter the inflamed alveoli, where they adopt a pro-inflammatory phenotype. This phenotype is characterized by the abundant release of pro-inflammatory agents, such as TNF- α , IL-6 and NO derivatives, which contribute to viral clearance during the early infection phase [95, 98, 99]. Aberrant cytokine release, death-ligand-induced epithelial damage, and tissue flooding with matrix degrading proteases, however, may aggravate lung injury, rendering the antiviral response of BMDM into a double-edged sword [42, 58, 77, 80, 98, 100, 101].

Neutrophils utilize a variety of different functions, including phagocytosis, cytokine production, and release of granular contents such as defensins and cathelicidins in order to prevent viral dissemination [95]. They further serve as antigen-presenting cells guiding the recruitment and activation of CD8⁺ T lymphocytes in the lung [95]. Neutrophil influx, however, is often associated with excessive inflammation and increased disease mortality [101, 102]. Amplification of self-recruitment through the release of chemokines, vascular dysregulation, and extensive neutrophil extracellular trap (NET) formation, are considered as some of the main mechanisms through which neutrophils exert their controversial role upon IV infection [95, 103, 104].

Cytolysis by degranulation and release of granzyme and perforin are initiated upon binding of viral HA to cytotoxic receptors on the surface of NK cells [95]. Despite the fact that NK cells have been

associated with augmented pulmonary inflammation [105], they can mitigate IV-induced epithelial cytopathology through the production of IL-22, which supports epithelial integrity and return to homeostasis [95]. NKT cells are an intermediate between innate and adaptive immunity, as they share features of both NK cells and T lymphocytes [106]. Their antiviral capacity relies on cytokine release, upregulation of the pro-inflammatory receptor CD40, and activation of antigen-presenting dendritic cells [106].

Resident dendritic cells are additional important players in antiviral host response. Upon encountering viral particles, infected cells, or pro-inflammatory cytokines from epithelial and immune cells, they migrate to the draining lymph nodes [59, 95], where they employ their remarkable antigen-presenting capacity into activating naïve helper CD4⁺ and cytotoxic CD8⁺ T lymphocytes [58-60, 107-110].

As infection progresses, the adaptive immune response is initiated. T lymphocytes enter the alveoli as a response to antigen presentation by dendritic cells [60]. Following an initial expansion phase, activated T lymphocytes turn into master coordinators of the late-phase inflammatory process. Cytotoxic granules released by antigen specific CD8⁺ T lymphocytes cause lysis of infected cells, while helper CD4⁺ T lymphocytes maintain a central role in the establishment of infection memory [60]. Innate-like T lymphocytes expressing γ and δ chains as receptors ($\gamma\delta$ T lymphocytes) constitute another lymphocyte population which can traffic to the lung upon IV infection and contribute to the antiviral response by direct cytotoxicity or release of IFN- γ [95, 106]. Activation of all these leukocyte populations culminates into a well-orchestrated inflammatory response, which aims at the inhibition of viral replication within infected cells and at the prevention of further viral spread through targeted cell death, partially at the cost of tissue integrity (**Figure 6**). Return to homeostasis and disease outcome are therefore dictated by the thin balance between viral clearance and repair mechanisms within the inflamed lung.

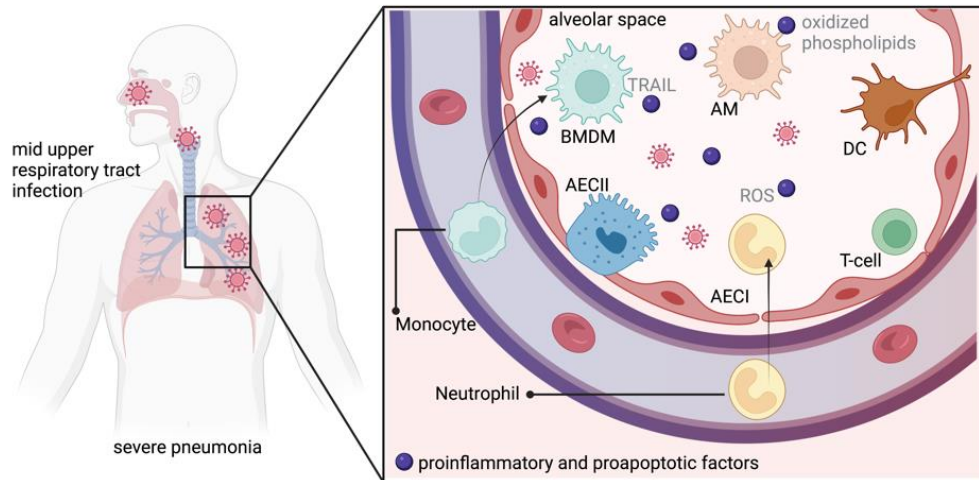


Figure 6. IV-induced pneumonia is characterized by a complex intra-alveolar inflammatory response. Viral presence within alveolar epithelial cells initiates a broad inflammatory process which involves TR-AM, neutrophils, inflammatory monocytes, and NK(T) cells. During the later stages of infection, T lymphocytes are recruited via their interaction with antigen-presenting dendritic cells, leading to the establishment of infection memory and inflammation resolution. Adapted from Peteranderl et al. 2016, created with BioRender.com [58].

Viral clearance and return to homeostasis

As viral clearance is achieved, acute inflammation subsides in favor of the re-establishment of homeostasis. T lymphocytes play a pivotal role in dampening the inflammatory response. Activated CD4⁺ and CD8⁺ T lymphocytes inhibit the expression of MARCO on TR-AM via IFN- γ , while CD8⁺ T lymphocytes additionally release the anti-inflammatory cytokine IL-10 and regulatory CD4⁺ T lymphocytes suppress neutrophil-associated cytokine production [60]. Parallel to that, pro-repair mechanisms are initiated, which aim at the restoration of the denuded airways. Type-2 innate lymphoid cells (ILC2s) are here of paramount importance, as they release the tissue-protective and pro-regenerative interleukins IL-22, IL-33, and amphiregulin [60, 95, 111, 112].

BMDM adopt a different polarization profile as a result of a complex crosstalk with the injured epithelium, helper T lymphocytes, and ILC2s [113, 114]. In contrast to pro-inflammatory macrophages, this phenotype is characterized by the release of immune-modulatory cytokines such as IL-10, CCL17, and CCL22, and pro-regenerative growth factors, including TGF- β , vascular endothelial growth factor (VEGF), platelet-derived growth factor (PDGF), and placenta expressed transcript 1 (PLET1) [60, 113]. Development of new blood vessels and enhanced cell proliferation support repair of the denuded epithelial layer and contribute to the restoration of the damaged

alveolar architecture [115]. These pro-regenerative macrophages eventually integrate themselves into the depleted TR-AM pool, following a series of transcriptional, functional, and phenotypical changes [116]. The new resident macrophage population which arises at the aftermath of infection is an amalgam of surviving TR-AM and recruited BMDM, thus preserving infection memory over time.

Humoral immunity is finally established through the expansion of certain B lymphocyte subpopulations and the production of antibodies against various viral proteins, in particular against the surface glycoproteins HA and NA, additionally contributing to the establishment of infection memory [59].

IV infection clinical course, treatment, and vaccination

IV can cause a variety of disease, ranging from mild upper airway infection to severe pneumonia eventually leading to ARDS and death due to respiratory failure [60]. Symptoms usually begin after 1-2 days of incubation and typically involve high fever and shivering. Dry cough, headache, sore throat, loss of appetite, myalgia, arthralgia, belong to the typical symptoms of influenza-like illness (ILI), which may persist for up to one week [58]. Dyspnea with low oxygen saturation and excessive fatigue indicate the transition to pneumonia, which may be aggravated by a secondary bacterial infection, the latter being the most common complication of IV infection [58]. Other, rarer complications, include meningitis or encephalitis, myositis, rhabdomyolysis, pericarditis, or myocarditis, and -in the case of intubated patients- invasive pulmonary aspergillosis. These complications are usually observed in patients belonging to high-risk groups, such as patients aged >65 or <2 years, immunocompromised, patients having undergone transplantation or with underlying cardiovascular, respiratory, hepatic or renal conditions, as well as pregnant women or nursing home residents [58, 59].

Mild influenza cases do not require any specific treatment but rather supportive measures. In more severe cases or in the case of high-risk or hospitalized patients, treatment should be initiated as early as possible, based on the clinical characteristics of the disease [58]. Currently, treatment of IV infection involves NA inhibitors, such as oseltamivir, zanamivir, and peramivir. Treatment with NA inhibitors should be initiated within 48h of symptom onset [58, 60]. The previously used M2 channel inhibitors (rimantadine, amantadine) are no longer recommended as antiviral drugs due to worldwide-spread resistance as well as lack of efficacy against IV type B. Polymerase A inhibitors

(baloxavir) have been recently approved for uncomplicated influenza cases in patients older than 12 years [57].

Vaccination remains the cornerstone of worldwide efforts in limiting IV disease burden. Influenza vaccines contain 4 (tetraivalent) antigens of 2 inactivated subtypes of IV A and (either one or both) IV B subtypes and can be applied intramuscularly [58]. Vaccines containing live, attenuated IV can be administered intranasally and are approved for children vaccination in Europe and in the USA [59]. The Center for Disease Control (CDC) recommends yearly vaccination of all persons older than 6 months, in particular high-risk individuals, pregnant women, residents of nursing homes, and healthcare professionals [57]. The establishment of herd immunity is paramount in order to minimize the number of severe cases, the need for hospitalization, and overall morbidity and mortality, which can be attributed both to the infection itself and its complications.

Post-influenza bacterial infection

Bacterial pneumonia following primary infection is one of the most common complications of influenza and can have a significant impact on disease outcome [8, 117, 118]. The presence of a bacterial superinfection, most commonly with *Streptococcus pneumoniae*, could be demonstrated in the vast majority of all severe cases and deaths during the 1918, 1957, and 1968 influenza pandemics [118-120]. In recent years, *Staphylococcus aureus* has additionally gained significance as a bacterial pathogen leading to secondary pneumonia, as shown in various studies in the aftermath of the 2009 H1N1 pandemic [119]. Other, less frequent, bacterial pathogens causing post-influenza pneumonia involve *Haemophilus influenzae*, *Moraxella catarrhalis*, and occasionally atypical bacteria such as *Mycoplasma pneumoniae* [8, 121].

Virulence factors associated with the virus as well as host immune mechanisms are interlinked and establish susceptibility to secondary bacterial pneumonia [118, 122]. IV-induced epithelial cell death disrupts the first line of defense against invading pathogens, while excessive cytokine release and uncontrolled influx of inflammatory cells may impair host defense mechanisms [8]. At the same time, exploitation of host glycoconjugates provides a rich nutrient source for bacteria [119, 123]. Fibrin deposition leads to obstruction of small airways and impaired gas exchange, creating an environment which supports bacterial growth. Mechanical clearance is further impaired due to a decrease in ciliary beat frequency [119, 124]. Virulence factors such as the expression of the accessory protein PB1-F2 and manipulation of the host immune response towards the establishment

of an anti-inflammatory state further facilitate secondary bacterial pneumonia [119, 121, 122, 125, 126]. Recently, new data has come to light regarding the role of the gut microbiome as a determinant of disease progress. IV infection has been shown to actively alter the metabolism of fatty acids in the gut [118]. These changes can, in turn, shape immune responses against invading pathogens in the lung, including interferon response, growth factor production, macrophage phagocytosis capacity, dendritic cell migration, and antibody response [118].

Virus-induced depletion of the TR-AM pool needs to be highlighted as an important determinant of susceptibility towards secondary bacterial infection [119, 127]. Animal and mathematical experimental models have demonstrated that the period of maximum susceptibility coincides with the depletion phase of TR-AM [127, 128]. Defective phagocytosis capacity has been shown in a series of different studies to further aggravate the effect of TR-AM loss [129]. IFN- γ , which is abundantly released in the alveoli as part of the antiviral response, heavily impairs the phagocytic functions of alveolar macrophages, partially through downregulation of key scavenger receptor MARCO [122, 130, 131].

All these mechanisms lead to enhanced permissiveness for the expansion of bacterial populations which colonize the upper airways [8, 132]. In fact, pneumococcal density in the upper airways has been revealed to be an important parameter in the pathophysiology of post-influenza pneumonia [8]. Alternatively, bacterial pulmonary infection can be the aftermath of inhalation and short-term colonization by a new, more invasive bacterial strain (**Figure 7**) [119, 133]. In either case, bacterial dissemination is rendered possible through the deleterious effect of IV infection on alveolar barrier integrity, which can be heavily attributed to extensive and, in case of severe disease, uncontrolled cell death.

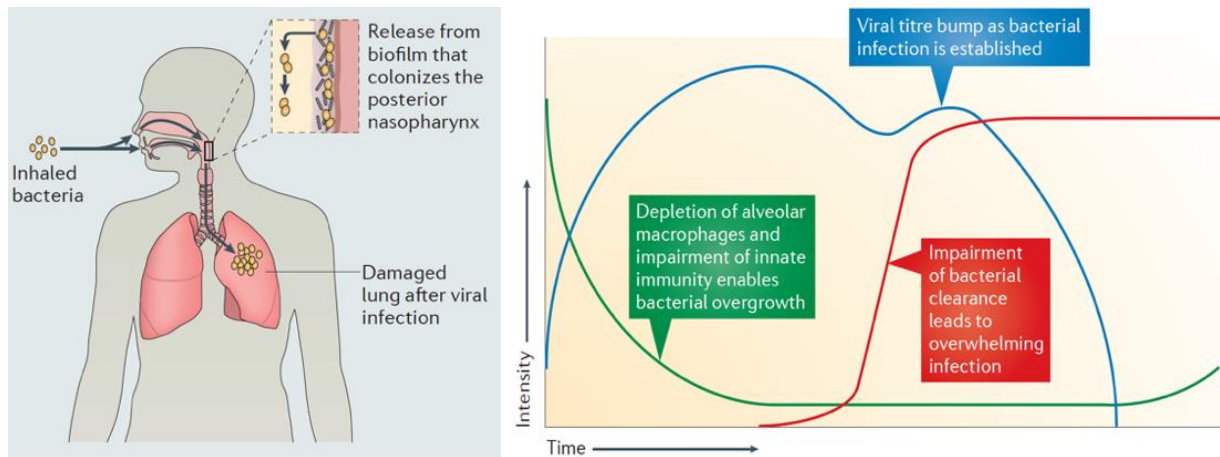


Figure 7. Post-influenza TR-AM depletion enables the establishment of secondary bacterial pneumonia. Left panel: Exploiting the locally compromised immune defense following viral infection, bacteria disseminate within the distal lung either as expansion of local biofilm colonizing the upper airways or per direct inhalation of a new, more invasive bacterial strain [119]. Right panel: Viral titers increase rapidly during the acute phase of infection leading to depletion of the alveolar macrophage pool. As time progresses, virus titers start declining, however, with the first line of defense heavily now impaired, uncontrolled bacterial growth is established. McCullers JA, 2014, reproduced with permission of Springer Nature [119].

Cell death and death-inducing ligands

Initiation of cell death pathways is one of the best conserved mechanisms observed in different development, carcinogenesis, infection, and repair-after-injury processes [65]. In case of infection, epithelial cells and leukocytes regulate cell death programs in a tight manner, in order to restrict infection spread, while preserving the functions of healthy cells. At the same time, pathogens try to manipulate cell death mechanisms of the host in favor of further dissemination [134].

Apoptosis has been traditionally associated with programmed cell death and therefore plays an important role in maintaining tissue homeostasis, though it can also be involved in inflammatory processes [135]. Main apoptosis pathways involve the intrinsic, extrinsic, and granzyme-mediated pathway. The intrinsic apoptosis pathway is initiated by intracellular stimuli culminating in the activation of the B cell lymphoma (BCL-2) protein family and transport of the pro-apoptotic BH3-interacting domain death agonist (BID) into the mitochondria, where it increases permeability of the outer mitochondrial membrane [73, 136]. This series of events enables the release of cytochrome c and second mitochondria-derived activator of caspases (SMAC) -alternatively named 'direct IAP binding protein with low pI (DIABLO)'- into the cytoplasm [135, 137].

Cytochrome c release contributes to the activation of the apoptosome and thus directly initiates cell death, whereas SMAC binds to the anti-apoptotic X-linked inhibitor of apoptosis protein (XIAP), therefore allowing the recruitment and activation of effector caspases [135, 136]. Recent findings have challenged the traditional association of the intrinsic pathway exclusively with intracellular stimuli, proving that it may also be activated upon crosslinking of death-inducing ligands to their respective death receptors [136, 137].

The extrinsic apoptosis pathway is the pathway traditionally associated with members of the TNF superfamily (TNFSF). This family involves a variety of structurally homologous ligands which, upon interaction with their respective receptors, orchestrate a complex intra- and intercellular communication network. The initial ligation step may lead to different outcomes regarding cell fate, depending on cell identity and the specific (patho)physiological circumstances (**Figure 8**) [138].

TNFSF receptors are characterized by a cysteine-rich ectodomain and are subdivided according to their cytosolic signaling into those which utilize a death domain, those which exert their signaling potential through the TNF receptor-associated factors (TRAF) family of ubiquitin E3 ligases, and, finally, those which act as decoy receptors by lacking any cytosolic domain [138, 139]. Cross-linking of a ligand to a cell membrane-expressed death receptor leads to the assembly of death-inducing signaling complex (DISC) through the recruitment of Fas-7-associated surface antigen (Fas)-associated protein with death domain (FADD) and caspase-8. DISC formation leads to the activation of caspase-8 through proteolytic cleavage, which in turn activates effector caspases such as caspase-3 and -7 [135-137, 140]. Granzyme-mediated apoptosis is a specific form of apoptosis employed by cytotoxic NK cells and T lymphocytes, which involves BID activation by endocytosed granzyme B within the cytosol of target cells, leading to their apoptotic death [135]. Necroptosis emerges as an alternative pathway to apoptosis upon lack of sufficient amounts of FADD or pro-caspase-8. Receptor-interacting serine/threonine-protein kinase 1 (RIP-1) is then recruited to DISC, where it further recruits and activates the RIP-3 kinase [135]. In this case, cell death is initiated through activation of mixed lineage kinase domain-like (MLKL) and/or poly-ADP-ribose (PAR) polymerase 1 (PARP-1) [136]. Anti-apoptotic proteins such as BCL-2 and CASP8 and FADD-like apoptosis regulator (CFLAR) are upregulated parallel to their pro-apoptotic counterparts upon ligand crosslinking [73]. In the setting of acute infection, these anti-

apoptotic proteins serve as balance regulators and protect the cells from pathological, untimely activation of cell death due to the pathogen itself or circulating death-inducing ligands [141].

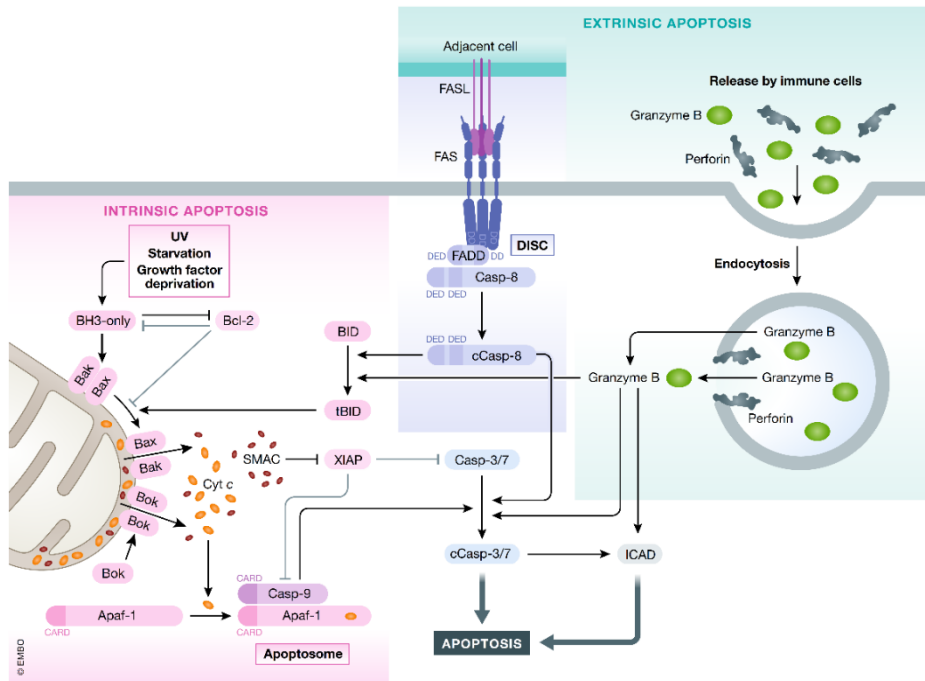


Figure 8. Apoptosis can be the endpoint of the intrinsic, extrinsic, or granzyme-associated programmed cell death pathway. Direct activation of caspase-3 or -7 by caspase-8 following ligation of a death-inducing ligand (here depicted is Fas ligand as a typical example) to its receptor characterizes the extrinsic apoptotic pathway. Caspase-8-orchestrated translocation of the pro-apoptotic factor Bid into the mitochondria as a result of starvation or growth factor deprivation culminates in the activation of the apoptosome and/or activation of caspase-3 and characterizes the intrinsic apoptotic pathway. Endocytosis of cytotoxic cell-released granzyme B can also lead to BID activation and result in apoptotic death. If cell death is induced by ligand crosslinking but apoptosis cannot be executed due to lack of procaspases, the necroptotic pathway is initiated, involving kinases RIP-1 and RIP-3 (not depicted). Kist M and Vucic D, 2021, reproduced with permission of John Wiley and Sons [135, 137].

Pyroptosis emerges as an important type of cell death in the context of infection/inflammation. As previously mentioned, PAMP recognition by TLRs leads to inflammasome formation, caspase-1 activation, and release of IL-1 β and IL-18 [58, 135]. Parallel to that, caspase-1 cleaves gasdermin-D, separating the auto-inhibitory C-domain from the lytic N-domain [135, 139]. This enables the latter to translocate to the cell membrane, where it initiates cell lysis [135, 142].

Autophagy processes are initiated upon cell stress and involve lysosome-driven organelle degradation. The resulting components can then be used to form new subcellular structures or as a source of energy [139]. In case of excessive degradation, however, autophagy results in cell destruction, as often observed during elimination of aged cells or within neoplastic lesions [139]. In recent years, other forms of programmed cell death have been described, including oxidative-stress or Ca^{2+} accumulation-mediated mitochondrial permeability transition pore (MPTP) necrosis, DNA damage-induced parthanatos, and reactive oxygen species (ROS)-related ferroptosis [135, 139, 143].

Though previously believed to function without any significant overlap, cell death pathways are now considered to be tightly linked and capable of cross-regulation [142]. This sets TNFSF ligands with their ability to initiate different death pathways in the epicenter of cell death studies, in particular in the context of infection, which involves a plethora of cell populations, pathogens of varying virulence, and a complex network of host defense mechanisms.

TNFSF and IV infection

Death-inducing ligands in IV infection have been a continuous research object over the years, emphasizing the complicated role of this family in this context [144-146]. TNF- α (TNFSF1) release by the injured epithelium and by immune cells in particular contributes to viral clearance but may also aggravate disease outcome in terms of an exuberant inflammatory response [95, 98]. TRAIL (or TNFSF10), one of the most extensively studied members of the TNFSF, is released by directly infected cells [147, 148] or by primed innate and adaptive immune cells [98, 109, 110], and has been associated with alveolar fluid clearance impairment, increased morbidity, and enhanced susceptibility to secondary pneumococcal infection in mice [99, 146] as well as higher morbidity in patients with IV-induced ARDS [144]. Ligation of Fas ligand (FasL, TNFSF6) to the Fas receptor leads to the apoptotic death of recruited macrophages upon IV infection and further affects disease severity in a type-I-interferon-dependent manner [145, 149]. These examples demonstrate but by no means exhaust the various functions of TNFSF members and highlight the need to further understand their controversial functions during IV infection.

TNFSF14/LIGHT

LIGHT (homologous to Lymphotoxin, exhibits inducible expression and competes with Herpes Simplex Virus glycoprotein D for HVEM, a receptor expressed by T lymphocytes), also known as CD258 or TNFSF14, is a relatively understudied member of the TNFSF, compared to the better-known TRAIL or FasL. Typically found as a transmembrane type II protein of 29kDa in a homotrimer form with an internal N-terminus, TNFSF14/LIGHT may also exist in a soluble form, which retains its receptor-binding and signal-inducing capacity upon proteolytic cleavage [150-152]. An alternatively spliced form deletes the transmembrane domain, thus ending up in the cytoplasm, where its function remains unknown [151]. TNFSF14/LIGHT binds to three different receptors: type I transmembrane lymphotoxin beta receptor (LT β R), herpesvirus entry mediator (HVEM, also known as TNF receptor superfamily 14, TNFRSF14), and soluble inhibitory decoy receptor 3 (DcR3), which is found in most animals of the Chordata phylum, but not in mice and rats (**Figure 9**) [138, 150, 153-155].

TNFRSF14/HVEM (CD270) is a common receptor for TNFSF14/LIGHT, lymphotoxin α (LT α), the two members of the immunoglobulin family B and T lymphocyte attenuator (BTLA) and CD160, as well as the virion glycoprotein D of herpes simplex virus [138, 154]. It is constitutively found on the surface of all hematopoietic lineages but can also be expressed by non-hematopoietic cell populations, such as the mucosal epithelium [156]. The main functional activity of TNFSF14/LIGHT- TNFRSF14/HVEM crosslinking is considered to be a co-signaling pathway in T lymphocytes [154]. TNFRSF14/HVEM expression is, therefore, observed in a variety of tissues, including spleen, thymus, bone marrow, but also lung and intestines [154, 157]. When acting as a canonical TNF receptor, receptor-ligand crosslinking leads to the activation of NF- κ B through the involvement of the TRAF2/3 pathway, thus promoting cell survival and differentiation [138, 157]. Interestingly, BTLA crosslinking may restrict B and T lymphocyte proliferation and it can be assisted or inhibited by TNFSF14/LIGHT in this function [138]. While binding of the transmembrane form of TNFSF14/LIGHT to TNFRSF14/HVEM serves as a counter-regulator to BTLA, interaction of the receptor with soluble TNFSF14/LIGHT enhances the inhibitory role of the BTLA checkpoint [138]. The variety of potential ligands and interaction outcomes proves that TNFRSF14/HVEM can promote both pro- and anti-inflammatory pathways, depending on the interaction in question.

Unlike TNFRSF14/HVEM, LT β R is absent from T and B lymphocytes, but it is widely distributed on stromal and parenchymal cells, dendritic cells, and macrophages of most organs [150, 154]. LT β R serves as a receptor for two potential ligands, TNFSF14/LIGHT and the LT $\alpha_1\beta_2$ heterotrimer. The LT $\alpha\beta$ -LT β R interaction is required for the formation of secondary lymphoid tissue, including lymph nodes, Peyer's patches, and germinal centers in the spleen, but also for the development of NK cells and the afferent lymphatic migration of T lymphocytes [150, 158, 159]. Recently, LT β R-TNFSF14/LIGHT ligation has been linked to increased survival and proliferation of human bone marrow mesenchymal stem cells *in vitro*, making this interaction an interesting research topic for stem-cell based therapies [160]. Ligand binding to LT β R initiates canonical and non-canonical NF- κ B pathways [159] and, in contrast to HVEM, which lacks a death domain, may additionally lead to cell death via apoptosis [158, 161].

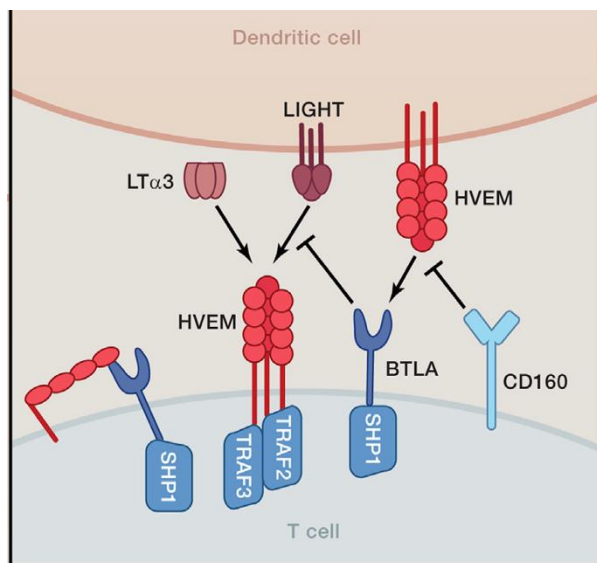


Figure 9. Depiction of TNFSF14/LIGHT and TNFSF14/LIGHT receptor signaling in lymphoid cells. TNFSF14/LIGHT is a homotrimer type II transmembrane protein with three potential receptors; TNFRSF14/HVEM, which is found on all hematopoietic and various non-hematopoietic cells; LT β R, which is absent from lymphocytes but is expressed on most members of the myeloid compartment; and DcR3, which serves as an antagonist for the other two receptors. Ward-Kavanagh et al., 2016, reproduced with permission of Elsevier [138].

TNFSF14/LIGHT expression is observed in a variety of tissues, where it emerges as an inflammation and homeostasis mediator [154]. It is widely expressed on cells of the hematopoietic compartment, including T and B lymphocytes, dendritic cells, NK cells, and platelets [152, 162, 163]. TNFSF14/LIGHT plays a significant role in T lymphocyte co-stimulation, activation, and proliferation [154]. Blockade of its signaling pathway therefore impairs allogeneic T lymphocyte responses, highlighting a role in graft-versus-host-disease [151, 154, 164]. Furthermore, TNFSF14/LIGHT has been linked to several autoimmune inflammatory diseases, including, but not limited to, inflammatory bowel disease [151, 165], atherosclerosis and coronary heart disease

[166, 167], diabetes mellitus type 2 [168], nonalcoholic fatty liver disease [169], systemic sclerosis [170], atopic dermatitis [171], hepatitis [172], preeclampsia [173] and rheumatoid arthritis [174, 175]. The role of TNFSF14/LIGHT-initiated inflammatory responses has been additionally studied in the context of viral [176, 177], bacterial [153, 178] and parasitic [154, 179] infection. Depending on the pathogen and cell population of interest, TNFSF14/LIGHT has been shown to exert different functions regarding T lymphocyte activation, adaptive immune response, and establishment of infection memory. Studies addressing the role of the ligand upon early infection and any potential impact on innate immunity are, however, still lacking.

In the lung, TNFSF14/LIGHT has been associated with the promotion of airway remodeling and hyperresponsiveness in asthma models [176, 180] as well as enhanced fibrosis formation and smooth muscle hyperplasia through increased production of TGF- β , IL-1 β , and IL-13 by structural and immune cells in idiopathic pulmonary fibrosis, dermatomyositis, and systemic sclerosis [176, 181-183]. High TNFSF14/LIGHT serum levels have been further linked to the development of interstitial pneumonia in patients with dermatomyositis, presumably as a result of TNFSF14/LIGHT-activated CD8⁺ T lymphocyte infiltration of the lung and elevated Th1 cytokine production [184]. Recently, TNFSF14/LIGHT has been attributed a potential role in COVID-19, with high plasma levels [185, 186] and increased expression of TNFSF14/LIGHT in peripheral blood mononuclear cells (PBMCs) having been described in patients with severe COVID-19 [185].

2. Aims of this work

Influenza A virus (IAV)-induced pneumonia remains a significant threat in the era of emerging viral infections. One of the immunological hallmarks of the disease is the depletion of the tissue-resident alveolar macrophage (TR-AM) pool. This compromises host defense, thereby enabling the establishment of secondary bacterial pneumonia, which is one of the most common and severe complications of IAV infection. Despite years of research, the pathophysiological mechanisms driving TR-AM depletion remain largely unknown.

The primary aim of the presented work was to investigate the underlying mechanisms leading to TR-AM loss during IAV infection and to therapeutically address the aforementioned mechanisms. The next aim of this work was to address the clinical outcome of post-influenza pneumococcal pneumonia following successful prevention of TR-AM death through direct targeting of any involved pathways.

Together, the ultimate aim of this study was to better understand host defense, design novel therapeutics, and improve disease outcome in the light not only of primary viral but, more importantly, viral and secondary bacterial infection.

3. Methods

Mouse strains

Wild-type C57BL/6 mice were purchased from Charles River Laboratories. *Tnfrsf14*^{-/-} [187], *tnfrsf14*^{-/-} [188], and *ltbr*^{-/-} [189] mice were provided as a gift by the group of Prof. Klaus Pfeffer from the University Clinic of Düsseldorf. Mice were bred under specific pathogen-free conditions (SPF), used between 10 and 12 weeks of age, and transferred to IVC conditions upon treatment. Monitoring was performed daily depending on experimental severity. A scoring system was developed based on weight reduction, general physical appearance, spontaneous behavior, as well as specific experiment-relevant criteria (tachypnea, dyspnea, visible breathing with reduced breath frequency, apathy, immobility, severe exsiccosis, cyanotic mucosae, and gasping). Depending on the scoring, specific measures were undertaken in line with local animal welfare laws (**Table 1**):

Table 1. Experimental scoring for *in vivo* experiments.

0	Scoring once daily, no measures undertaken.
5-9	Scoring twice daily, 5% glucose added to the drinking water, softened food pellets placed within the cage, reduced handling.
10-19	Scoring three times a day, 5% glucose added to the drinking water, softened food pellets placed within the cage, reduced handling, and consultation with a veterinarian.
20 or higher, based on 2-3 different parameters	Scoring every 4-6 hours, 5% glucose added to the drinking water, high-calory wet food (e.g. Clear H ₂ O boost or liquid altromin), reduced handling, and consultation with the animal welfare officer.
20 or higher, based on one parameter, or several parameters persisting over 24h	Euthanasia and notification of the project leader.

Animals were euthanized when a scoring of 20 (single parameter or several parameters persisting over 24h) was achieved, when a control animal had to be sacrificed due to high scoring and an analysis was possible at the given time point, or when an animal received an unchanged scoring of 10-15 for over 5 days. Animal experiments were performed at the Biomedical Research Center Seltersberg (Biomedizinisches Forschungszentrum Seltersberg) and the Central Animal Laboratory (Zentrales Tierlabor, Room 108) of the Justus Liebig University of Giessen as well as the Max Planck Heart and Lung Laboratory of the Institute of Biomedicine Investigation of Buenos

Aires (Instituto de Investigación en Biomedicina de Buenos Aires, IBioBA-CONICET-Partner Institute of the Max Planck Society).

Cell culture

Cell lines

Madin-Darby canine kidney (MDCK) II cells were cultured in cell culture flasks in full medium (DMEM, 10% FCS, 1% penicillin/streptomycin, 1% L- glutamine, 2.5% HEPES) at 37°C and 5% CO₂. Cells were detached and singularized with trypsin-EDTA after washing with PBS^{+/+} for passaging. For experimental purposes, cells were passaged on 6-, 12-, or 96-well plates 24h prior to further treatment. DMEM was purchased from Gibco/Life Technologies, Carlsbad (USA).

Primary alveolar macrophages

Primary tissue-resident alveolar macrophages (TR-AM) were isolated from the bronchoalveolar lavage fluid (BALF) of non-infected mice. Mice were sacrificed by cervical dislocation. After exposure of the trachea, a small incision was performed and a shortened 21-gauge cannula was inserted for BALF acquisition. Mice were lavaged in ten instillation steps with 0.5ml PBS^{-/-}/2mM EDTA. BALF samples were stored on ice until further process. Samples were centrifuged at 1600rpm for 8min at 4°C, after which pellets were resuspended in TR-AM medium (RPMI, 2% FCS, 2.5% HEPES, 1% penicillin/streptomycin, 1% L-glutamine). TR-AM were seeded at a density of 100,000-125,000 cells/cm² and left to adhere for 2h before further treatment.

Influenza A virus propagation and titration

Influenza virus A/Puerto Rico/8/34 (H1N1) (IAV PR8) was propagated on canine epithelial MDCK II cells. Seasonal wild-type mouse-adapted influenza A virus was propagated in the lab of Stephan Pleschka, Virology, Giessen (Germany). A recombinant strain of the seasonal mouse-adapted virus was propagated in the lab of Thorsten Wolff, Robert Koch Institute, Berlin (Germany). Cells were passaged in a T75-cell culture flask at a ratio of 1:3 one day prior to infection up to 85-90% confluence at the time point of infection. Cells were washed with PBS^{+/+} and infected at a 0.001 multiplicity of infection (MOI). The virus dilution was prepared in MDCK II infection medium (MDCK medium as described above but supplemented with 0.2% BSA instead of FCS). Cells were inoculated with 5ml virus dilution for 1h at 37°C and 5% CO₂. After that, they were washed and

further incubated with 10ml infection medium containing trypsin-TPCK in a 1:1000 dilution. Cell culture supernatants containing virus particles released from the infected cells were harvested after 36-48h when a cytopathic effect of approximately 70% had been achieved and centrifuged at 1600rpm at 4°C for 30min. Supernatants were aliquoted and stored at -80°C.

To determine the amount of virus particles capable of multicycle replication (foci forming units, ffu), MDCK II cells were seeded in T-shaped 96-well plates one day prior to infection. Cells were washed with PBS and infected with 0.05ml of serial 1:10 dilutions of the virus stock in PBS^{+/+}/0.2%BSA/1% penicillin/streptomycin/1% L-glutamine, covering a range of dilutions from 1:10¹ to 1:10⁸. Virus dilutions were inoculated at 37°C, 5% CO₂ for 45-60min, cells were then covered with 100µl Avicel medium (10% 10x MEM/30% dH₂O/0.3% BSA/1% DEAE dextran/0.3% NaHCO₃/1% penicillin/streptomycin/1.25% Avicel) containing 1µg/ml trypsin-TPCK. Due to its high viscosity, Avicel prevents viral spread through the cell culture by diffusion of viral particles in the surrounding medium and only allows virus spread from cell to cell.

Cells were incubated for further 24-36h at 37°C, 5% CO₂, to allow formation of foci caused by local virus propagation. After this incubation step, PBS^{+/+} was added to the cells for 10-15min at RT, in order to reduce Avicel viscosity. Following 3 washing steps with PBS^{+/+}, cells were fixed and permeabilized through the addition of fixing solution containing Triton X-100 (PBS^{+/+}/3.7% PFA/1% Triton X-100) for 30min at RT. After that, fixing solution was discarded, cells were washed three times with PBS^{+/+}/0.05% Tween 20 (‘washing solution’), and plates were left to dry. Plaques were visualized by immunohistochemical staining. Incubation with a primary anti-influenza nucleoprotein (NP) antibody diluted 1:100 in PBS/3% BSA for 1h at RT was followed by incubation with a secondary, horse raddish peroxidase (HRP)-marked, anti-mouse antibody, diluted 1:1000 in PBS/3% BSA for 1h at RT. Addition of TrueBlue -an HRP substrate yielding a blue color after enzymatic progressing- allowed counting of the number of foci per well.

The titer of the virus stock was calculated according to the following equation:

Number of foci per well*20 (infection is done in 50µl, 1:20 of 1ml) *10^{dilution} where single foci could be counted = ffu/ml.

***In vivo* experiments and preparation of animal-derived samples**

Influenza A virus and secondary Streptococcus pneumoniae infection

For *in vivo* IAV infection, mice were premedicated with atropin (application 0.05mg/kg; 0.5mg/ml initial concentration diluted in 0.9% sterile NaCl to 0.05mg/ml and applied subcutaneously at 0.2ml per 20g body weight) and anesthetized by isoflurane inhalation. More specifically, oxygen containing 4% isoflurane was supplied under constant flow into the induction chamber of an anesthesia device [TEM SEGA, (FR)]. The induction chamber was automatically heated up to maintain body temperature upon device ignition. Once gas flow had been stabilized, mice were placed in the induction chamber until loss of their righting reflex, upon which they were transferred from the induction chamber to the intubation station (60° plane). Mice were then fixed by their incisors and hindlegs in a supine position, while 2.5% isoflurane was applied at a flow rate of 0,3L/min through a nose mask. An endotracheal tube was then inserted orally, passing between the vocal cords into the trachea. Using a 27G syringe, mice were inoculated with 500ffu of IAV diluted in 0.07ml sterile PBS^{-/-}. Control groups were inoculated with 0.07ml of sterile PBS^{-/-} without additives. Mice were then returned to their cage and monitored until complete recovery from anesthesia could be observed. Treated mice were monitored 1-3 times per day, depending on disease severity, as described above.

For co-infection experiments, mice initially infected with 250ffu IAV were additionally infected with *Streptococcus pneumoniae* serotype 3 on day 7 post-IAV infection (pi), bacterial strain kindly provided by the research group of Martin Wizenrath, Charité, Berlin (Germany). Pneumococci were streaked on 4-5 sheep blood agar plates (Oxoid, GER) and left to grow at 37°C for 8-10h on the day prior to infection (day 6 pi). Pneumococci were then harvested using an inoculation loop and left to grow in liquid medium (THY medium; 30g Todd-Hewitt broth powder/5g yeast extract/1L distilled water) containing 10% heat-inactivated FCS at 37°C until the desired optical density was reached. The latter was measured with an Ultrospec 10 cell density meter (Amersham Biosciences, UK) using a 1,5ml semi-micro PMMA disposable cuvette (BRAND® UV, Merck, GER) containing 1ml of bacteria in liquid medium. A blank cuvette containing 1ml of liquid medium was used as baseline control. Once the optimal density of 0.03-0.04 had been established, liquid culture was stored within a tightly sealed canister in ice overnight. On the day of infection, the liquid bacterial culture was removed from ice and allowed to grow at 37°C for 3h until reaching an OD of 0.3-0.4 (equals 3-4 x10⁸ cfu/ml), upon which it was centrifuged at 3100IU/min, 10min,

10°C, at a deceleration rate of 1. Bacteria were then resuspended in the appropriate volume of sterile PBS^{-/-} in order to achieve a concentration of 1x10⁹/ml and were further diluted up to a final concentration of 20-50cfu/0.05ml PBS^{-/-}, which was used as the infection dose. Bacterial inoculation was then performed intranasally in lightly anesthetized mice (isoflurane-induced anesthesia in an induction chamber, as described above). Mice were returned to their cage and monitored until ambulatory conditions had been established. Treated mice were monitored 1-3 times per day, depending on experimental severity. Infection dose was confirmed by overnight culture of 0.05ml of final bacterial concentration diluted in 0.2ml PBS^{-/-} on a sheep blood agar plate and quantification of the number of colony-forming units (cfu) 16h later.

Orotracheal administration of recombinant tnfsf14/light

For treatment with recombinant tnfsf14/light (rTnfsf14/Light), mice were infected with 500ffu IAV diluted in 0.05ml PBS^{-/-} as described above. On days 1 and 2 pi, mice were anesthetized and received 10µg rTnfsf14/Light (R&D Systems, GER) diluted in 0.03ml PBS^{-/-}. Control groups received 0.03ml PBS^{-/-} per time point. Following infection and treatment, mice were returned to their cages and monitored daily through clinical scoring. Organ harvesting and experimental analysis were performed on day 3 pi.

Adoptive transfer of TR-AM and co-infection experiments

For adoptive transfer experiments, C57Bl/6 wild-type mice were infected with 250ffu IAV, infection procedure as described above. Three days later, BALF was obtained from non-infected wild-type, *tnfrsf14*^{-/-}, or *ltβr*^{-/-} mice, and centrifuged at 1600rpm for 8min at 4°C. Pelleted cells were resuspended in 1ml MACS buffer (PBS, 7.4% EDTA, 0.5% FCS pH 7.2). After determination of the total cell count, cells were centrifuged once again at 1600rpm, 4°C, for 8min, and resuspended in the appropriate sterile PBS^{-/-} volume, so that 300,000-500,000 cells per 0.05ml PBS could be oro-tracheally transferred to the animals. Adoptive transfer was performed in isoflurane-anesthetized mice using a Hamilton® 1725 RN 0.25ml (Hamilton Company, USA) syringe. Following transfer, mice were returned to their cage and monitored until ambulatory conditions had been established. Treated mice were monitored 1-3 times per day, depending on experimental severity. Secondary pneumococcal infection was performed four days later (day 7 pi), as described

above. Clinical scoring was performed daily until experimental ending, according to the previously mentioned criteria.

Caspase inhibitor and neutralizing antibody treatment

The *in vivo* effect of apoptosis inhibition was addressed through the use of specific caspase inhibitors in IAV-infected mice. More specifically, mice were infected with 500 (for day 7 experiments) or 1000ffu IAV (for day 3 experiments) as described above and treated with a specific caspase-3 or caspase-8 inhibitor, or a DMSO control. Lyophilized caspase-3 and caspase-8 inhibitors were diluted in 0.075ml or 0.0765ml DMSO, respectively, for a concentration of 20mM. Further dilution was then performed in sterile PBS^{-/-} for a final concentration of 10mg/kg (0.015ml of the 20mM stock diluted in 0.045ml PBS^{-/-}). Diluted inhibitors and their DMSO controls were then applied subcutaneously on day 2 pi when analysis was performed on day 3 pi, or daily on days 2-6 pi for analysis on day 7 pi.

For neutrophil depletion, 200µg of an anti-Ly6G antibody (InVivoMAb anti-mouse Ly6G antibody, clone 1A8, 9,8mg/ml, BioXCell, USA) or an isotype control (InVivoMAb rat IgG2a isotype control, anti-trinitrophenol, clone 2A3, 9,7mg/ml, BioXCell, USA) diluted in 0.1ml sterile PBS^{-/-} were injected intraperitoneally (i.p.) in IAV-infected mice (500ffu) on days -1, 1, 3, and 5 pi.

For tnfsf14/light neutralization, a mouse specific blocking antibody was kindly provided by the research group of Professor José Ignacio Rodríguez Barbosa, University of León, León (ES). Mice were infected with 500ffu IAV and treated i.p. with 500µg of the blocking antibody, or an isotype control (mouse IgG2b, κ isotype control, clone MPC-11, 0.5mg/ml, BioLegend), diluted in 0.2ml PBS^{-/-} on day 2 pi.

Preparation of BALF and lung tissue single-cell suspension for further analyses

Preparation of BALF for cytokine and cell composition flow cytometry analysis

For cytokine and cell composition analysis of the BALF, mice were sacrificed by exsanguination under anesthesia. To this purpose, xylazine hydrochloride (application 16mg/kg; diluted in 0.9% sterile NaCl to 3.33mg/ml) and ketamine hydrochloride (application 100mg/kg; diluted in 0.9% sterile NaCl plus 3.33mg/ml xylazine hydrochloride to a concentration of 20mg/ml) were applied intraperitoneally at 0.2ml per 20g body weight. Exsanguination was then performed through

puncture of the left ventricle. Following that, the trachea was exposed through an incision in the neck skin and separation of the salivary glands and sternohyoid muscles. A 21G cannula was then inserted in the trachea via a small incision and fixed in place with the help of surgical suture. BALF was collected through repeated steps of orotracheal instillation and extraction of PBS^{-/-}/2mM EDTA. More specifically, instillation of 1.2ml PBS/EDTA (in 0.3ml, 0.4ml, 0.5ml steps, 'first fraction') was followed by instillation of 8x0.5ml PBS/EDTA ('second fraction'). BALF was stored on ice until further processing. Both fractions were centrifuged at 1600rpm for 8min at 4°C, after which pellets were combined, resuspended in 1ml MACS buffer (PBS^{-/-}, 7.4% EDTA, 0.5% FCS pH 7.2), and stored on ice until further analysis. Supernatant of the first fraction containing viral particles and soluble, cell-derived molecules, was aliquoted and stored at -80°C.

Calculation of absolute cell numbers in mouse BALF

For calculation of total cell count and viability assessment in the BALF of naïve, mock- and IAV-infected mice, 19µl of cells resuspended in 1ml MACS buffer were stained with 1µl of acridine orange (AO)/4',6-diamidino-2-phenylindole (DAPI) dye (Solution 18, ChemoMetec). 0.01ml of cell suspension containing the AO/DAPI dye were loaded on a NC-slide A8TM and fluorescence imaging was performed in a NucleoCounter[®] NC-3000TM [ChemoMetec, (DEN)]. Cell count was determined by quantification of cells with positive AO staining as total number of cells in 1ml. Dead cells were identified as AO- and DAPI-positive, thus providing additional information regarding cell viability.

Preparation of lung tissue single-cell suspension for cell composition analysis

After BALF extraction, mouse chest cavity was opened, and lungs were perfused with sterile HBSS via the right heart ventricle. Once 1.5ml of sterile dispase had been administered into the lungs, the cannula was removed, and the trachea was tightly sealed with suture. Lungs and trachea were removed, washed in HBSS, and placed in dispase for 40min at RT. Next, heart, trachea, and large airways were removed, and the remaining lung tissue was dissected in DMEM/2.5% HEPES plus 0.01% DNase in C tubes using the gentleMACS dissociator (Miltenyi Biotec). Cells were filtered through 100 and 40µm cell filters, washed, centrifuged at 1500g/4°C for 10min, resuspended in 1ml DMEM/2.5% HEPES, and counted. For the determination of total cell count, a similar approach to BALF was used (see above) with an additional 1:10 dilution step of the cell suspension (0.9ml MACS buffer + 0.1ml cell suspension) to avoid exceeding the maximal counting range of

the NucleoCounter due to the high cell numbers in the lung tissue. Solution 18 (1µl) was then added to 19µl of the diluted cell suspension and cell count was determined as described above.

Calculation of bacterial burden in the lungs of animals infected with IAV and Streptococcus pneumoniae

For comparison of the bacterial load between different mouse groups following a double infection hit, wild-type and *tnfsf14*^{-/-} mice were infected with low-dose IAV and *Streptococcus pneumoniae*, as described above. On day 9 pi, the first day after co-infection when significant changes in weight loss and clinical scoring could be observed, mice were sacrificed, BALF was collected, and lungs were harvested and homogenized, as previously described. Samples were stored on ice during the complete experimental procedure. A series of inoculum dilutions in NaCl was prepared for each sample in 1:10 steps on a 96-well plate, ranging from 0 to 7 dilutions per sample. For each dilution step, 4x0.01ml inoculum were pipetted on a blood agar plate and left to grow at 37°C overnight. Total bacterial load was then calculated by counting the average number of separately grown colonies, multiplied by 10^{number of dilution step}, for each sample.

Fluorescence activated cell sorting (FACS) of BALF TR-AM

BALF was obtained from mock- and IAV-infected mice as described above. After calculation of total cell numbers, cell suspensions were recentrifuged at 1.5g, 5min, 4°C, blocked with 0.01ml immune globulin blocking solution [10% Gamunex-C (Grifols, USA)/1% BSA/0.02% NaAz], and incubated in the appropriate antibody mixture for 20min at 4°C (**Table 2.**) Cells were washed between staining steps with MACS buffer and resuspended in 0.4ml MACS buffer before sorting. Sytox™ blue (ThermoScientific, USA) was added to BALF samples at a concentration of 1:1000 immediately before sorting. TR-AM were sorted into polypropylene FACS tubes (BD Biosciences, USA) and centrifuged at 1.5g, 5min, 4°C. Cells were then resuspended in 0.35ml RLT buffer (Qiagen, USA) and stored at -80°C for further gene expression analyses.

Table 2. Staining protocol for TR-AM sorting:

Gating strategy	Antibody	Dilution
sorting of viral hemagglutinin-negative (HA-neg) TR-AM from BALF	goat anti-mouse influenza A Virus	1:75
	rabbit anti-goat Alexa Fluor-647/FITC	1:100
	rat anti-mouse CD45 APC/Cy7, Gr-1 PE/Cy7, SiglecF	1:100, 1:100,
	PE, CD11c FITC/PE Cy7	1:50, 1:20
Live-dead staining	Sytox™ blue PacificBlue	1:1000

***In vitro* experiments**

In vitro infection and ultraviolet light (UV) treatment of cultured MDCK II cells

To infect MDCK II cells with IAV, virus stock was diluted in PBS⁺⁺, 0.2% BSA to an MOI of 1. MDCK II cells had been previously seeded á 1Mio cells/well on a 6-well plate and left to grow until a confluence rate of 85-90% had been reached at the time point of infection. Final concentration of the inoculum was calculated as follows:

Number of cells/well*MOI/inoculation volume (in ml) = ffu/ml

Cells were washed with PBS and inoculated with the final virus dilution for 1h 37°C 5% CO₂. In case of the ‘UV-inactivated’ groups, viral inoculum had been previously been subjected to UV-inactivation for 15min, 30min, or 60min, while being kept on ice. After this incubation step, viral dilution was removed and replaced by infection medium containing 0.2% BSA instead of FCS. Infected cells were then kept at 37°C 5%CO₂. On the following day (24h after infection), microscopy analysis of cell cultures was performed to identify any virus-induced cytopathic effect within each group.

Concentration of BALF from naïve and infected mice for ex vivo treatment of TR-AM

For *ex vivo* treatment of alveolar macrophages, the ‘first fraction’ of BALF isolated from mock-infected (‘day 0’) and IAV-infected wild-type and *mfsf14*^{-/-} mice (day 3, day 7 pi) was thawed from -80°C on ice. For each time point of the infection course, samples from three mice were placed in a ThermoScientific™ Pierce™ protein concentrator (2-6ml capacity, Cat. 88515, cut-off 3kDa, ThermoFisher Scientific, USA) and centrifuged at 4000g, 30’, 25°C. Concentrated retentates were collected from sample chambers and underwent 15min UV inactivation to exclude the interference of any remaining viral particles or cell debris with the treatment. Samples were then aliquoted and stored at -80°C or immediately diluted in TR-AM medium for alveolar macrophage treatment.

Viability analysis of ex vivo treated alveolar macrophages

Primary TR-AM were isolated from the BALF of non-infected mice as described above, seeded on a 96-well plate at a density of 50.000-100.000 cells/well, and left to adhere for a minimum of two hours at 37°C, 5% CO₂. Cells were then washed and treated with 0.1ml TR-AM medium containing 10% concentrated BALF from mock- and IAV-infected wild-type mice. For caspase inhibition experiments, cells were incubated in TR-AM medium containing a specific caspase-3/-8 inhibitor

at a concentration of 50 μ M for 3h prior to BALF treatment. This concentration was chosen as sufficient for significantly attenuating staurosporine-induced apoptosis (0.25 μ M) in naïve alveolar macrophages after 24h of treatment while not inducing any significant toxicity. TR-AM viability was then assessed by a colorimetric assay (Cell Counting Kit-8, Sigma Aldrich, GER). More specifically, 0.01ml of the tetrazolium salt WST-8 [2-(2-methoxy-4-nitrophenyl)-3-(4-nitrophenyl)-5-(2,4-disulfophenyl)-2H-tetrazolium] were added to TR-AM cultures 24h after treatment. As WST-8 is reduced by dehydrogenases in living cells, leading to the formation of yellow-colored formazan, viability could be assessed as being proportional to the amount of the newly produced formazan dye. To that purpose, cells were incubated in WST-8 for 1h at 37°C/5% CO₂ and the amount of formazan was quantified as proportional to the absorbance measured at 450nm wavelength in an iMark microplate reader (Bio-Rad, GER). Viability of treated cells was then calculated as follows:

absorbance treated/absorbance control * 100, expressed as % survival of control-treated cells, which was set at 100%.

Caspase activity assays

For caspase activity assays, TR-AM isolated from the BALF of naïve (day 0) or IAV-infected mice (day 3, day 7 pi) were seeded á 10,000-50,000 cells/well on a 96-well plate. After 2h of incubation at 37°C, 5% CO₂, cells were treated with 0.1ml TR-AM medium containing 10% concentrated BALF from wild-type or *tnfsf14*^{-/-} mice for 24h. For *tnfsf14*/light blocking experiments, a specific mouse anti-mouse *tnfsf14*/light blocking antibody (provided by the group of Prof. I. Rodriguez-Barbosa, University of León, León, ES) or an isotype control (mouse IgG2b, κ isotype control, clone MPC-11, 0.5mg/ml, BioLegend, USA) was added to the concentrated BALF at a concentration of 1 μ g/ml and incubated for 1h at 4°C prior to cell treatment, after which concentrated BALF was added and incubation was performed for 24h at 37°C, 5% CO₂. For recombinant *tnfsf14*/light treatment, flow-sorted TR-AM from naïve and IAV-infected mice were plated at a density of 10,000-50,000 cells/well on a 96-well plate and treated with rTnfsf14/Light (R&D Systems, GER) at a concentration of 500ng/ml in TR-AM medium containing PBS^{+/+}/0.1%BSA instead of FCS for 24h. In all experimental setups, lyophilized Caspase-Glo[®] 3/7 or Caspase-Glo[®] 8 substrate (Promega, GER) was resuspended in 10ml luciferase-containing Caspase-Glo[®] buffer (Promega, GER) and added á 0.1ml/well to the cells 24h after treatment. After

1h incubation at RT, cells were transferred to black 96-well plates for luminescence detection with a 520/25 filter in an FLx800 fluorescence and luminescence reader (BioTek Instruments, USA). In this assay, luminescence is produced following caspase cleavage of the pro-luciferin DEVD (for caspase 3/7) or IETD (for caspase 8) substrate and the release of aminoluciferin, leading to luciferase reaction and light emission. Caspase activity was quantified as proportional to luminescence emitted and was expressed as follows:

% Caspase activity (treated) = (caspase activity treated-caspase activity blank) / (caspase activity control-caspase activity blank) *100.

Analysis of gene expression

RNA isolation, cDNA synthesis, and quantitative polymerase chain reaction (qPCR)

For RNA isolation, flow-sorted murine TR-AM and human neutrophils were lysed in 0.35ml RLT buffer, provided in the RNeasy kit (Qiagen, USA), leading to cell lysis, protein denaturation, and RNase deactivation. Samples were processed according to the manufacturer's instructions. RNA was precipitated through the addition of 0.35ml ethanol, bound to a silica membrane, washed, and finally eluted in 0.014ml dH₂O. RNA concentration and quality were measured with the spectrophotometer Nanodrop One (ThermoScientific, USA). For cDNA synthesis, 100-250ng of isolated RNA plus 0.001ml dNTPs, 0.0015ml random hexamers, and dH₂O for a total volume of 0.0125ml were heated up to 65°C for 5min in order to break up secondary RNA structures and linearize the RNA. Samples were then placed on ice for 3-5min. After that, 0.008ml of PCR master mix including a reverse transcriptase needed for transcription of RNA into cDNA were added, according to the manufacturer's instructions. Samples were kept at 25°C for 1min, 37°C for 50min, and then heated up to 70°C for 5min in order to inactivate the reverse transcriptase. All incubation steps were performed in a T100 thermocycler (Bio-Rad, GER). qPCR analysis was performed with SYBR green in the StepOnePlus™ Real-Time PCR System (Applied Biosystems™, USA) and in the QuantStudio™ 3 Real-Time PCR System (Applied Biosystems™, USA) using the reaction setup provided by the manufacturer.

Gapdh and 18s ribosomal rRNA were selected as housekeeping genes and served as normalization controls (**Table 3**). Data are presented as $\Delta\Delta C_t$ [(Ct reference- Ct gene of interest)_{inf/treated} - (Ct reference- Ct gene of interest)_{mock inf/control}] or fold change ($2^{\Delta\Delta C_t}$). Primer specificity was validated by analysis of the melt curve of the qPCR products.

Table 3. Primer pairs used for qPCR.

<i>gapdh</i>	FP 5'-AGGTCGGTGTGAACGGATTTG-3' RP 5'-GGGGTCGTTGATGGCAACA-3'
<i>tnfsf14/light</i>	FP 5'-ACTGCATCAACGTCTTGGAGA-3' RP 5'-TGGCTCCTGTAAGATGTGCTG-3'
<i>tnfrsf14/hvem</i>	FP 5'-CAGGCCCTACAGACAACAC-3' RP 5'-ACTCGTCTCCCACAAGGAACT-3'
<i>ltβr</i>	FP 5'-CCCCTTATCGCATAGAAAACCAG-3' RP 5'-TGCATACCGCAAAGACAAACT-3'
<i>RPS18</i>	FP 5'-GCAGAATCCACGCCAGTACAAG-3' RP 5'-GCTTGTGTCCAGACCATTGGC-3'
<i>TNFSF14/LIGHT</i>	FP 5'-GGTCTCTTGCTGTTGCTGATGG-3' RP 5'-TTGACCTCGTGAGACCTTCGCT-3'

RT² Profiler PCR Arrays

RT² profiler PCR arrays (Qiagen, USA) were used for gene expression analysis of a panel of targets related to different intracellular biological pathways. In detail, RNA was isolated from flow-sorted TR-AM as described before. A total amount of 10ng RNA was used per sample for all further gene expression analyses, which were performed according to the manufacturer's instructions. As a first step, genomic DNA elimination was performed by adding 0.002ml of genomic elimination buffer to 0.008ml of RNA sample. Following incubation at 42°C for 5min, the reaction was stopped by placing the samples on ice for at least one minute. After that, 0.01ml of reverse transcription mix containing 0.004ml of 5x buffer BC3, 0.001ml of control P2, 0.001ml of cDNA synthesis enzyme mix, 0.001ml of RNase inhibitor, and 0.003ml of RNase-free water were added to the original mix and the total of 0.02ml mix was incubated at 42°C for 30min. The enzymatic reaction was then stopped by incubation at 95°C for 5min. Pre-amplification of cDNA targets was performed by addition of 0.0125ml of PCR mastermix (RT² PreAMP PCR Mastermix) and 0.0075ml of a species- and pathway-specific primer mix (PBM-063Z-RT² PreAMP cDNA Synthesis Primer Mix for Mouse TNF Ligands and Receptors, PBM-212Z - RT² PreAMP cDNA Synthesis Primer Mix for Mouse Cell Death PathwayFinderTM, PBM-148Z - RT² PreAMP cDNA Synthesis Primer Mix for Antibacterial Response) to 0.005ml of the cDNA synthesis reaction, as previously described. Samples were heated at 95°C for 10min in order to activate the HotStart DNA *Taq* polymerase,

after which pre-amplification was performed over 14 cycles of incubation at 95°C for 15sec followed by incubation at 60°C for 2min. At the end of the pre-amplification process, 0.002ml of side reaction reducer were added to each preamplified reaction, which was then incubated at 37°C for 15 minutes, followed by heat inactivation at 95°C for 5 min and addition of 0.084ml nuclease-free water. Samples were then placed on ice prior to real-time PCR. PCR components were mixed according to the 96-well plate array format provided by the company (PAMM-063ZC-24-RT² Profiler™ PCR Array Mouse TNF Signaling Pathway, PAMM-212ZC-12-RT² Profiler™ PCR Array Mouse Cell Death PathwayFinder, and PAMM-148ZC-12-RT² Profiler™ PCR Array Mouse Antibacterial Response). More specifically, 1.275ml of 2x RT² SYBR Green mastermix and 1.173ml of RNase-free water were added to 0.102ml of the preamplified samples. Samples were then pipetted á 0.025ml per well in a pre-coated 96-well plate containing 5 housekeeping gene controls for data normalization, 1 genomic contamination control, 3 reverse-transcription controls (testing reverse-transcription reaction efficiency), 3 positive controls (containing a predisposed artificial DNA sequence, testing polymerase chain reaction efficiency), and 84 gene targets belonging to the pathways of interest. Well plates were then sealed with optical adhesive film and centrifuged for 1min at 1000g, RT, in order to remove any remaining air bubbles. Real-time PCR was then performed in the StepOnePlus™ Real-Time PCR System (Applied Biosystems™) and in the QuantStudio™ 3 Real-Time PCR System (Applied Biosystems™) according to the manufacturer's instructions. Once the threshold was set and Ct values were calculated for all wells, data was exported into a blank Excel® spreadsheet for analysis with the company's PCR analysis web-based software (Qiagen GeneGlobe Data Analysis Center).

Single-cell RNA sequencing experiments

To identify the cellular source of tnfsf14/light during the infection course, mice were infected with 500ffu IAV and lungs were harvested on day 3 pi (ext303) and day 7pi (ext294) and subjected to homogenization and preparation of single-cell suspension as described above. Single-cell suspensions were centrifuged at 1500g, 5min, 4°C, washed in MACS buffer (PBS, 7.4% EDTA, 0.5% FCS pH 7,2, 0,01% NaAz), and incubated in 0.05ml of an antibody solution containing immune globulin blocking solution [10% Gamunex-C (Grifols, ES)/1% BSA/0.02% NaAz] and the CD45 APC/Cy7 antibody (BioLegend, Clone 30-F11) in a dilution of 1:100 for 20min at 4°C. Following a washing step with MACS buffer, cells were resuspended in 0.5ml MACS buffer and

stained with 0.0005ml SytoxTM blue (Invitrogen) for dead cell exclusion immediately prior to sorting. 500,000 live leukocytes (defined as Sytox⁻ CD45⁺ cells) were sorted into 0.35ml 0.04% BSA/PBS^{-/-} for library preparation and further processing. Samples were kept on ice between experimental steps. Sorted cells were stained with the acridine orange (AO)/4',6-diamidino-2-phenylindole (DAPI) dye (Solution 18, ChemoMetec). The NucleoCounter[®] NC-3000TM [ChemoMetec, (DEN)] cell counter was used to assess both cell number and viability (90–91%). Following quality control, single cell suspension with ~10,000 cells were loaded onto a Chromium Chip B (10X Genomics). Gel beads in emulsion (GEM) generation, cDNA synthesis and amplification, and library preparation were performed using the Chromium Single Cell 3' Reagent Kit v3.1 (10X Genomics), according to the manufacturer's protocol. Indexed libraries were sequenced on an Illumina NextSeq2000 with a P3 flowcell with 28 cycles for Read1, followed by 8 cycles for barcoding, and 52 cycles for Read2. Prior to analysis, reads were aligned against the mouse genome (GRCm38.p6) and quantified using the StarSolo (<https://github.com/alexdobin/STAR>) RNA-seq aligner. Analysis was conducted with the Scanpy software (<https://github.com/theislab/scanpy>). Quality filtering was done by removing cells with more than 9% mitochondrial reads and cells that were not in a range of 300 to 9000 expressed genes. Thus of 6869 cells, 95 were removed for ext303 and ext294 lost 66 cells out of a total of 7965 cells. Furthermore, genes detected in less than 30 cells were omitted. The remaining cells were then subjected to normalization. Raw cell counts were normalized to the median count over all cells and transformed into log space for variance stabilization. To identify cell clusters, we first did a principal component analysis (PCA). The first 12 components for ext303 and 10 components for ext294 were selected to construct neighbor graphs, as they contained the majority of variance in each dataset. Uniform Manifold Approximation and Projection (UMAP) embedding was performed to identify cell type clusters through Leiden clustering. Additionally, a doublet analysis was conducted on ext294 using the Scrublet software (<https://github.com/swolock/scrublet>), leading to the removal of a doublet cluster (118 cells).

Analysis of protein expression

Enzyme Linked Immunosorbent Assay (ELISA) and Multiplex Assay

A commercially available ELISA kit was used according to the manufacturer's instructions to determine the concentration of tnfsf14/light in the BALF and in the serum of IAV-infected and

mock-infected mice (Mouse LIGHT/TNFSF14 DuoSet ELISA, DY1794-05, R&D Systems), according to the manufacturer's instructions. Colorimetric detection of protein concentration was performed at a wavelength of 450nm in a microplate reader (Bio-Rad). Tnfsf14/light concentrations in different samples were calculated on basis of the optical density measured for samples of known concentrations following subtraction of the zero standard optical density in a standard curve.

For the determination of soluble TNFSF14/LIGHT in the human lung upon severe viral pneumonia, BALF from patients treated in the intensive care unit of the University Clinic of Giessen following severe IV pneumonia or COVID-19, or patients undergoing bronchoscopy for other diagnostic purposes, was obtained under written consent. In the latter case, 'healthy' samples were selected when a percentage of alveolar macrophages higher than 90% could be determined by cytospin analysis. Use of BALF samples had been previously approved by the University of Giessen Ethics Committee. Samples were concentrated in ThermoScientific™ Pierce™ protein concentrators (0.1-0.5ml capacity, Cat. 88512, cut-off 3kDa, ThermoFisher Scientific, GER) by centrifugation at 12000g, 30', 25°C. ELISA of the concentrated retentates was performed using a commercially available kit (Human LIGHT/TNFSF14 Quantikine ELISA Kit, DLIT00, R&D Systems), according to the manufacturer's instructions. Optical density was determined at 450nm on a microplate reader (Bio-Rad). Ligand concentrations were calculated on basis of samples of known concentrations in a standard curve, as described above for the mouse ELISA.

For multiplex analysis, the Bio-Plex Pro Mouse Cytokine 23-plex Assay was used (Bio-Rad, XMAP Technologies) according to the manufacturer's instructions. Cytokine analysis was performed in the BALF of wild-type and *tnfsf14*^{-/-} mice. All measurements were performed in a Bio-Plex MAGPIX multiplex reader (Bio-Rad, XMAP Technologies).

Flow cytometry analysis of immune cell populations in the BALF and in lung tissue single-cell suspension

Multicolor flow cytometric analysis was performed on an LSR Fortessa using DIVA software (BD Biosciences). In summary, BALF and lung tissue were obtained from naïve and IAV-infected mice as described above. After calculation of total cell numbers, cell suspensions were recentrifuged at 1500g, 5min, 4°C, and resuspended in FACS buffer (PBS, 7.4% EDTA, 0.5% FCS pH 7.2, 0.01% NaAz) containing immune globulin blocking solution [10% Gamunex-C (Grifols, ES)/1%

BSA/0.02% NaAz]. Cells were then incubated in the appropriate antibody mixture for 20min at 4°C (**Table 4**). Following a washing step with FACS buffer, cell were routinely stained either for 5min with 7-AAD (BioLegend, USA) or immediately before analysis with Sytox™ blue (Invitrogen, USA) for dead cell exclusion. Gating strategies and antibody concentrations were set with the help of corresponding isotype antibodies which served as negative controls. Data analysis was performed with the FlowJo™ v10.7 software (BD Biosciences, USA).

Table 4. Staining protocol for immune and structural cell population analysis from BALF and lung tissue.

Gating strategy	Antibody	Dilution
1: innate immune cell populations (BALF)	CD45 APC/Cy7, Ly6G APC, SiglecF BV421, CD11c PE/Cy7, CD11b FITC	1:100, 1:50, 1:50, 1:20, 1:50
2: HA expression in TR-AM (BALF)	goat anti-mouse influenza A Virus rabbit anti-goat Alexa Fluor-647 rat anti-mouse CD45 APC/Cy7, Gr-1 PE/Cy7, SiglecF PE, CD11c FITC	1:75 1:100 1:100, 1:100, 1:50, 1:20
3: adaptive immune cell populations (BALF, lung tissue)	CD45 APC/Cy7, NK1.1 APC, CD3 FITC	1:100, 1:50, 1:50
4: innate immune cell populations (lung tissue)	CD45 APC/Cy7, CD206 APC, CD24 PE/Cy7, Ly6C FITC, CD11b Pacific Blue	1:100, 1:20, 1:200, 1:50, 1:50
5: immune and structural cell populations (lung tissue)	CD45 PE/Cy7, CD31 eF488, CD326 APC/Cy7	1:100, 1:50, 1:50
6: Tnfsf14/Light receptor expression on TR-AM	CD45 PE/Cy7, SiglecF APC/Cy7, CD11c FITC, LTβR PE, HVEM APC	1:100, 1:50, 1:20, 1:50, 1:50
7: live-dead staining	7-AAD Sytox™ blue	Gating strategies 1,4. Gating strategies 2,3,5,6.

Phagocytosis assay

Phagocytosis capacity of wild-type and *tnfsf14*^{-/-} BALF TR-AM was compared on day 7 pi using the pHrodo™ Green *E. coli* BioParticles™ phagocytosis kit for flow cytometry (Invitrogen). BALF cells were collected and total cell count was performed as described above. BioParticles™ conjugates were reconstituted in 0.44ml of Buffer B, vortexed for 1min, and sonicated for 15min in order to achieve an even particle distribution. Reconstituted bacterial conjugates were stored on ice for 10min until further use. Each BALF sample was then divided into four samples and

centrifuged at 1500g, 5min, 4°C. Two samples per original samples were resuspended in medium containing reconstituted conjugates in a 1:5 dilution and the other two only in medium (total of 0.12ml per sample). Sample pairs (conjugates and empty controls) were then incubated either in a water bath at 37°C or at 4°C for 15min, after which all samples were placed on ice to stop the phagocytosis process. After the addition of 0.1ml Lysis Buffer A per sample, a series of washing steps was performed, then antibody staining was performed and immune cell populations in the BALF were identified via flow cytometry analysis (**Table 4**, gating strategy 1 without CD11b).

Microscopy

Fixation and preparation of lung tissue for hematoxylin-and-eosin (HE) staining and histological analysis

For histological staining of mouse lung tissue, lungs were clipped at the trachea before opening of the chest cavity, then removed and fixed for 24h in 4% PFA. Lungs were then processed in a Tissue-Tek VIP sample preparation system according to the following steps:

Water 50min, 70% ethanol 50min, 80% ethanol 50min, 96% ethanol 50min (twice), 100% ethanol 50min (twice), xylene 50min (twice), paraffin 50min (twice), paraffin 1h (twice). All steps from water to xylene were performed at 37°C, paraffin steps were performed at 60°C. After the last step, tissue was embedded in paraffin (Myr EC 350-1), then cooled down for 5-8min at -8°C on a Myr EC 350-2 cooling plate and sliced in 3-5µm thick sections on adhesive slides (Star Frost), using the microtome Leica RM2235. Sections were left to dry overnight (60°C) before proceeding with the HE staining as follows:

Xylene 3min, xylol 3min, then 2min, 100% ethanol 1min (twice), 96% ethanol 1min, 80% ethanol 1min, 70% ethanol 1min, water 1min 30sec, hematoxylin 8min, water 5min, eosin 30sec, water 5sec, 70% ethanol 5sec, 80% ethanol 5sec, 96% ethanol 1min, 100% ethanol 1min, then 2min, xylene 2min (four times). All steps were performed in the Leica Autostainer XL. At the end of the staining, sections were coverslipped in the automated Leica CV5030 coverslipper machine. Pictures were taken with an Olympus BX 41 microscope and an EVOS® FL Auto microscope (*life technologies*, ThermoFisher).

Each lung was evaluated for the presence of following characteristic lesions: hemorrhage, alveolar and perivascular edema, perivascular infiltrates, pleuritis, steatitis, bronchitis, tracheitis, and bronchus-associated lymphoid tissue (BALT) formation. According to the extent of the above-

mentioned parameters, an injury grading system from 0-4 was developed as follows: 0: not present, 1: minimal, 2: low, 3: medium, 4: high. Total histological pneumonia score was calculated as the sum of each individual score and normalized to the total score of mock-infected mice.

Immunohistochemistry of lung tissue

Paraffin slides were prepared as described above. After overnight incubation at 60°C, deparaffinization and rehydration were performed as follows:

Xylene 10min (twice), 100% ethanol 3min (twice), 96% ethanol 3min (twice), 70% ethanol 3min. Blocking of endogenous peroxidase was performed through incubation with 20ml H₂O₂ 30% in 180ml PBS for 15min at RT. After rinsing with distilled water for three times and an additional incubation step in distilled water for 10min at 37°C, antigen retrieval was performed through the addition of a protease (0,1g protease from *Streptomyces griseus*, Pan Reac AppliChem, ITW Reagents, activity: 10474,48 U/mg) in 100ml PBS for 10min at 37°C. After rinsing with PBS for three times, slides were installed in coverplates and placed in racks, where they were rinsed for an additional three times with Triton/PBS. Following that, blocking serum (PBS, Roti-ImmunoBlock (Roth) and goat normal serum) was applied for 30min at RT, then the primary antibody (TNFSF14 ab203578, goat-anti-rabbit, dilution1:300) was applied overnight at 4°C. On the following day, slides were rinsed three times with Triton/PBS, incubated in the secondary antibody [goat-anti rabbit IgG (H+L), biotinylated, BA-1000 (Vector Laboratories)], and rinsed three times with Triton/PBS. After that, peroxidase belonging to the VECTASTAIN ABC-HRP Kit (Vector Laboratories) was applied to the slides, according to the manufacturer's instructions. Slides were then rinsed three times with distilled water, stained with 3,3-diaminobenzidine [DAB buffer tablets, Merck KGa, 4 tablets in 0.2ml distilled water, 0.02ml 30% H₂O₂ (ROTIPURAN)], rinsed again three times, and stained with hematoxylin for 1min. Slides were rinsed again until no staining solution remained visible and incubated in water for 10min at RT. Finally, dehydration was performed through the following steps:

70% ethanol 3min (twice), 96% ethanol 3min (twice), 100% ethanol 3min (three times), xylene 2min (three times). Slides were then coverslipped using the Leica CV5030 automated coverslipper machine. Pictures were taken with the Olympus BX 41 microscope using the cellSens imaging software (Olympus Corporation ver. 1.18) and were subsequently edited with Photoshop CS5 (64 bit). Tnfsf14/Light expression was determined in a semi-quantitative manner based on the

frequency of positive signal in the lung parenchyma, the bronchi (both in the intact and in the influenza-associated damaged areas), as well as the pleura. Tnfsf14/Light expression scoring ranged between 0, when no signal was present, and 4, when the protein was highly abundant in the examined tissue.

Human samples

Human BALF and flow-sorted BALF neutrophil samples were obtained from patients who underwent bronchoscopy due to an underlying, non-inflammatory, pulmonary disease (samples containing >90% alveolar macrophages as measured by cyto-spin) or patients who had been admitted to the ICU of the University Clinic of Giessen following virus-induced pneumonia. Written consent had been acquired either from the patients or from a legal guardian or legally authorized patient relative. Use of human lung neutrophil and BALF samples was approved by the University of Giessen Ethics Committee.

Statistics

All data are given as mean \pm SEM. Statistical significance of two groups was analyzed by unpaired Student's t test. Statistical difference of three or more groups were analyzed by one-way or two-way ANOVA and post-hoc Tukey or Kruskal-Wallis and post-hoc Dunn's comparison test (GraphPad Prism 9). A p-value less than 0.05 was considered significant, * $p < 0.05$; ** $p < 0.01$; *** $p < 0.005$.

4. Results

Pre-existing influenza A virus (IAV) infection enables the establishment of secondary pneumococcal pneumonia

Secondary infection with bacterial pathogens such as *Streptococcus pneumoniae* (*Spn*) is a common complication of severe primary IAV infection, with dramatic implications for clinical course and disease outcome [127, 133]. In order to study the pathomechanisms behind it, a co-infection model needed to be established, which would cause significant disease severity but would still permit comparisons among different mouse groups. Single infection with 500 foci forming units (ffu) IAV A/PR/8/34 (PR8) administered orotracheally to C57Bl/6 wild-type mice led to substantial mortality and weight loss, while a single infection with 2000 colony forming units (cfu) *Spn* administered intranasally had no impact on survival or weight loss 14 days after infection (Figure 10 A, B).

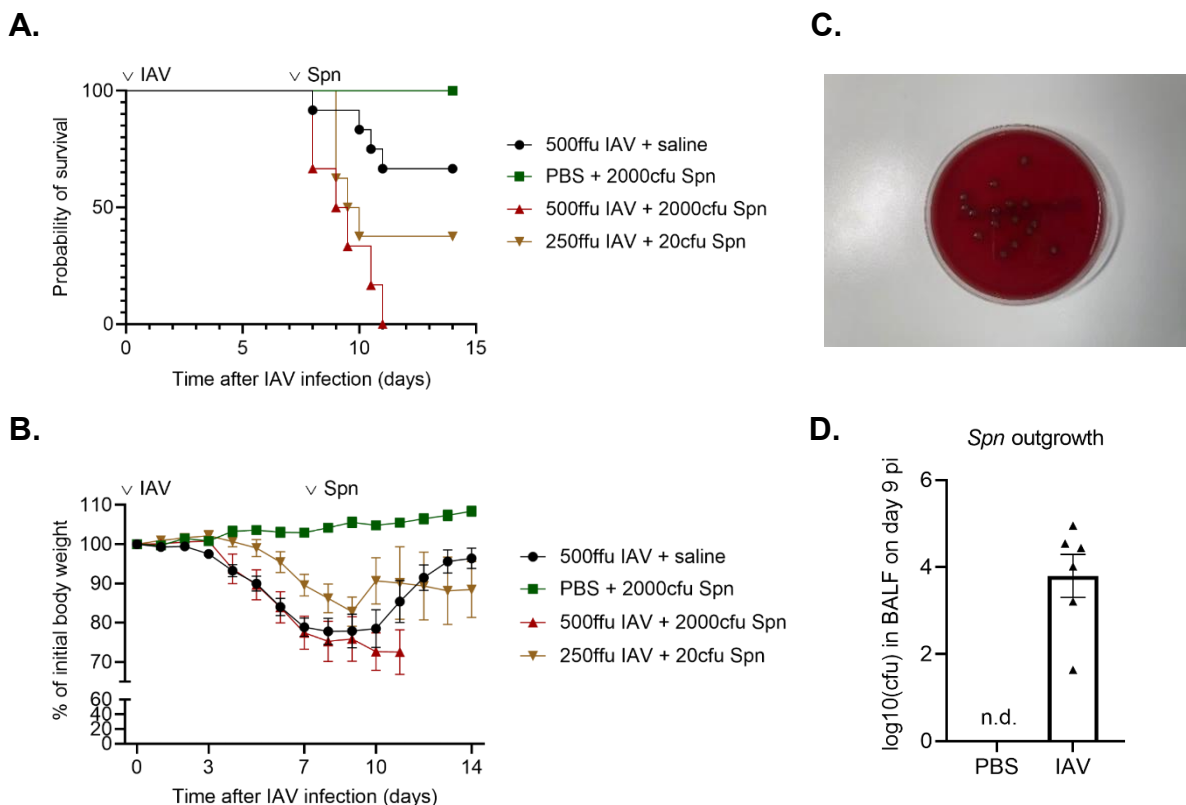


Figure 10. Pre-existing IAV pneumonia enables the establishment of post-influenza pneumococcal pneumonia. (A-B) Survival and weight loss after orotracheal infection of C57Bl/6 wild-type mice with IAV and/or intranasal

pneumococcal infection on day 7 pi at different doses, as observed over fourteen days after initial IAV infection. (C) Bacterial culture on a blood agar plate as used in the established co-infection model. For this low-dose model, an amount of 20-50cfu *Spn* was used on day 7 pi following an initial infection with 250ffu IAV. (D) Despite the low infection inoculum, pre-existing IAV infection on day 0 led to a high bacterial burden in the BALF of co-infected wild-type mice on day 9 pi (2 days after pneumococcal infection), as opposed to mock infection on day 0. Data shown are pooled from four different experiments, n=6-8, mean \pm SEM is depicted.

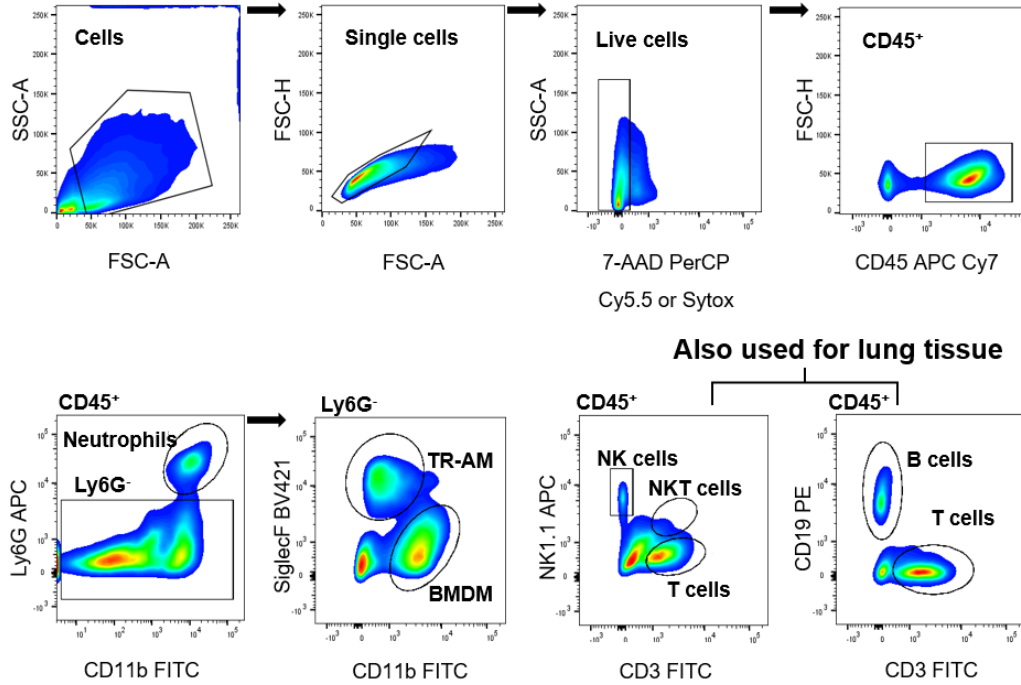
However, when pneumococcal infection was preceded by IAV infection, all mice had to be euthanized due to high disease burden, according to the scoring criteria mentioned in the 'Methods' section (**Table 1**). For this reason, both infection doses were reduced and a co-infection model of 250ffu IAV on day 0 and approximately 20cfu (experimental variance 20-50cfu) *Spn* on day 7 post-IAV infection (pi) was established, which led to an average of 37.5% survival on day 14 pi (**Figure 10 A**). Despite the low viral and bacterial (**Figure 10 C**) inoculum, high bacterial titers were detected in the lungs of IAV/*Spn* co-infected mice on day 9 pi, compared to PBS/*Spn* –infected mice, which could entirely clear pneumococcal infection (**Figure 10 D**). Day 9 pi was chosen as the first time point when a significant reduction in weight as well as clinical deterioration could be observed following the low-dose, double-infection hit. Having established a reproducible two-hit disease model, the pathomechanisms of increased vulnerability towards pneumococcal infection following primary IAV-induced pneumonia were further investigated, in particular the role of tissue-resident alveolar macrophage (TR-AM) depletion.

IAV-induced pneumonia is characterized by the depletion of the TR-AM pool and the intra-alveolar influx of recruited immune cells at distinct time points over the infection course

In order to elucidate the underlying mechanisms driving TR-AM death upon IAV-induced pneumonia, a valid and reproducible infection time course had to be established, which would enable the identification of the critical time point(s) for TR-AM depletion. To this purpose, wild-type C57Bl/6 mice were orotracheally infected with 500ffu of IAV, a dose which had been previously proven sufficient for causing severe infection with a strong intra-alveolar inflammatory response [98, 146]. Flow cytometry analysis was performed at different time points after infection using diverse gating strategies, aiming at addressing the complexity of BALF (**Figure 11 A**) and lung tissue cell composition (**Figure 11 B**), according to previously published studies on the analysis of lung leukocyte populations [38, 42]. Starting on day 3 pi, a significant decrease in TR-

AM numbers could be observed until day 7 pi, followed by gradual replenishment by day 14 pi (Figure 12 A).

A. BALF



B. Lung

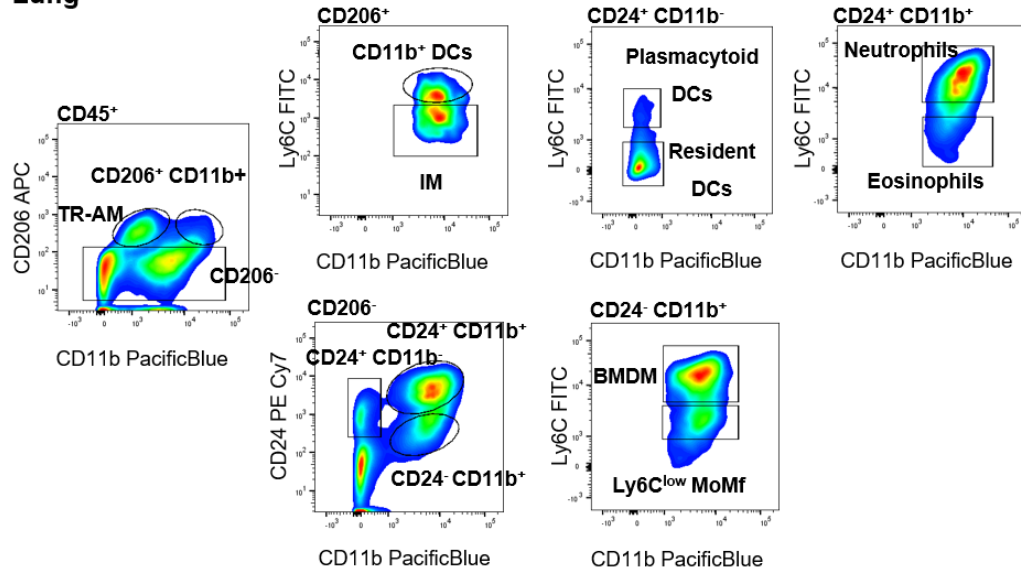


Figure 11. Gating strategy for flow cytometry analysis of different immune cell populations in the BALF and lung tissue over the course of IAV-induced pneumonia. Representative plots of multicolor staining for BALF and lung immune cells. All gating strategies were set according to the appropriate isotype and fluorescence minus one (FMO) controls. TR-AM: tissue-resident alveolar macrophages, BMDM: bone marrow-derived macrophages, NK: natural killer, IM: interstitial macrophages, DCs: dendritic cells, MoMf: monocytes/macrophages.

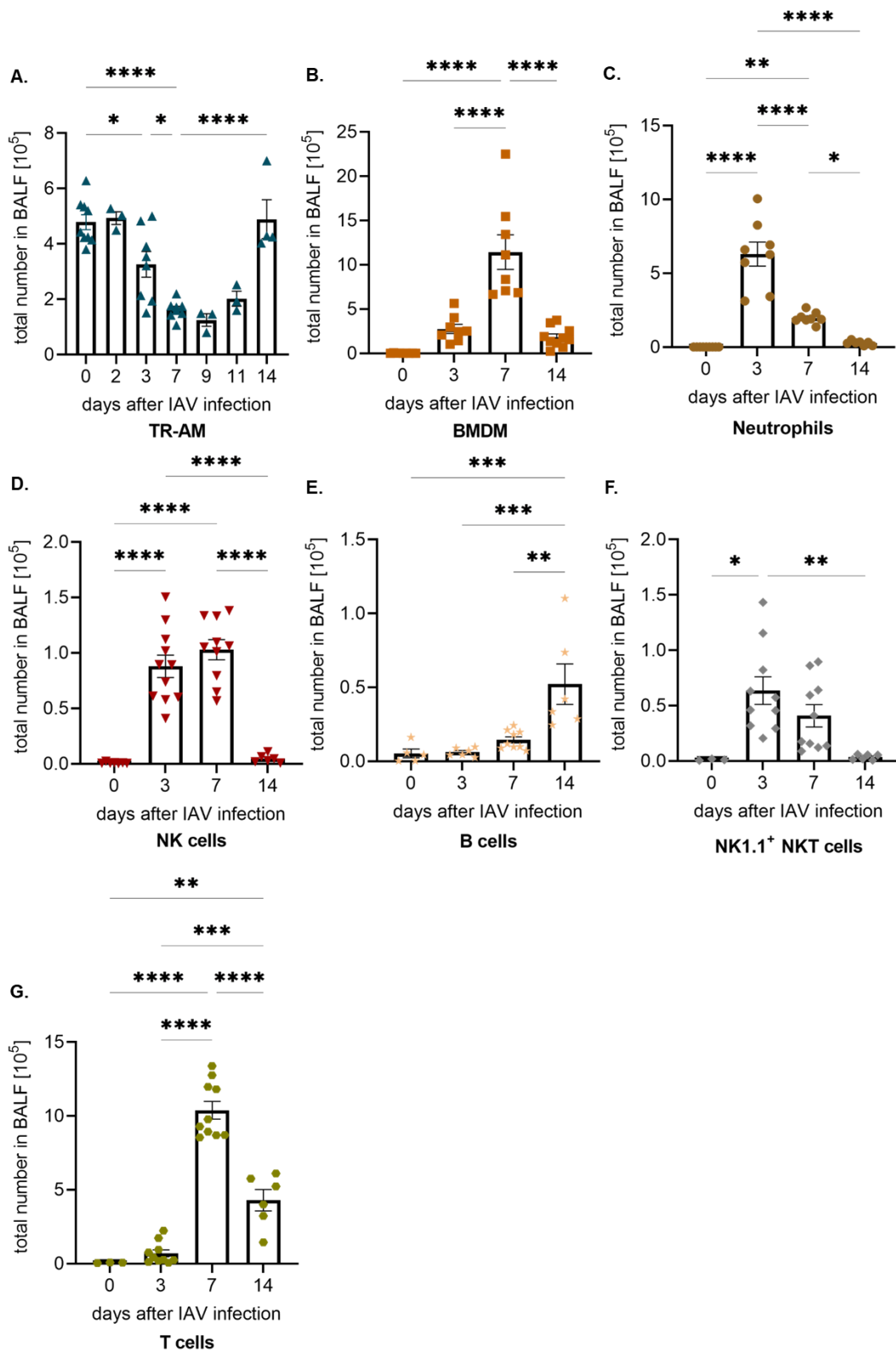


Figure 12. Kinetics of different immune cell populations in the BALF of infected mice over the course of IAV infection. (A-G) C57Bl/6 wild-type mice were infected with 500ffu IAV. BALF was collected at different time points after infection and, following determination of total cell count, surface staining was performed for flow cytometry analysis of immune cell population kinetics. Data shown are pooled from five different experiments, n=3-11, mean \pm SEM is depicted.

Early upon infection, bone marrow-derived macrophages (BMDM), neutrophils, natural killer (NK) cells, and natural killer T (NKT) cells entered the inflamed alveoli, while the presence of T and B cells was more prominent as infection progressed (**Figure 12 B-G**).

Similar kinetics could be observed for the more complex network of immune cell populations found in single-cell suspension from homogenized lung tissue of infected animals during the infection course. Resident populations including interstitial macrophages (IM), CD11b⁺, and CD11b⁻ resident dendritic cells (DCs) diminished during the acute phase (**Figure 13 C, G, I**), while the numbers of Ly6C^{low} monocytes/macrophages remained relatively unchanged (**Figure 13 D**).

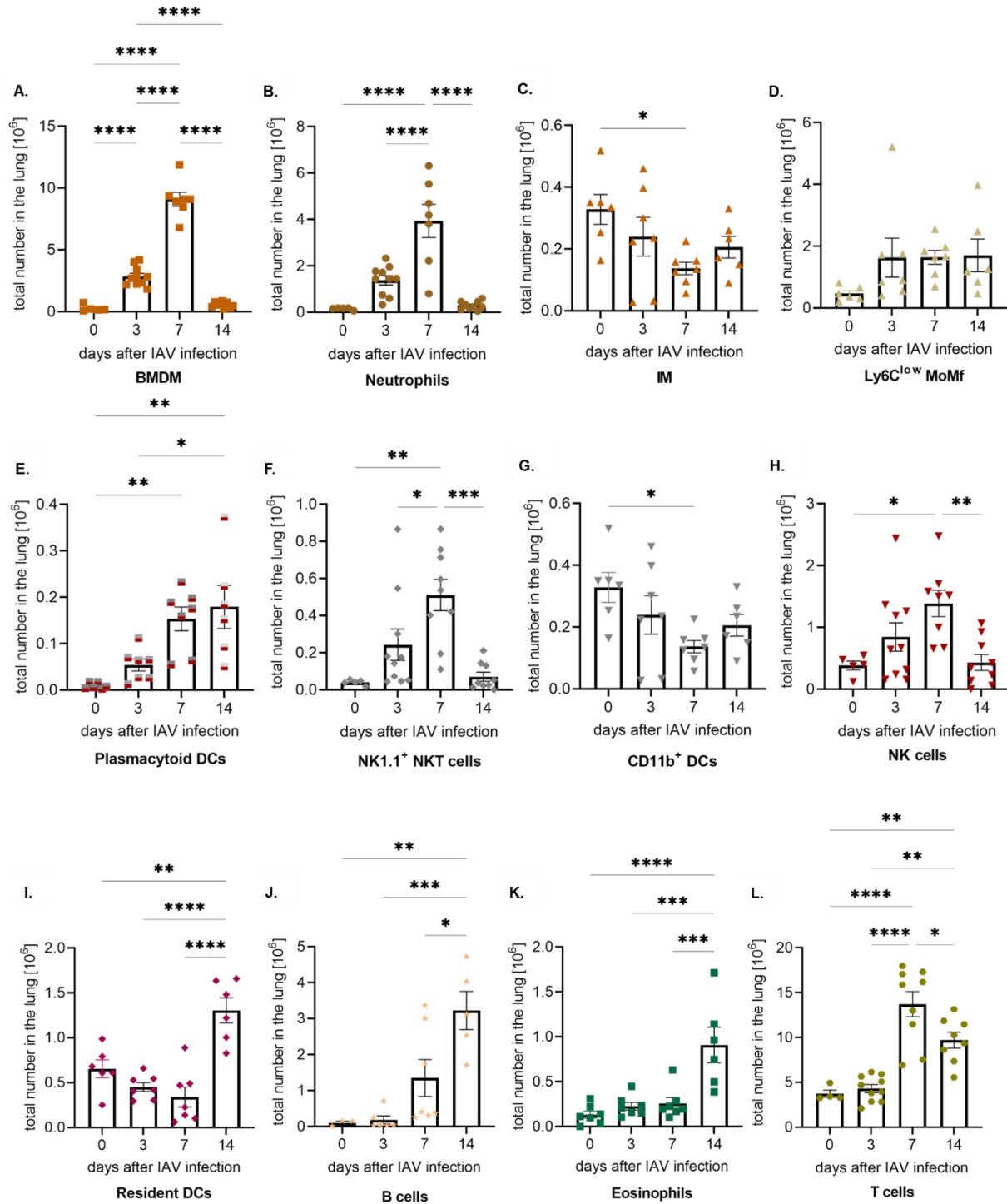


Figure 13. Kinetics of immune cell populations in lavaged lungs (A-L) of infected mice over the course of IAV infection. C57Bl/6 wild-type mice were infected with 500ffu IAV and lungs were collected at different time points after infection, following BALF harvesting. Single-cell suspensions were stained with different antibody combinations

and subjected to flow cytometry analysis in order to establish the different immune cell population kinetics within the lung parenchyma. Data shown are pooled from five different experiments, n=3-11, mean \pm SEM is depicted.

Instead, pro-inflammatory BMDM, which are high on Ly6C expression, neutrophils, plasmacytoid DCs, and NK(T) cells entered the alveoli during the early infection phase (**Figure 13 A, B, E,F, H**). B and T cells were present from day 7 pi on at high numbers (**Figure 13 J, L**), reflecting the recruitment and expansion of these cell populations following signalling from innate immune cells. Interestingly, an increase in eosinophil numbers was observed during the late time points of infection (**Figure 13 K**), potentially demonstrating barrier destruction which enabled the influx of immune cells with a high pro-inflammatory potential into the alveoli. Having set the timeframe for immune cell population kinetics upon IAV-induced pneumonia, and more importantly the key time points of TR-AM depletion, further focus was placed on dissecting the death-inducing pathways within this population.

Apoptosis drives TR-AM death upon IAV-induced pneumonia and is largely independent of direct viral infection

IAV infection leads to the apoptosis of infected alveolar epithelial cells [58]. In order to determine whether this was the underlying mechanism behind TR-AM death as well, BALF TR-AM were examined for the expression of viral hemagglutinin (HA) during the course of IAV infection as a measure of direct viral infection. As viral titers in the lung decrease over time [98], this analysis involved the early infection period. Although a significant decrease in the numbers of HA-negative macrophages could be observed, HA-positive TR-AM were hardly detected and remained relatively unchanged over the course of infection (**Figure 14 A**). This suggested that direct viral infection is not the main driving force behind TR-AM death upon IAV-induced pneumonia. This hypothesis was supported by a further experimental series, where *ex vivo* treatment of naïve TR-AM with UV-inactivated BALF from day 7 pi (when TR-AM depletion is at its severest level) significantly impaired 24h survival post-treatment, as shown in a cytotoxicity assay (**Figure 14 B**). UV irradiation for 15min had been previously proven sufficient in abolishing any virus presence, measured by the cytopathic effect in IAV-infected MDCK cultures (**Figure 14 C**) and was applied in all following experiments involving *in vitro* BALF treatment. These experiments suggested that the observed cytotoxic effect could be attributed to the presence of a soluble, death-inducing agent, present in the BALF of infected animals.

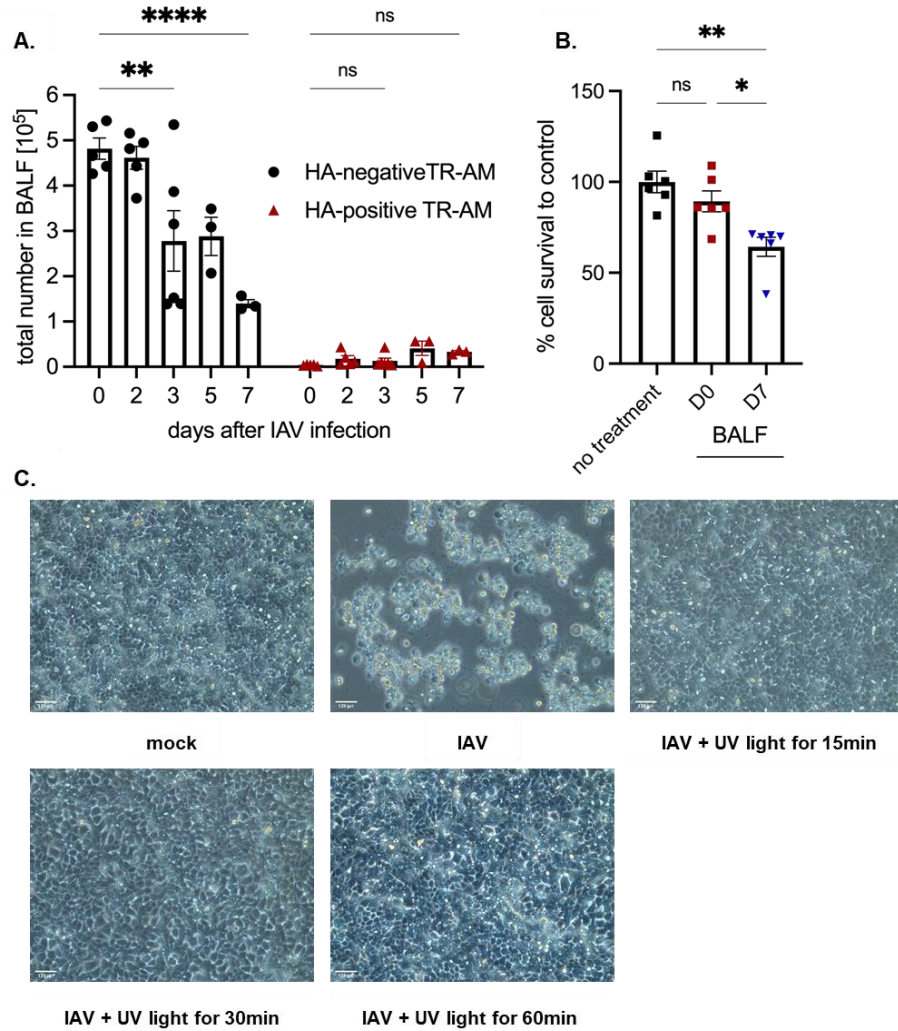


Figure 14. TR-AM depletion can occur independently of direct viral infection upon IAV-induced pneumonia.

(A) Quantification of viral hemagglutinin (HA)-positive and HA-negative TR-AM in the BALF of infected C57Bl/6 mice over the course of IAV infection by flow cytometry. Bar graphs represent means \pm SEM of n=3-6 mice per time point. (B) TR-AM survival 24h after treatment with UV-irradiated BALF from non-infected (day 0) or infected mice from day 7 pi, as assessed by a colorimetric dehydrogenase assay. Cell viability was assessed as absorbance measured at 450nm wavelength and is depicted as percentage of control for each condition. Bar graphs represent means \pm SEM of 3 independent experiments. (C) Microscopy analysis of MDCK II cells infected with MOI 1 of IAV for 24h with or without prior UV inactivation of the viral inoculum for different time intervals (15min, 30min, 60min).

IAV infection can lead to cell death through a variety of different pathways [190], which raised the question which intracellular process was the main driver behind TR-AM depletion. Over time, an increase in the percentage of apoptotic TR-AM was observed in the BALF of infected mice, as defined by the percentage of Annexin V-positive, 7-actinomycin D (7-AAD)-negative TR-AM

(**Figure 15** A and B). Fluorophore-conjugated Annexin V is widely used as a marker of apoptosis, as it binds with high affinity to phosphatidylserine residues normally found on the cytoplasmic side of the cell membrane, which only become accessible upon apoptosis through translocation to the outer membrane surface. As cells transition from apoptosis to death, loss of membrane integrity allows DNA-intercalating dyes like 7-AAD to enter the cytoplasm, thus allowing the distinction of live, apoptotic, and dead cells by flow cytometry [191].

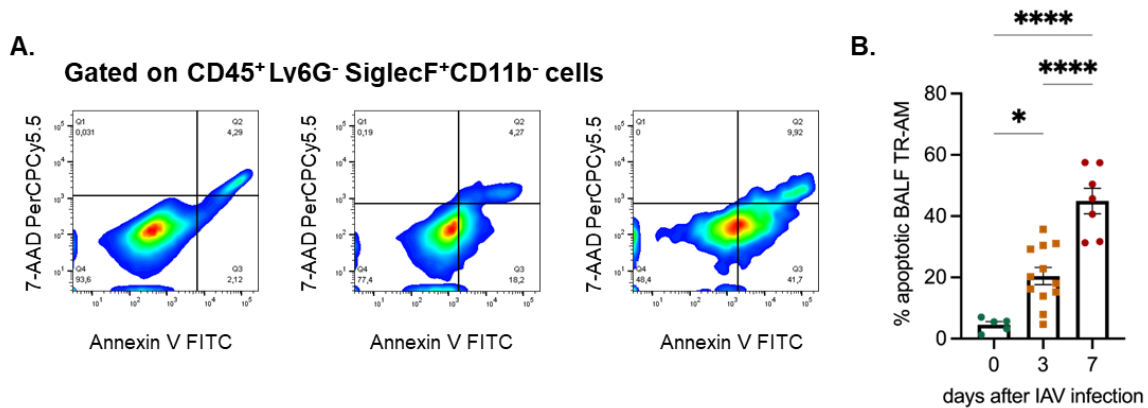


Figure 15. Flow cytometry analysis of Annexin V⁺ 7-AAD⁻ TR-AM over the course of IAV infection. (A) Representative plots of the gating strategy for flow cytometry analysis of BALF TR-AM of non-infected (day 0) and infected wild-type mice on day 3 and 7 pi, stained with Annexin V and 7-AAD. (B) Quantification of the percentage of apoptotic TR-AM (Annexin V⁺ 7-AAD⁻) in the BALF at these time points. Graph represents means ± SEM of n=5-11 mice, pooled from 2-3 different experiments per time point.

Flow-sorted, HA-negative TR-AM revealed an upregulation of several apoptosis- (**Figure 16 A i**), autophagy- (**Figure 16 A ii**), and necrosis-related genes on day 3 and day 7 pi (**Figure 16 A iii**), compared to TR-AM from non-infected mice. However, the apoptosis pathway seemed to be the predominant one, particularly on day 7 pi. In addition to that, BALF treatment of naïve TR-AM led to a significant increase in caspase-3 (**Figure 16 B**) and caspase-8 activity (**Figure 16 C**) 24h later, particularly when BALF from day 7 pi was used. This further added to the hypothesis that TR-AM death is driven by a soluble ligand, which initiates the apoptosis pathway within these cells.

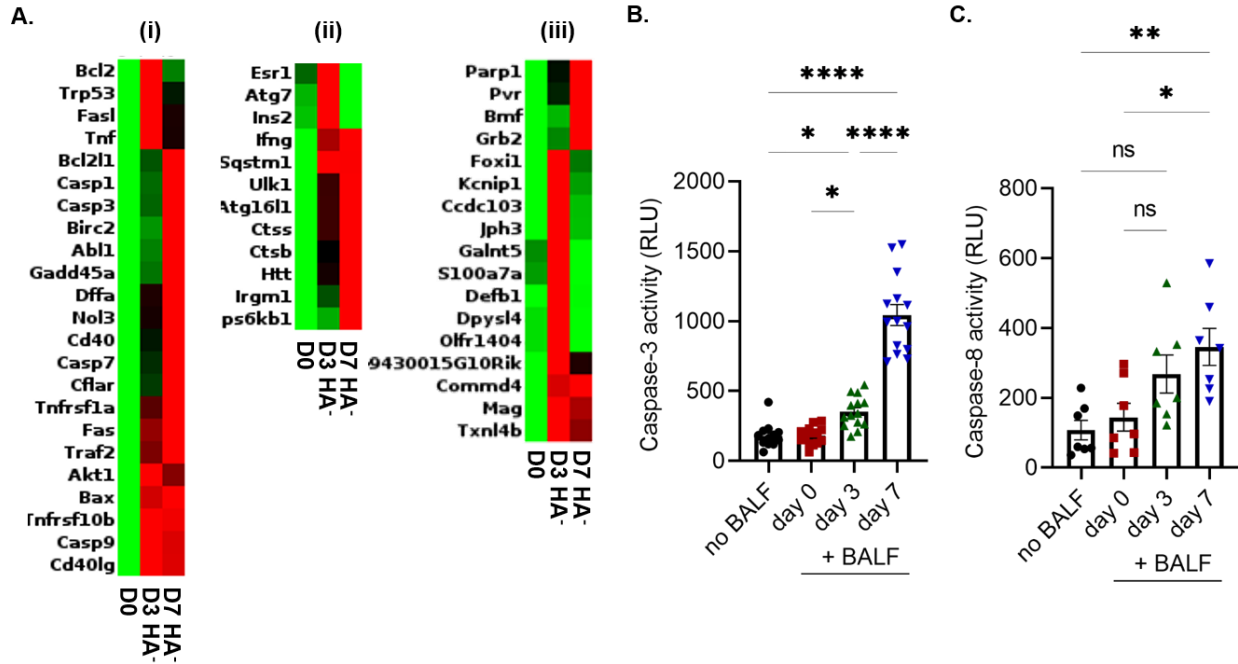


Figure 16. TR-AM death in IAV-induced pneumonia is linked to caspase-dependent apoptosis. (A) Gene expression analysis of flow-sorted HA-negative TR-AM over the course of IAV infection (day 0, day 3, day 7) using the RT² Cell Death PathwayFinder® assay. Genes were grouped into three different cell death pathways, namely apoptosis (i), autophagy (ii) and necrosis (iii), n=3-4 mice were used per time point. Heat maps were created using the company's online software. (B-C) Caspase-3 and caspase-8 activity upon TR-AM treatment with BALF from mock- or IAV-infected C57Bl/6 mice. Cells were seeded at 20,000-50,000/well/0.1ml on a 96-well plate and treated with UV-inactivated BALF in a 1:10 dilution. After 24h, 0.1ml of a reagent mix containing proluciferin-bound caspase-3 or caspase-8 substrate and luciferase were added to the cells for 1h. Caspase activity was then measured as luminescence emission on a luminescence reader. Medium-only controls were used for normalization. Graphs represent means ± SEM of 3-6 independent experiments.

Post-influenza TR-AM depletion can be attenuated by the use of specific caspase inhibitors

Having established that apoptosis is the main pathway leading to TR-AM depletion upon IAV-induced pneumonia, the use of caspase inhibitors as a preventive approach against TR-AM loss was tested. To this end, naïve TR-AM were *in vitro* treated with UV-inactivated BALF from infected wild-type mice (day 7 pi) and compared to their respective non-treatment and mock-infected controls. A specific caspase-3 or caspase-8 inhibitor or a DMSO control was added to the cells at a concentration of 50 μ M 3h prior to treatment and survival was assessed 24h later through a colorimetric assay. The concentration of 50 μ M had been previously established for both inhibitors as being non-toxic to TR-AM, yet sufficient to attenuate staurosporine-induced apoptosis, prior to BALF treatment experiments (**Figure 17 A and B**). Inhibition of caspase-3 only showed a minor protective effect, whereas TR-AM survival was significantly improved when a caspase-8 inhibitor was used (**Figure 17 C**). Based on these results, the effect of caspase inhibition on TR-AM survival was tested over the course of *in vivo* infection. Wild-type mice were infected orotracheally with IAV and treated with a single subcutaneous injection of 10mg/kg of a caspase-3 inhibitor, a caspase-8 inhibitor, or a DMSO control on day 2 pi for analysis on day 3 pi, or with daily injections (day 2 pi to day 6 pi) for analysis on day 7 pi. As caspase inhibition may attenuate viral replication [192], a higher viral dose of 1000ffu IAV was chosen for the short day 3 pi experiments. Viral titers showed no significant difference on day 3 pi (**Figure 17 D**); however, mice showed an attenuated weight loss on day 6 pi and day 7 pi when a caspase inhibitor had been used (**Figure 17 E**). Caspase inhibition completely abrogated TR-AM depletion on day 3 pi (**Figure 17 F**) and significantly attenuated TR-AM loss on day 7 pi, compared to the DMSO control (**Figure 17 G**). These results demonstrate that blocking of the apoptosis pathway at its beginning can preserve a significant part of the TR-AM pool and caspase-8 is pivotal to that purpose. As caspase-8 often serves as the intermediate between extracellular signals and intracellular death pathways [193], these data further corroborated the hypothesis of a soluble, death-inducing ligand being responsible for TR-AM death. The identity of this ligand was the subject of a further experimental series.

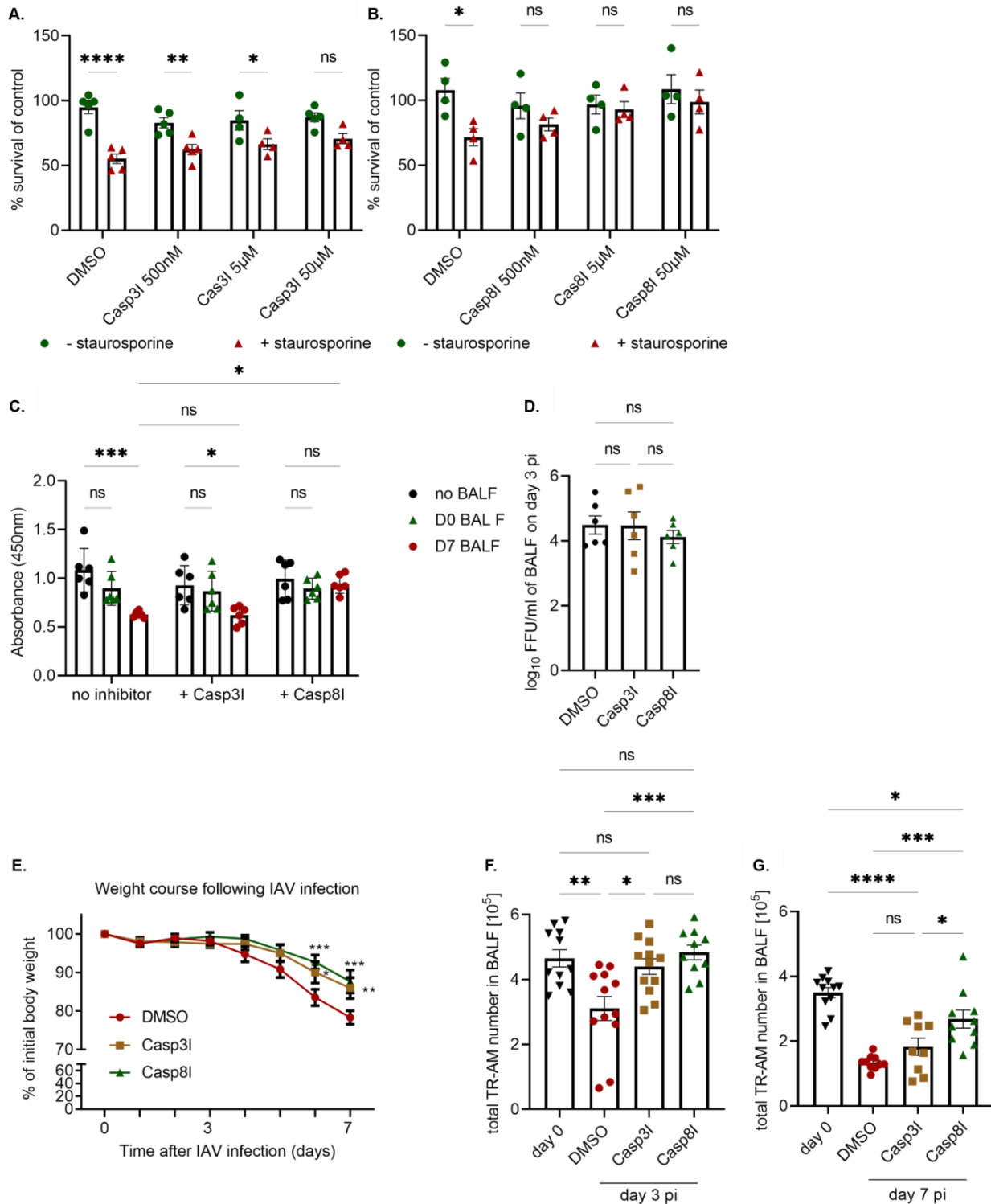


Figure 17. Apoptosis inhibition attenuates TR-AM depletion upon IAV-induced pneumonia. (A-B) Colorimetric viability assessment upon treatment of naïve TR-AM with different doses of a caspase-3 (A) or a caspase-8 (B) inhibitor and/or 0.5µM staurosporine. Cells were seeded á 100,000/well/0.1ml medium on a 96-well plate and treated for 24h. WST-8/CCK8 solution was added to the culture on the following day, leading to the formation of yellow-

colored formazan. Viability was quantified as proportional to the amount of formazan, as measured on a microplate reader, values are depicted as % survival of control (DMSO, no staurosporine). Graphs represent means \pm SEM of 3 different experiments. (C) Colorimetric viability assay upon BALF treatment of naïve TR-AM following pre-treatment with a specific caspase inhibitor. Cells were seeded at 100,000/well/0.1ml medium on a 96-well plate, pre-treated with 50 μ M caspase-3 or 8 inhibitor -or DMSO- for 3h and treated with UV-inactivated BALF in a 1:10 dilution for 24h. Viability was quantified as proportional to the amount of formazan, as measured on a microplate reader. Graph represents means \pm SEM of 3-6 independent experiments. (D) Viral titers as measured per foci forming assay on day 3 pi in the BALF of infected mice, which were treated with a caspase inhibitor or a DMSO control on day 2 pi. (E) Weight curve of IAV-infected mice treated with a caspase-3 or 8 inhibitor, or a DMSO control up to day 7 pi. Graphs represent means \pm SEM of 8-11 mice per group. (F-G) Quantification of BALF TR-AM on day 3 pi (F) and day 7 pi (G) by flow cytometry analysis after *in vivo* treatment with a caspase inhibitor. Graphs represent means \pm SEM of 9-12 mice, pooled from 4-6 experiments per time point.

Tnfsf14/Light and its receptors are upregulated in the murine lung upon IAV-induced pneumonia

Several members of the TNF superfamily (tnfsf) have been so far linked to cell death induction upon IAV infection [136, 146]; therefore, a tnfsf screening assay was used in order to identify a potential candidate which may be implicated in TR-AM depletion. To this end, HA-negative TR-AM were flow-sorted from the BALF of infected mice for gene expression assays regarding tnfsf ligands and their respective receptors. Data analysis revealed an upregulation of genes reflecting the activated, pro-inflammatory nature of TR-AM during the early infection phase, such as *Cd40*, *tnf*, and several other tnfsf ligands and receptors, including *tnfsf10*, which has been previously shown to play an important role in epithelial cell death [98]. Interestingly, there was no upregulation of *tnfrsf10b*, the receptor for *tnfsf10*, indicating that this death-initiating signalling pathway, though highly relevant for epithelial cells, was not involved in TR-AM death. Instead, another tnfsf ligand and receptor pair emerged as potential candidates. *Tnfrsf14* (or herpesvirus entry mediator, *hvem*) presented a remarkable upregulation both on day 3 pi (**Figure 18 A,C**) and on day 7 pi (**Figure 18 B,D**). The respective ligand, *tnfsf14* (or *light*) was additionally found to be upregulated in TR-AM, making these members of the tnfsf interesting candidates for further investigation regarding any involvement in TR-AM depletion following IAV infection.

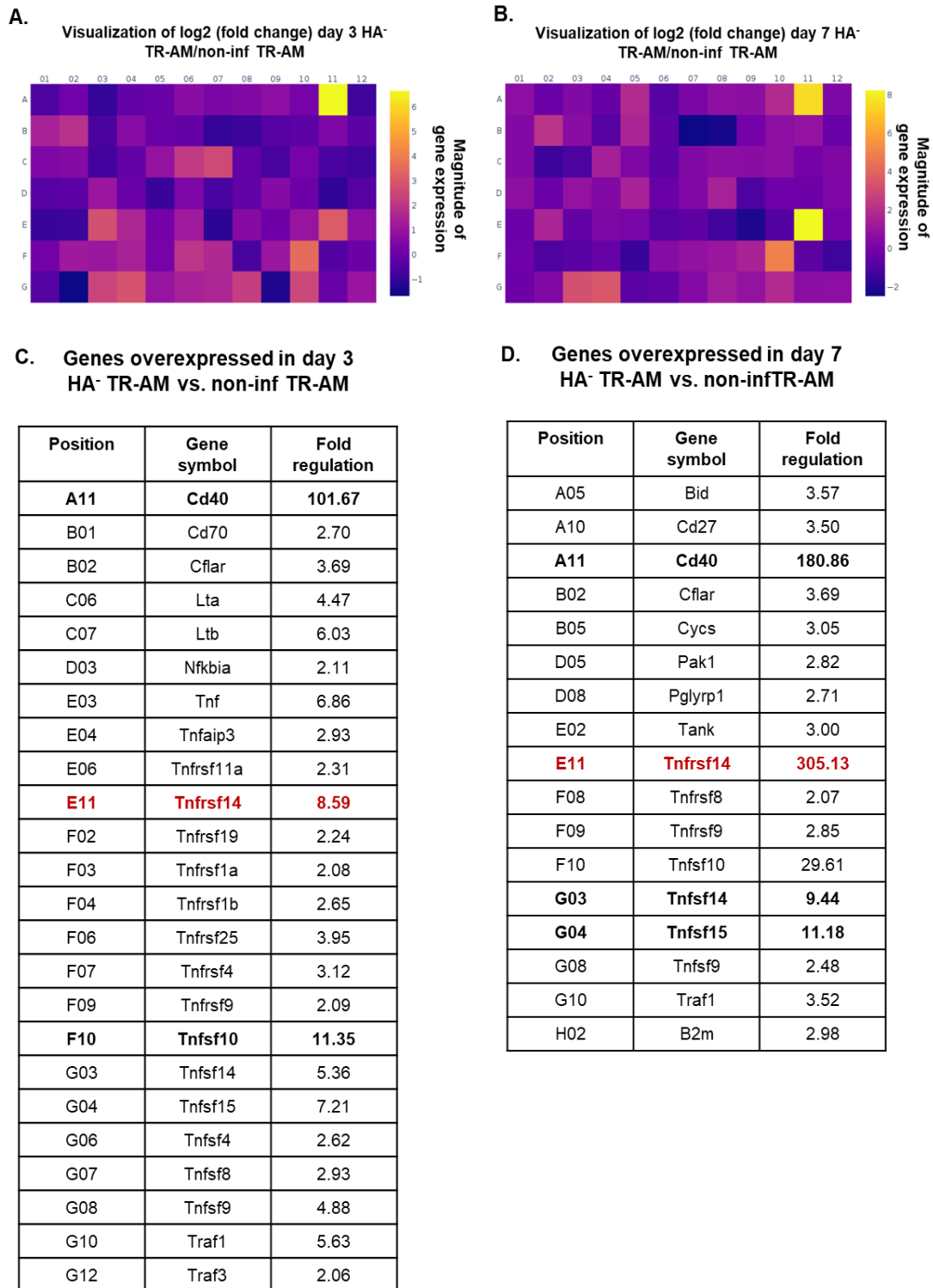


Figure 18. Gene expression analysis of flow-sorted TR-AM reveals an upregulation of various members of the *tnfsf* after IAV infection. (A-B) Heat maps depicting fold change in expression of *tnfsf*-related genes in flow-sorted, HA-negative (HA⁻) TR-AM on day 3 pi (A) and day 7 pi (B) compared to TR-AM from non-infected mice. (C-D)

Tables of heat map genes upregulated in flow-sorted (HA⁻) TR-AM on day 3 pi (C) and day 7 pi (D) over TR-AM from non-infected mice, including the respective position of the gene on the heat map, the gene name, and the fold change. Analysis was performed with the RT² Profiler TNF Signaling assay (Qiagen), n=4-6 mice per time point, data pooled from three different experiments.

As tnfrsf14 competes for ligation to tnfsf14/light with the lymphotoxin beta receptor (Itβr), we performed qPCR on flow-sorted TR-AM from the BALF of wild-type mice to establish an expression time course for both receptors. Over the course of infection, *ltβr* RNA levels remained relatively unchanged, yet an increase in protein expression on TR-AM surface was observed on day 7 pi (**Figure 19 A and B**). *Tnfrsf14/Hvem*, on the other hand, underwent significant upregulation during the early infection phase, which gradually subsided at later time points (**Figure 19 A**). Like Itβr, an increase in protein expression was observed on day 7 pi (**Figure 19 C**). Interestingly, treatment of naïve TR-AM with BALF from infected mice led to an upregulation of tnfrsf14/hvem levels 24h after treatment, while no significant changes could be observed for Itβr, mirroring the *in vivo* findings (**Figure 19 C**).

Once the receptor kinetics on TR-AM had been established, expression of the ligand in the murine lung was investigated both in homeostatic conditions and upon IAV infection. qPCR analysis revealed an upregulation in the lung of infected animals (**Figure 20 A**), while BALF ELISA demonstrated a significant increase in soluble tnfsf14/light, particularly during the acute infection phase (**Figure 20 B**). Tnfsf14/light signal was further shown to be much more prominent in the lung parenchyma of infected wild-type mice on day 7 pi compared to mock-infected animals, as shown by immunohistochemistry analysis (IHC) (**Figure 20 C**). Parallel to the murine data, soluble TNFSF14/LIGHT was highly expressed in the BALF of patients with severe IV pneumonia or COVID-19, compared to controls (**Figure 20 D**), thereby indicating a role for the ligand in virus-induced pneumonia.

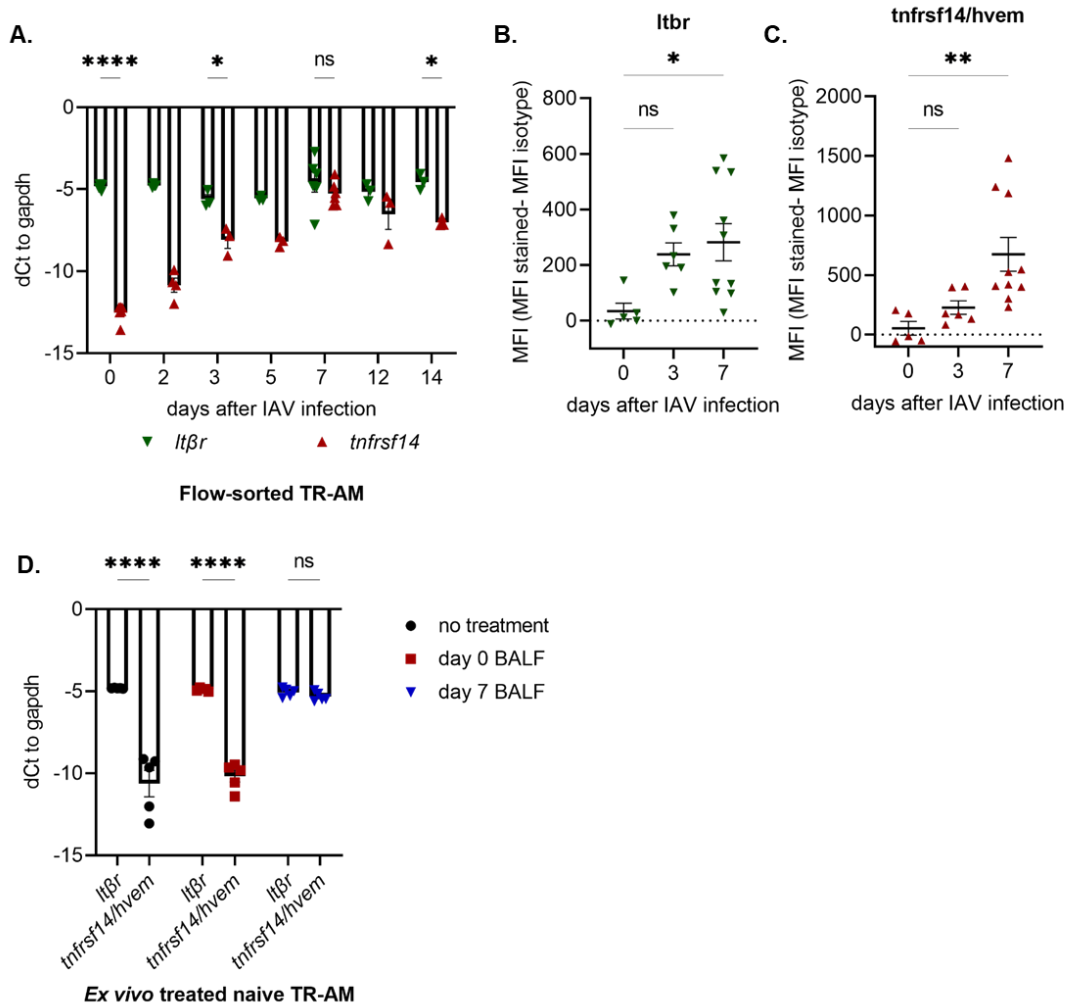


Figure 19. Tnfsf14/Light receptors on TR-AM follow distinct expression kinetics upon IAV-induced pneumonia.

(A) *Tnfsf14/hvem* and *Itβr* transcription comparison over the course of IAV-induced pneumonia by qPCR analysis. Data presented as dCt of gene expression over the housekeeping gene *gapdh*. Graph represents means \pm SEM of n=3-6 mice per time point. (B-C) Flow cytometry analysis for *Itβr* (B) and *tnfsf14/hvem* (C) expression on the surface of TR-AM on days 0, 3 and 7 after IAV infection. Median fluorescence intensity (MFI) normalized to an isotype control. Graphs represent means \pm SEM of n=5-10 mice per time point, data pooled from 4 different experiments. (D) qPCR analysis for *tnfsf14/hvem* and *Itβr* transcription regulation in TR-AM following 24h of treatment with 1:10 UV-inactivated BALF from mock-infected and infected mice from day 7 pi. Graph represents means \pm SEM of n=5 samples per condition, data pooled from three independent experiments.

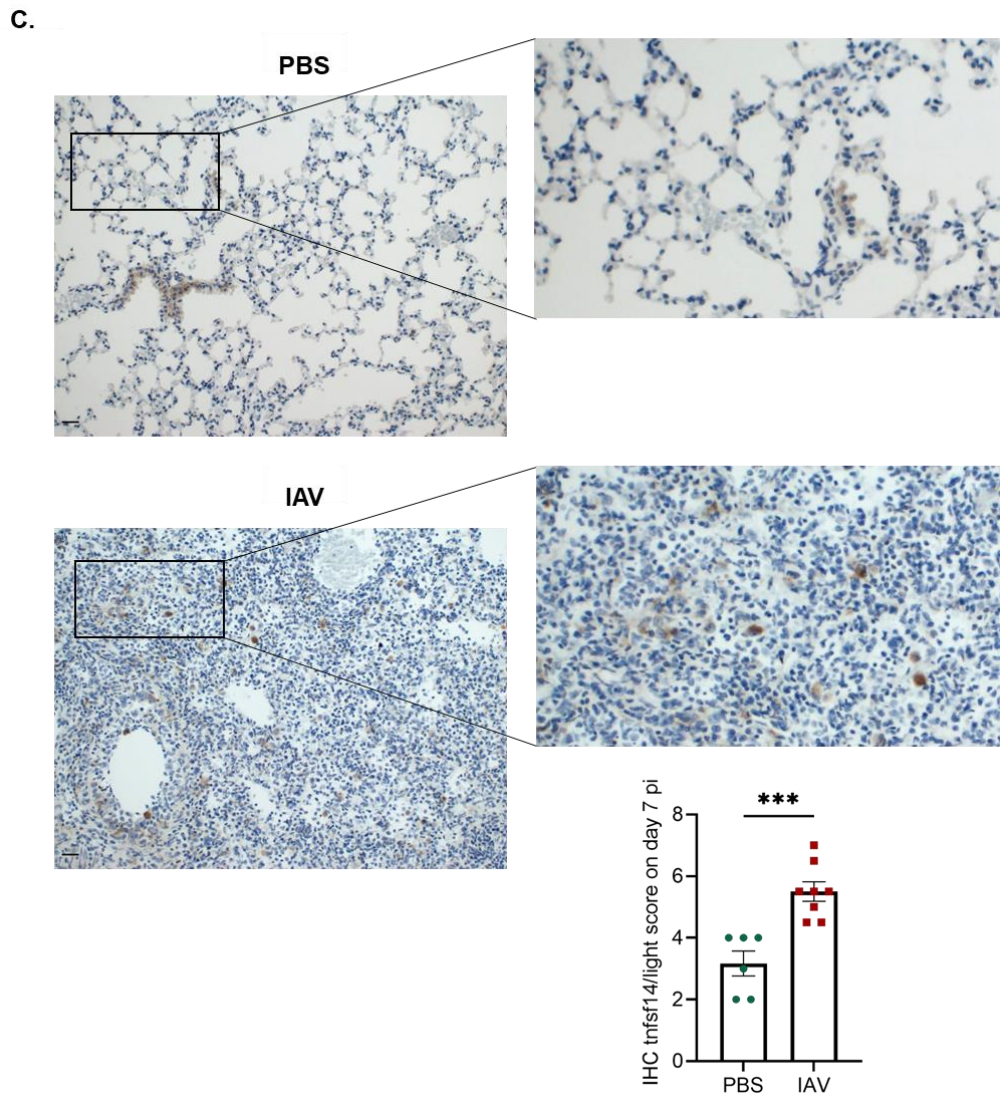
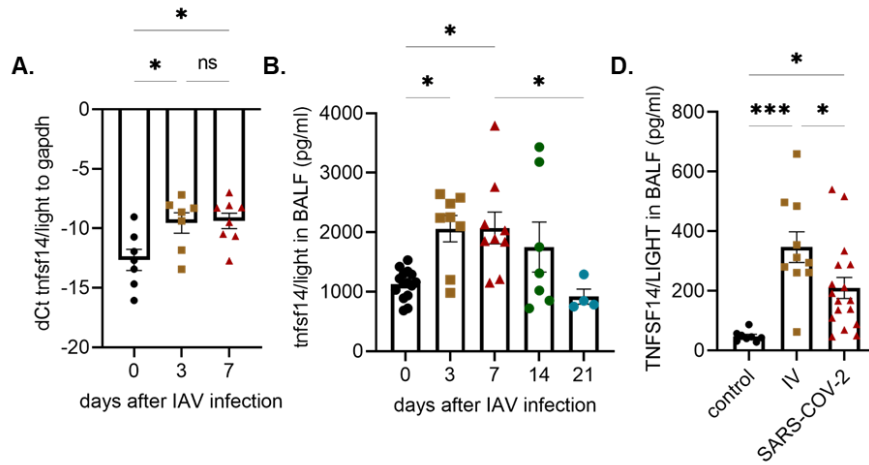


Figure 20. Pulmonary tnfsf14/light levels increase during the course of IAV-induced pneumonia. (A) qPCR for *tnfsf14* gene expression in the lungs of IAV-infected animals on days 0, 3, and 7 pi. Data presented as dCt of gene expression over the housekeeping gene *gapdh*. Graph represents means \pm SEM of n=7-8 animals per time point, data pooled from 7 independent experiments. (B) Soluble tnfsf14/light concentration in the BALF of infected wild-type mice measured by ELISA. Graph represents means \pm SEM of 3-8 mice per time point, data pooled from three independent experiments. (C) Left: IHC analysis for tnfsf14/light expression in representative sections after mock (upper panel) or IAV infection (lower panel). Scale bar set at 100 μ m. Right: Semi-quantitative score of total tnfsf14/light signal in murine lungs as defined per IHC analysis. Graph represents score means \pm SEM of 6-8 animals per condition. (D) Soluble TNFSF14/LIGHT quantification in the BALF of patients with IV pneumonia or COVID-19, compared to controls. Graph represents means \pm SEM of n= 8-17 patient samples per group.

Tnfsf14/Light drives TR-AM depletion upon IAV-induced pneumonia and TR-AM loss can be abrogated through genetic deletion or therapeutic targeting of the ligand

To address any role of *tnfsf14/light* in post-influenza TR-AM depletion, we treated flow-sorted murine TR-AM from non-infected mice and from days 3 and 7 pi with 500ng/ml rTnfsf14/Light for 24h *in vitro*. A statistically significant increase in caspase-3 activity could be observed in the day 3 pi group, compared to the PBS/BSA control of the same time point (**Figure 21 A**). No significant difference between treatments was shown in the non-infected group, while the lack of significance in the day 7 pi group could be potentially explained by the already high caspase-3 activity demonstrated by the PBS/BSA control on that time point of profound TR-AM apoptosis (see **Figure 15**). Treatment duration was also found to be of importance, as treatment of naïve TR-AM with rTnfsf14/Light for 72h led to a significant increase in caspase-3 and caspase-8 activity (**Figure 21 B-C**), suggesting a potential change in receptor regulation or initiation of different intracellular pathways through longer exposition to the ligand.

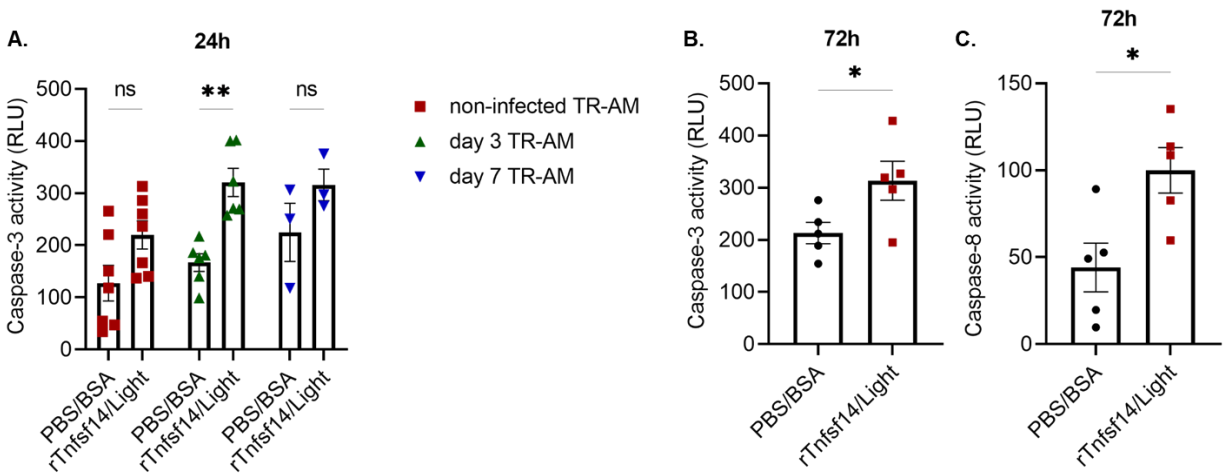


Figure 21. Treatment with rTnfsf14/Light drives TR-AM apoptosis upon IAV infection. (A) Caspase-3 activity assay following 24h treatment of flow-sorted naïve, day 3 pi, and day 7 pi TR-AM with 500ng/ml rTnfsf14/Light or PBS/BSA. Graph represents means \pm SEM of n=3-7 samples, data pooled from three different experiments. (B-C) Caspase-3 (B) and caspase-8 (C) activity following treatment of naïve TR-AM with 500ng/ml rTnfsf14/Light or PBS/BSA for 72h. Graphs represent means \pm SEM of n=4-7 samples, data pooled from three independent experiments.

Any potentially aggravating effect of *tnfsf14/light* treatment on TR-AM death was then evaluated *in vivo*. IAV-infected mice were orotracheally treated on days 1 and 2 pi with 10 μ g rTnfsf14/Light in 0.05ml PBS or PBS only. Flow cytometry analysis on day 3 pi revealed an increase in the

percentage of Annexin V⁺ BALF TR-AM following rTnfsf14/Light administration as well as an enhanced decrease in total TR-AM numbers in the BALF of rTnfsf14/Light-treated animals, compared to PBS-treated animals (**Figure 22** A-B). These results further corroborated the hypothesis that *tnfsf14/light* may play a role in post-IAV TR-AM death, which was then investigated in another series of *in vivo* approaches.

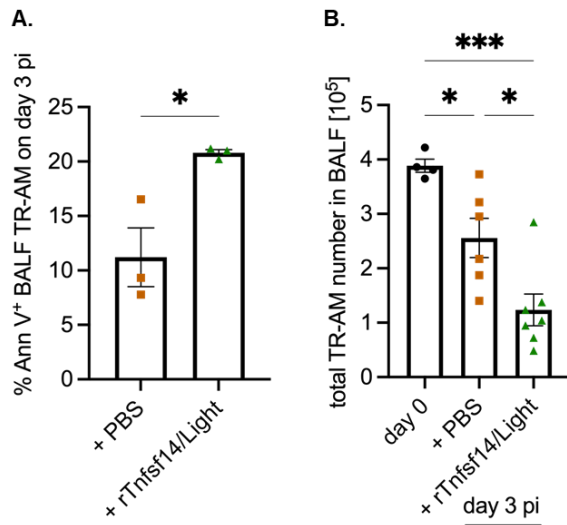


Figure 22. Ororhacheal administration of rTnfsf14/Light aggravates TR-AM loss on day 3 pi. (A)

Percentage of Annexin V⁺ TR-AM in the BALF of infected mice upon administration of rTnfsf14/Light or a PBS control. Graph represents means \pm SEM of n=3 animals per condition. (B) Quantification of TR-AM numbers in the BALF of non-infected and IAV-infected mice on day 3 pi shows a significant decline in absolute numbers upon rTnfsf14/Light administration in comparison with PBS-treated mice. Graph represents means \pm SEM of n=4-7 animals per time point and condition.

Tnfsf14^{-/-} mice presented an intact BALF TR-AM pool over the course of infection, as opposed to wild-type mice, when infected with 500ffu IAV (**Figure 23** A). In line with that, treatment of naïve wild-type TR-AM with virus-free, UV-inactivated BALF from *tnfsf14*^{-/-} mice did not have any significant effect on caspase-3 activity, as opposed to treatment with wild-type BALF (**Figure 23** B).

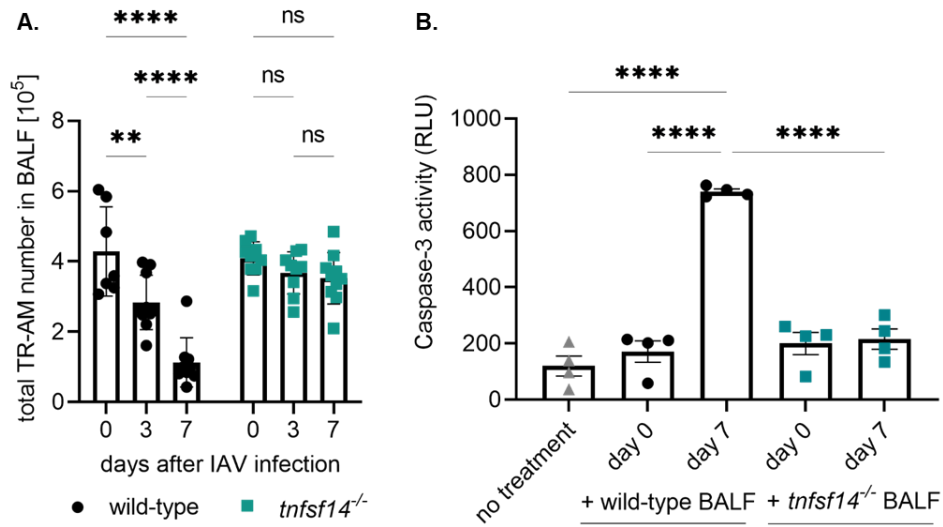
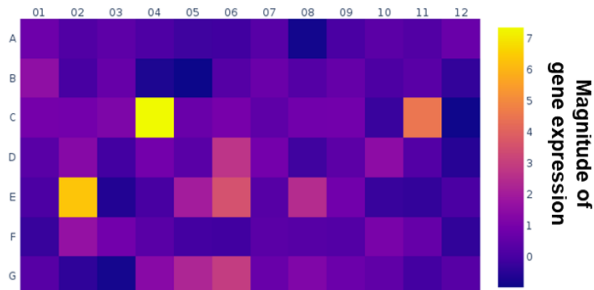


Figure 23. Loss of *tnfsf14*/light preserves the TR-AM pool over the course of IAV infection. (A) Quantification of TR-AM in the BALF of wild-type and *tnfsf14*^{-/-} mice on day 0, day 3, and day 7 pi, following infection with 500ffu IAV. Graph represents means \pm SEM of n=3-10 animals per group and time point. (B) Caspase-3 activity 24h post-treatment of naïve wild-type TR-AM with virus-free, UV-inactivated BALF from wild-type and *tnfsf14*^{-/-} mice. Graph represents means \pm SEM of n=4 animals per condition.

Gene expression analysis of flow-sorted *tnfsf14*^{-/-} TR-AM additionally revealed an attenuated upregulation of death-related genes on day 3 pi and on day 7 pi over TR-AM from non-treated mice over the course of infection, compared to wild-type mice (**Figure 24 A-H**).

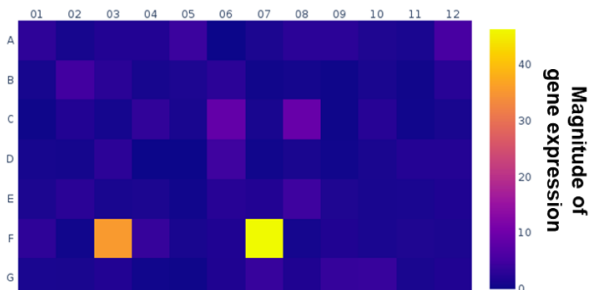
A.

Visualization of log₂ (fold change) day 3/non-inf HA-TR-AM (wild-type)



B.

Visualization of log₂ (fold change) day 3/non-inf HA-TR-AM (*tnfsf14*^{-/-})



C. Genes overexpressed in day 3 HA- vs. non-infected wild-type TR-AM

Position	Gene symbol	Fold regulation
B01	Bcl2	2.88
C03	Ccdc103	2.20
C04	Cd40	163.41
C11	Dpysl4	2.49
D06	Fasl	6.70
D10	Galnt5	2.78
E02	Ifng	79.88
E05	Ins2	4.05
E06	Irgm1	11.59
E08	Kcnp1	5.60
F02	Nol3	3.08
F10	S100a7a	2.07
G04	Tnf	2.58
G05	Tnfrsf10b	4.87
G06	Tnfrsf11b	7.67

D. Genes overexpressed in day 3 HA- vs. non-infected *tnfsf14*^{-/-} TR-AM

Position	Gene symbol	Fold regulation
C04	Cd40	9.56
E02	Ifng	6.03
E06	Irgm1	5.13
F10	S100a7a	2.47
F11	Snca	2.88
G06	Tnfrsf11b	3.04
H02	B2m	2.79

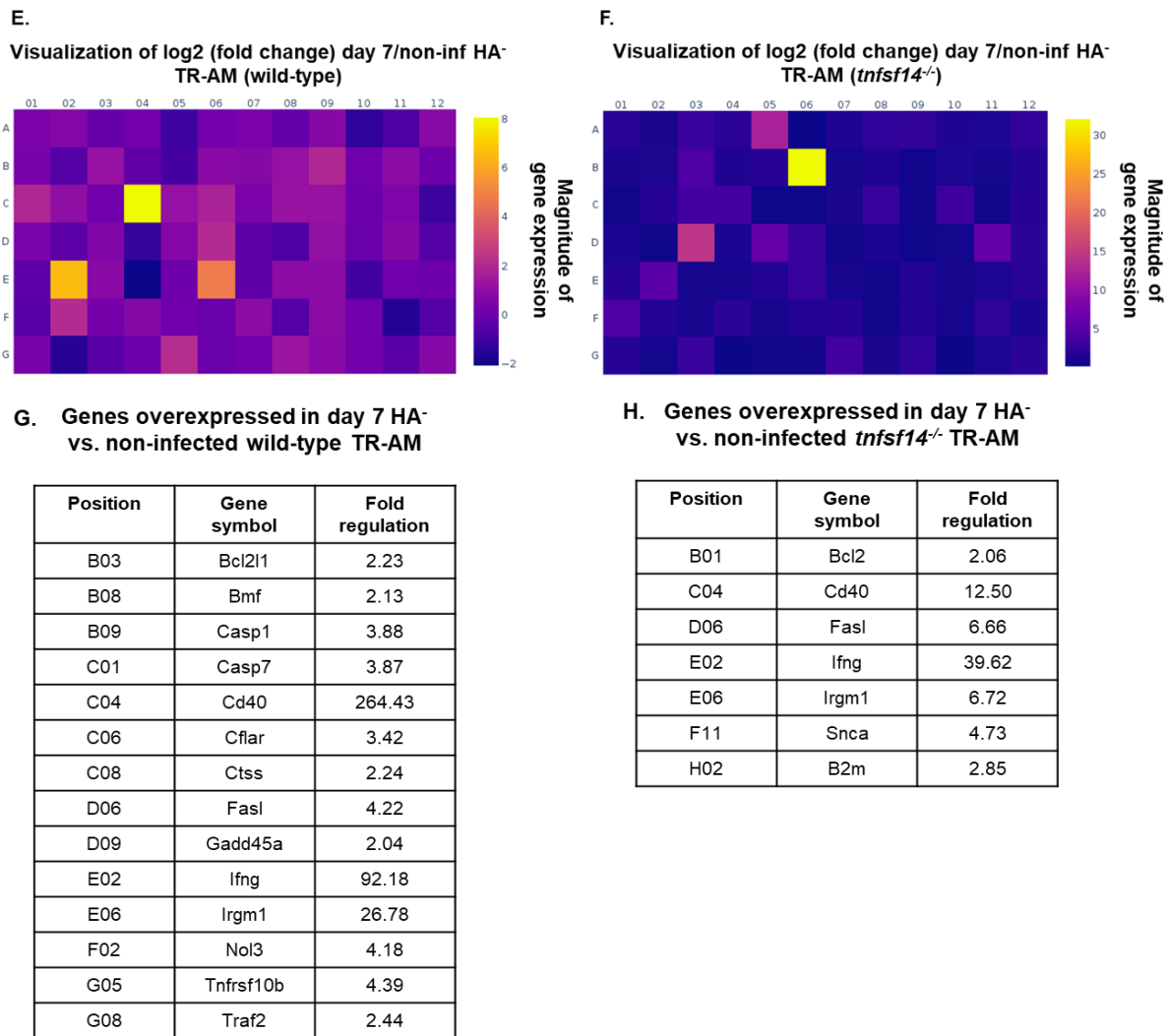
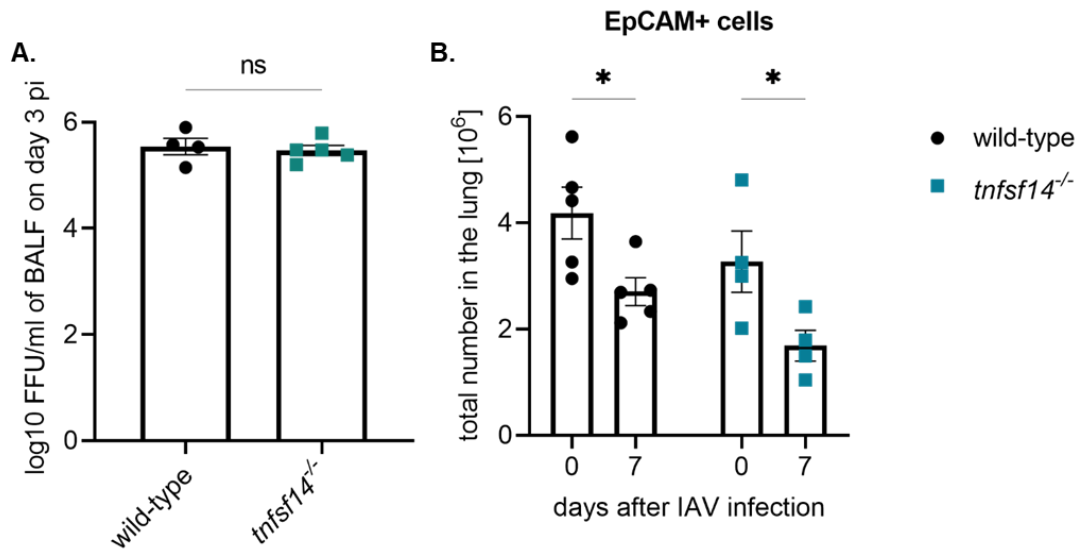


Figure 24. Gene expression analysis of flow-sorted wild-type and *tnfsf14*^{-/-} TR-AM over the course of IAV infection. Heat maps depicting fold change in the expression of cell death-related genes in flow-sorted, HA-negative (HA⁻) TR-AM on day 3 pi and day 7 pi in comparison to TR-AM from non-infected mice, using the RT² Cell Death PathwayFinder® assay. Tables present position in the heat map, name of the upregulated genes, and the respective fold change, data summarized as follows: wild-type, day 3 pi over non-infected: heat map A, table C; wild-type, day 7 pi over non-infected: heat map E, table G; *tnfsf14*^{-/-}, day 3 pi over non-infected: heat map B, table D; *tnfsf14*^{-/-} day 7 pi over non-infected: heat map F, table H. Data from 3-5 mice per group and time point, data pooled from three independent experiments.

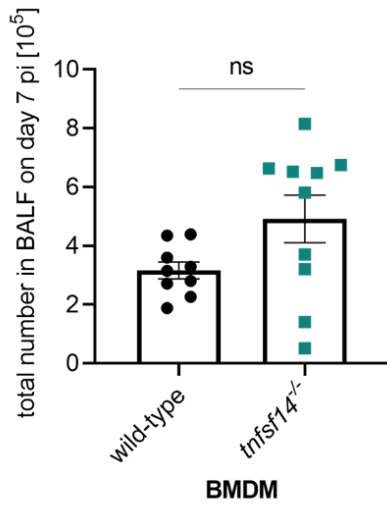
To exclude any antiviral effect of *tnfsf14*/light deletion leading to milder infection and therefore attenuated lung injury and TR-AM loss, viral titers on the day of viral peak (day 3 pi) [98] (**Figure 25 A**) and numbers of epithelial cells (defined as EpCAM⁺ as per flow cytometry analysis) (**Figure**

25 B) over the course of IAV infection were compared between wild-type and *tnfsf14*^{-/-} mice, revealing no differences between the two groups. Next, the inflammatory response, including immune cell influx and cytokine release, as well as the histological alterations in wild-type and *tnfsf14*^{-/-} mice were analyzed. As TR-AM numbers reach their lowest levels on day 7 pi in wild-type conditions (**Figure 12**), further analyses focused on this time point. *Tnfsf14*^{-/-} mice showed an enhanced neutrophil influx (**Figure 25 D, I**), higher dendritic cell numbers (**Figure 25 L, M, O**) and lower T cell numbers (**Figure 25 G, Q**) in their BALF and lungs than their wild-type counterparts, which could be mirroring the central role of *tnfsf14*/light in the crosstalk between innate and adaptive immunity. Interestingly, IM numbers were lower in *tnfsf14*^{-/-} mice than wild-type mice (**Figure 25 N**). When compared to day 0, *tnfsf14*^{-/-} mice presented a significant decline on day 7 pi, while wild-type IM numbers showed a drastic increase, when compared to baseline (**Figure 25 R**). No further differences could be detected between wild-type and *tnfsf14*^{-/-} mice in inflammatory cell influx (**Figure 25**) or BALF cytokine profile (**Figure 26**).

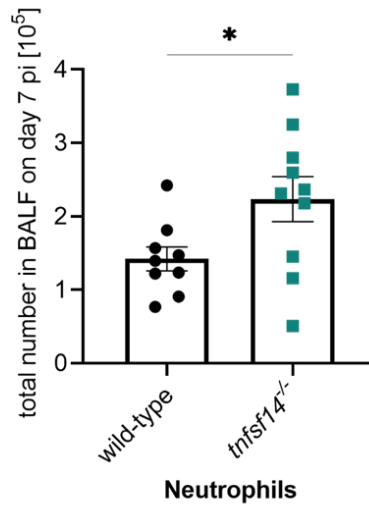


BALF

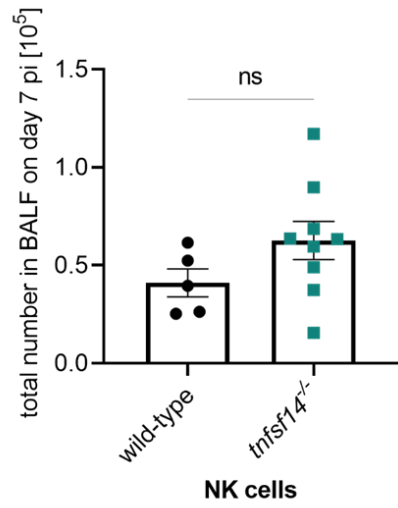
C.



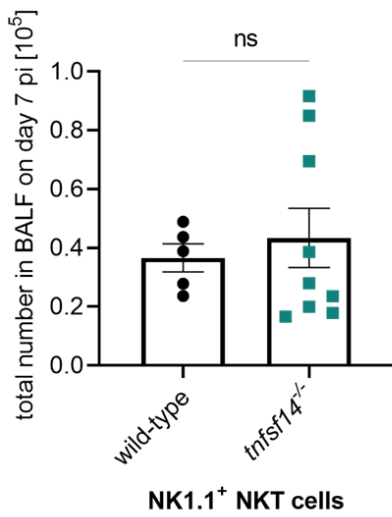
D.



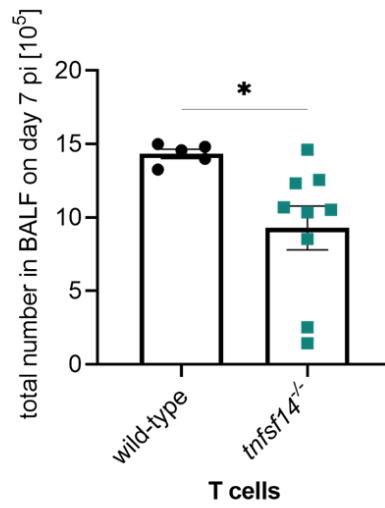
E.



F.

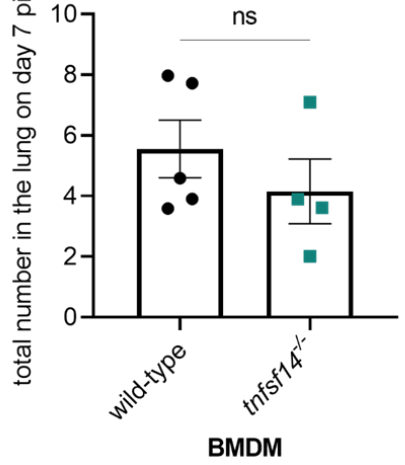


G.

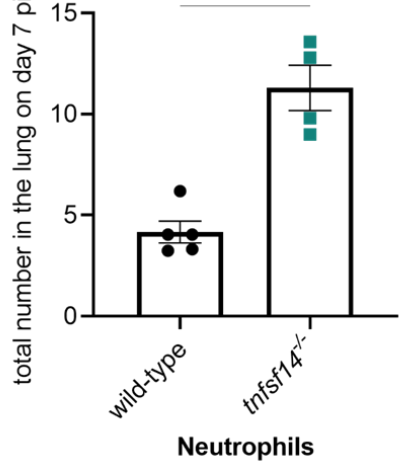


Lung

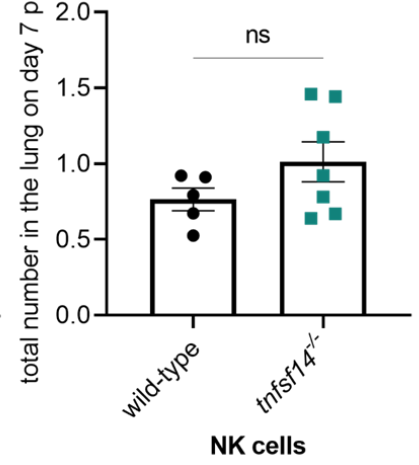
H.



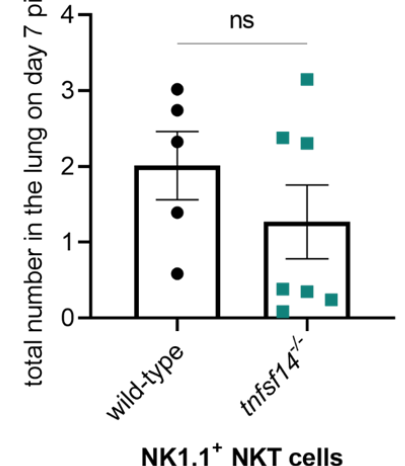
I.



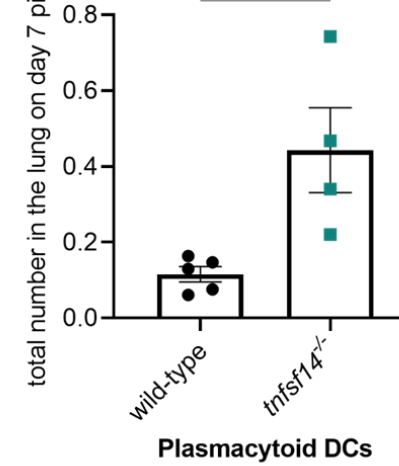
J.



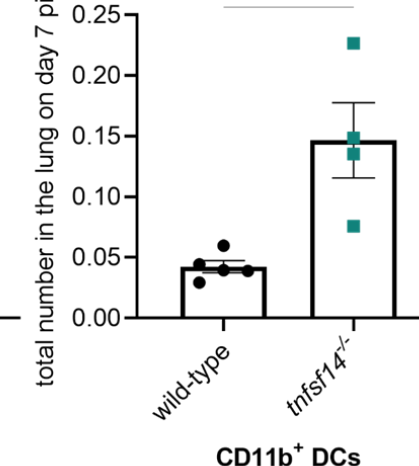
K.



L.



M.



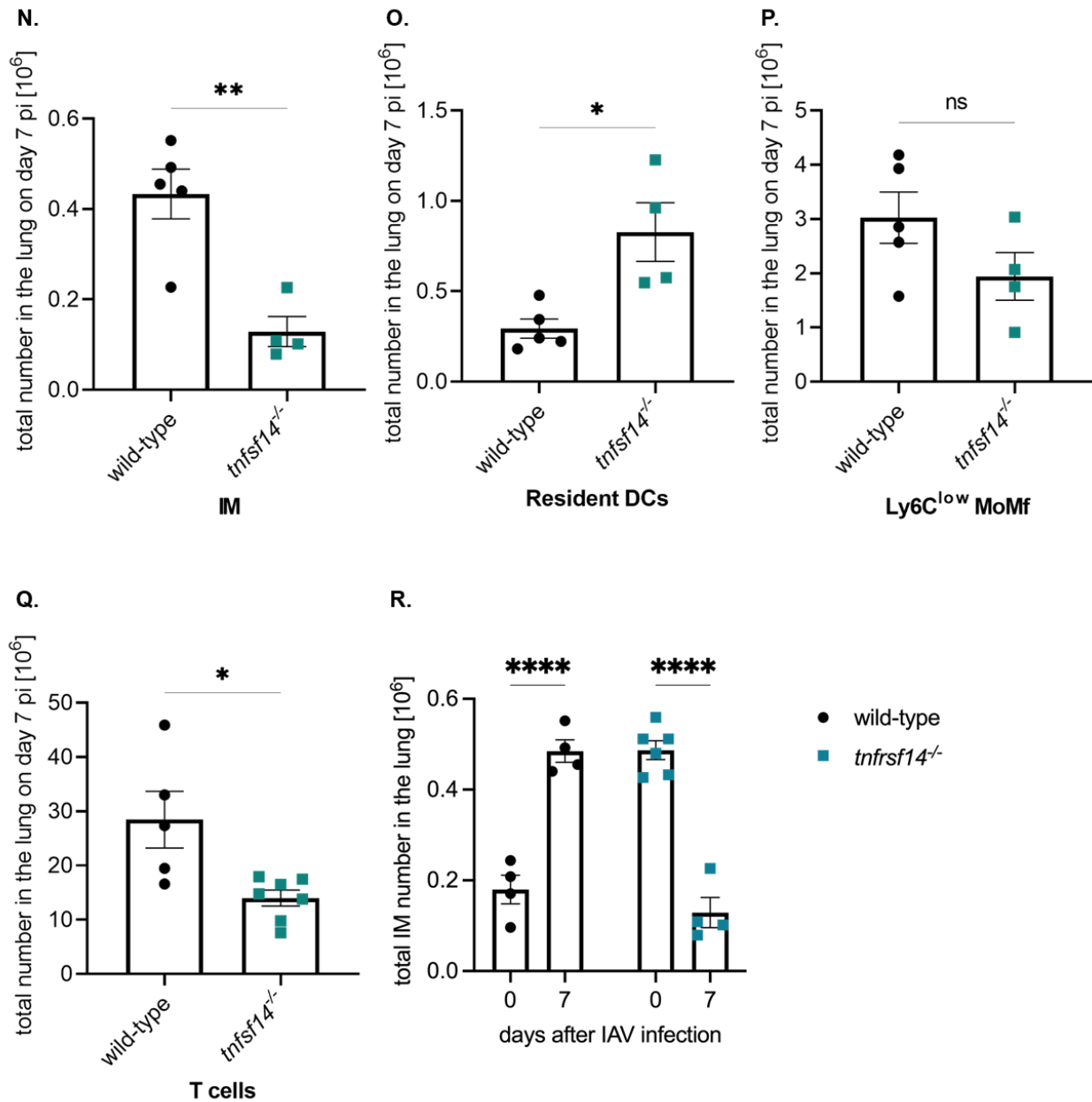


Figure 25. Characterization of the injury degree and the inflammatory response of wild-type and *tnfrsf14*^{-/-} mice following IAV infection. (A) Viral titers in the BALF of wild-type and *tnfrsf14*^{-/-} mice on day 3 pi. Graph represents means \pm SEM of n=4 animals per group. (B) Quantification of EpCAM⁺ cells in the lungs of wild-type and *tnfrsf14*^{-/-} mice on day 0 and day 7 pi. Graph represents means \pm SEM of n=4-5 animals per group. (C-Q) Quantification of different immune cell populations in the BALF (C-G) and the lungs (H-P) of wild-type and *tnfrsf14*^{-/-} mice, including BMDM, neutrophils, NK and NKT cells, T cells, IM, and diverse DCs subsets on day 7 pi after infection with 500ffu IAV. Graphs represent means \pm SEM of n=4-10 animals per group. (R) Quantification of IM in the lungs of wild-type mice on day 0 and day 7 pi. Graph represents means \pm SEM of n=4-7 animals per time point.

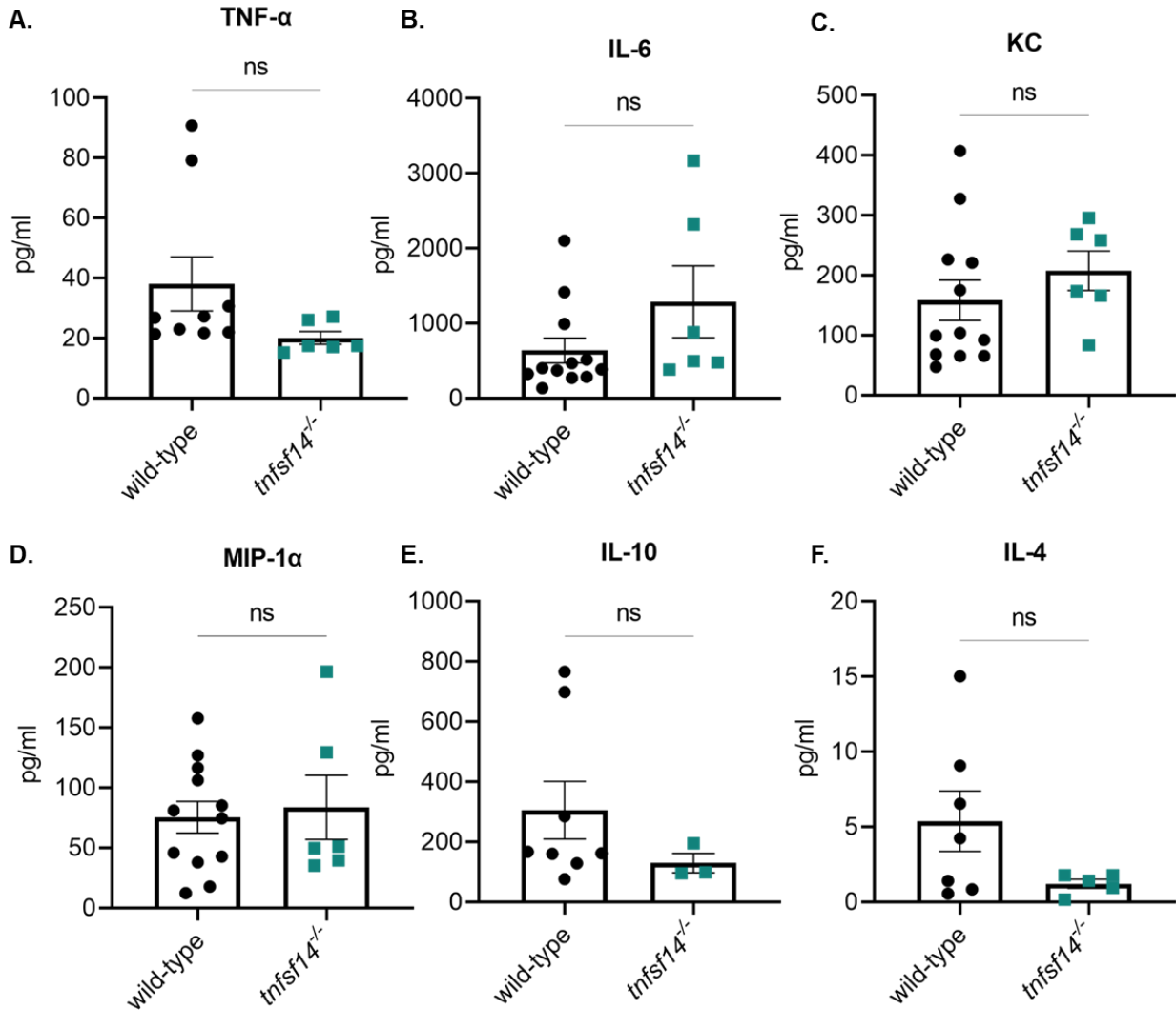


Figure 26. Cytokine profile as measured in the BALF of wild-type and *tnfsf14*^{-/-} mice on day 7 pi per multiplex analysis. (A-F) Graphs represent means \pm SEM of n=3-12 animals. TNF- α : tumor necrosis factor alpha, IL: interleukin, KC: chemokine (C-X-C motif) ligand 1, MIP: macrophage inflammatory protein.

Additionally, an attenuated weight loss over the course of infection (**Figure 27 A**) and a reduced histological score on day 7 pi (**Figure 27 B and C**) were observed in *tnfsf14*^{-/-} mice, compared to their wild-type counterparts. Histological alterations were characterized and quantified as described in the 'Methods' section. Briefly, lungs were evaluated for the presence of hemorrhage, alveolar and perivascular edema, perivascular infiltrates, pleuritis, steatitis, bronchitis, tracheitis, and bronchus-associated lymphoid tissue (BALT) formation. A pneumonia grading system from 0-4 was developed for each parameter and total score was calculated as the sum of the individual

values. Despite the similarities between wild-type and *tnfsf14*^{-/-} mice regarding viral titers, epithelial damage, and inflammatory response, the attenuated weight loss and superior histological pneumonia score could reflect additional roles of the pro-inflammatory *tnfsf14*/light in the lung, e.g. in endothelial injury [194, 195].

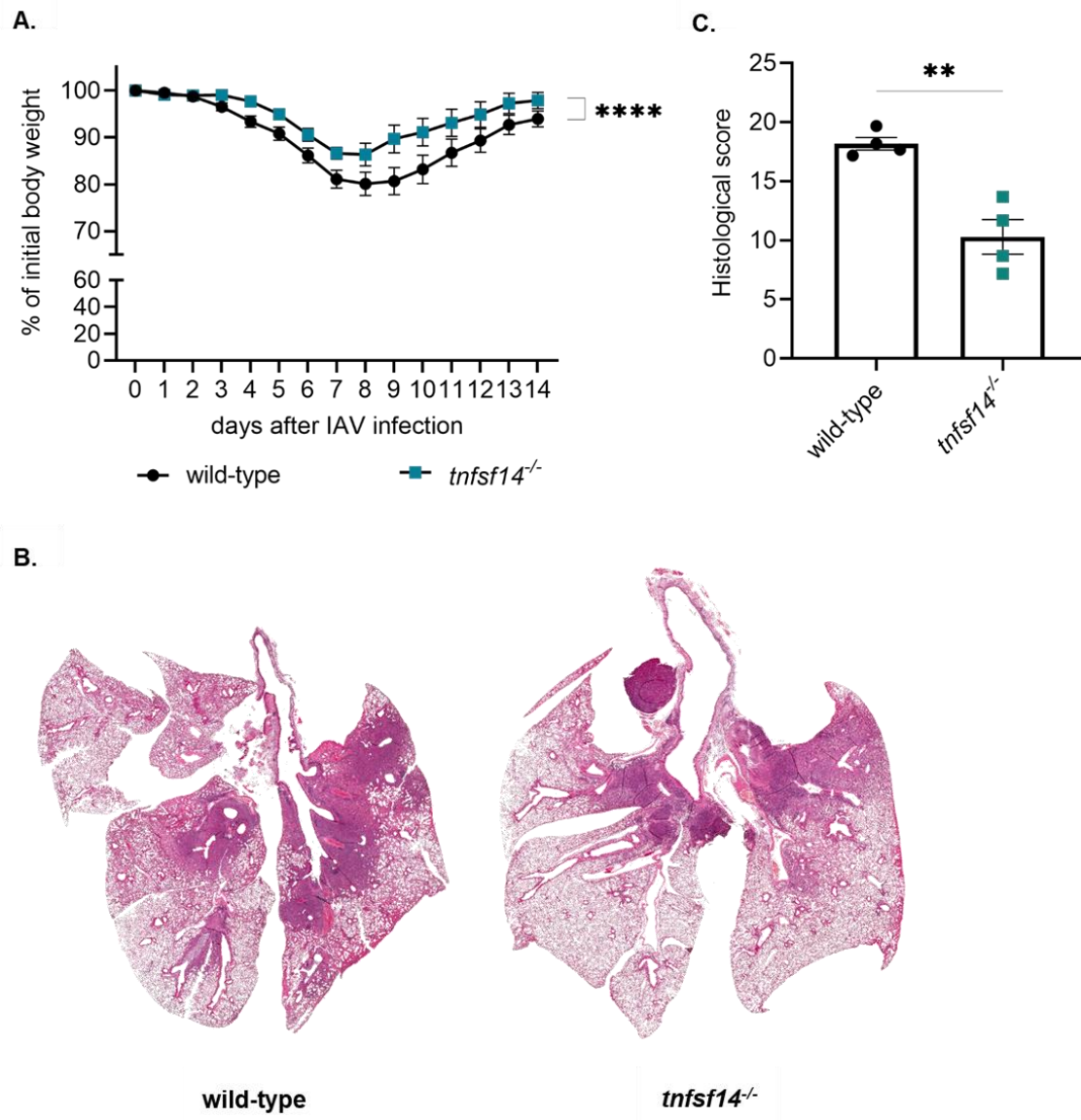


Figure 27. Post-influenza clinical score is improved in *tnfsf14*^{-/-} mice compared to wild-type mice. (A) Body weight over the course of IAV infection presented as percentage to initial weight up to day 14 pi for wild-type and *tnfsf14*^{-/-} mice. Graph represents means ± SEM of weight at each time point, n=12-13 animals per group. (B) Representative whole-lung histological sections of wild-type (l) and *tnfsf14*^{-/-} mice (r) on day 7 pi, following infection with 500ffu IAV. (C) Histological score normalized to the respective mock-infected controls; graph represents means ± SEM of n=4 animals per group.

Similar results to the genetic deletion were observed when a specific neutralizing mouse anti-mouse antibody was used to block *tnfsf14/light* *in vivo*. TR-AM loss could be attenuated on day 7 pi (**Figure 28 A**) with no differences in immune cell influx in the BALF (**Figure 28 B**) and the lung (**Figure 28 C, D**). Additionally, an attenuated caspase-3 activation could be observed upon treatment of naïve TR-AM with BALF from infected wild-type mice when the neutralizing anti-*tnfsf14/light* antibody was used (**Figure 28 E**). Even though no return to baseline was observed, as was the case with *tnfsf14*^{-/-} BALF, there was a clear advantage over the isotype control regarding *in vivo* TR-AM numbers and *in vitro* caspase-3 activity, offering a potential therapeutic approach for attenuating IAV-induced TR-AM death.

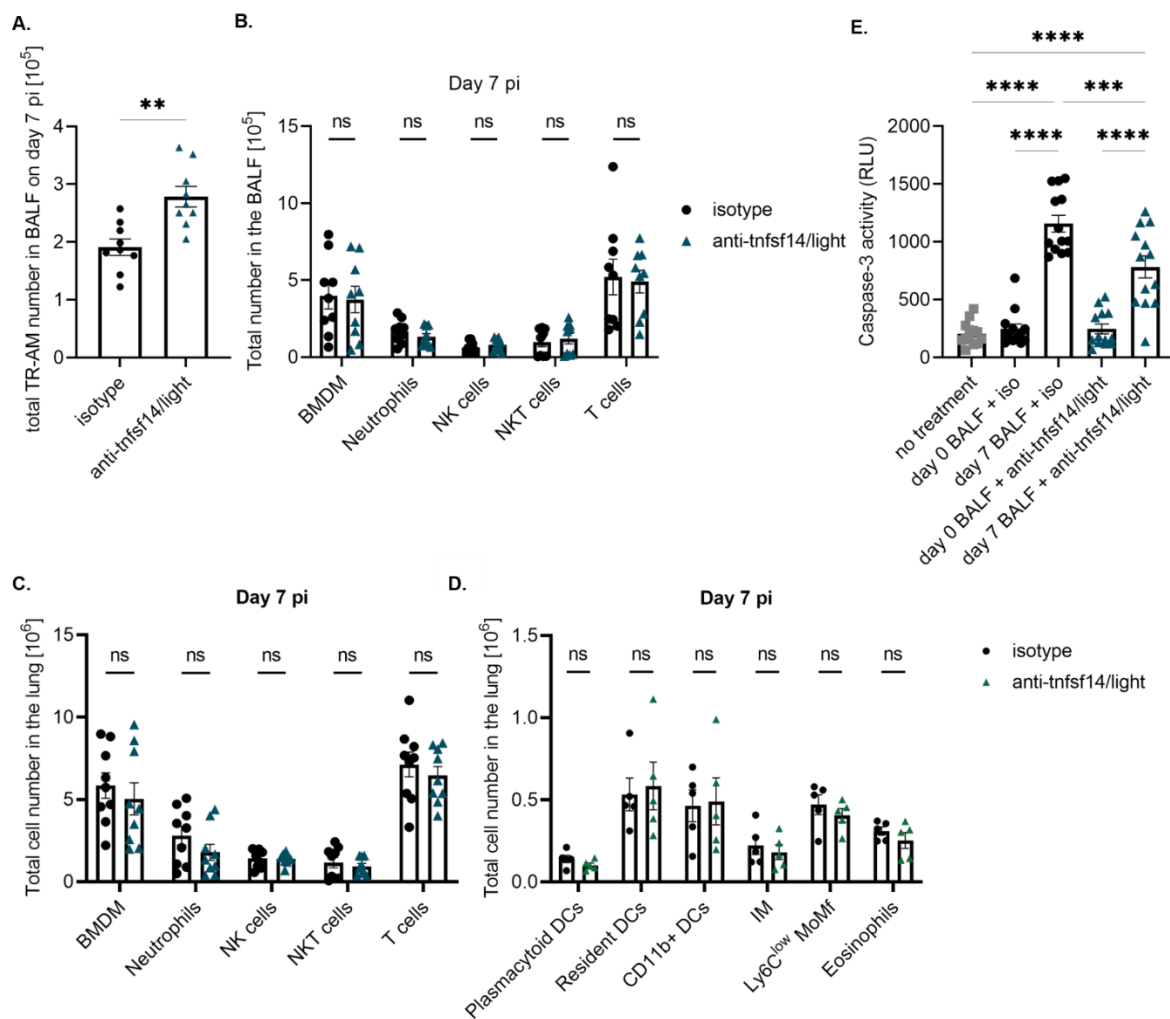


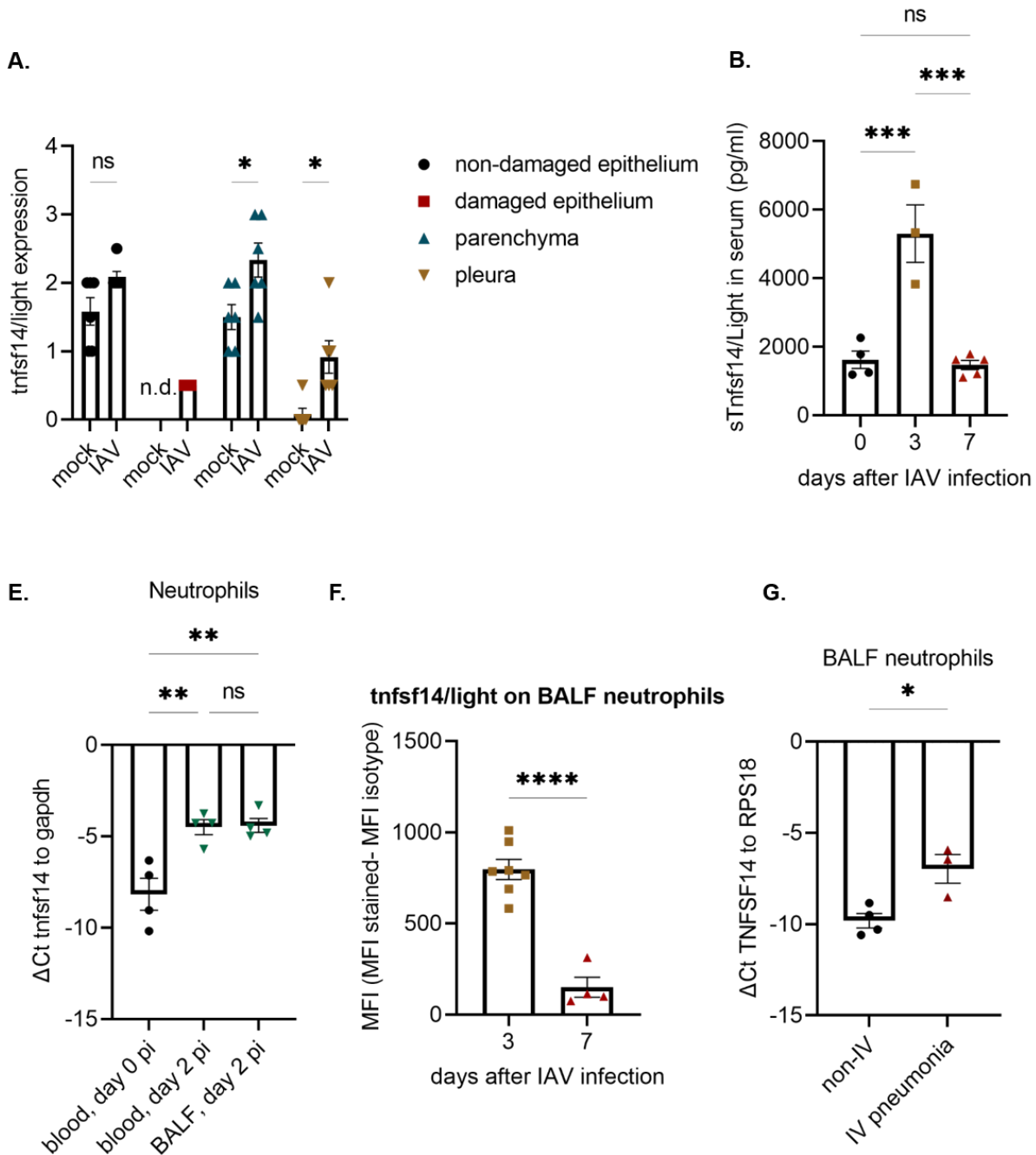
Figure 28. Therapeutic blocking of *tnfsf14/light* attenuates TR-AM loss upon IAV infection. (A) Quantification of TR-AM in the BALF of IAV-infected mice intraperitoneally treated with 500 μ g/0.2ml of a blocking anti-*tnfsf14/light* antibody or an isotype control on day 2 pi, analysis performed on day 7 pi. Graph represents means \pm SEM of n=9 animals per group. (B-D) Immune cell influx in the BALF (B) and in the lungs (C-D) of infected mice

upon the same experimental setup. (D) Caspase-3 activity 24h after treatment of naïve TR-AM with virus-free, UV-inactivated BALF from infected animals following 1h pre-incubation of the BALF with 1µg/ml anti-tnfsf14/light antibody at 4°C. Graph represents means ± SEM of n=3 independent experiments.

Neutrophils are the main cellular source of tnfsf14/light upon IAV infection and neutrophil depletion attenuates TR-AM loss

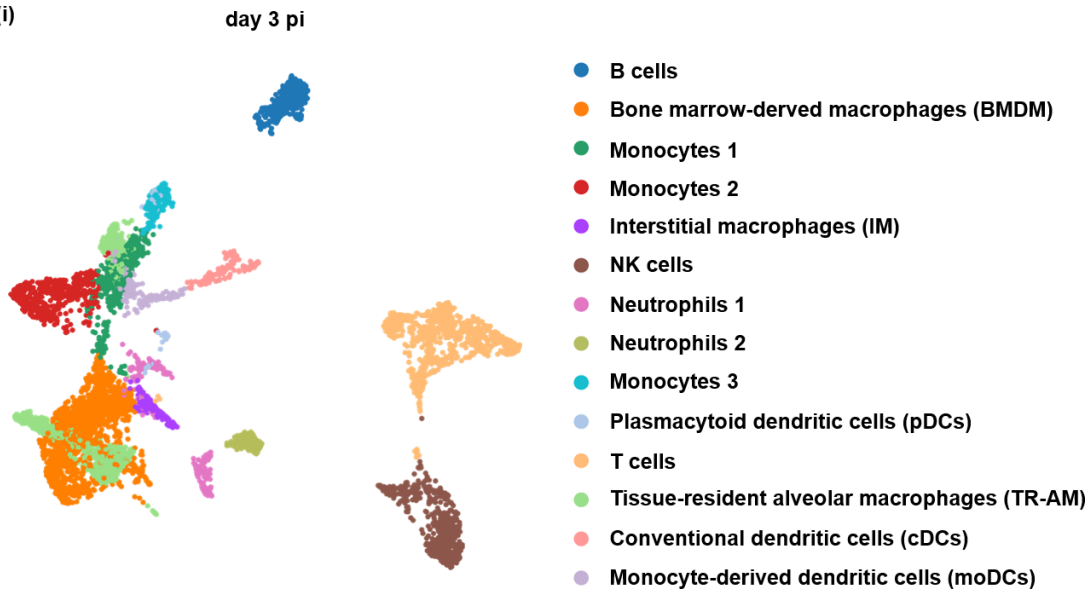
Tnfsf14/light expression has a wide distribution in the lung, involving leukocytes and non-leukocyte populations [176, 177]. Indeed, immunohistochemistry analysis in the lungs of mock- and IAV-infected mice on day 7 pi revealed a widespread expression in various compartments of the lung (**Figure 29 A**), which were, however, differently affected by infection; an increase in expression could be observed in the parenchyma and in the pleuritic region, hinting at a potential link to leukocyte influx. Conversely, expression was barely changed within intact epithelium, whereas injured epithelium showed a remarkably low expression compared to the intact regions. This change in expression pattern implied that within damaged areas of interest, tnfsf14/light was not of epithelial, but rather of leukocyte origin. Furthermore, tnfsf14/light ELISA in the serum of infected mice revealed a transient but significant increase in the soluble ligand on day 3 pi and decreasing levels on day 7 pi, which could be reflecting ligand expression by leukocytes in the periphery (**Figure 29 B**). To identify the main leukocyte population which serves as a cellular source for tnfsf14/light, single-cell RNA sequencing analysis was performed in flow-sorted leukocytes from the lungs of non-lavaged animals on day 3 pi (**Figure 29 C i-iii**) and day 7 pi (**Figure 29 D i-iii**). On both time points, neutrophils were revealed to be the population with the highest fraction of tnfsf14/light-expressing cells and RNA expression levels for *tnfsf14*, with minimal contribution from macrophages and T cells. Interestingly, *l1βr* was highly expressed by all monocyte/macrophage populations, while only low levels of *tnfsf14* could be detected in them (**Figure 29 C, D**). qPCR analysis of neutrophils from the peripheral blood on day 0 and day 2 pi (one day prior to the first time point of significantly decreased TR-AM numbers in the BALF, **Figure 12**) showed a massive upregulation in *tnfsf14* expression, while no difference could be detected between blood-derived and BALF neutrophils on day 2 pi, suggesting not only expression of the ligand by neutrophils in terms of systemic inflammation, but also *in situ* presence of the ligand in the lung (**Figure 29 E**). At the same time, flow cytometry analysis revealed high expression levels of the transmembrane form of tnfsf14/light on neutrophils on day 3 pi, with a significant decrease on day 7 pi, following ligand release (**Figure 29 F**). In accordance with our

murine data, flow-sorted neutrophils from a small group of patients with severe IV pneumonia revealed an upregulation in *tnfsf14/light* gene expression, compared to non-influenza controls (**Figure 29 G**).

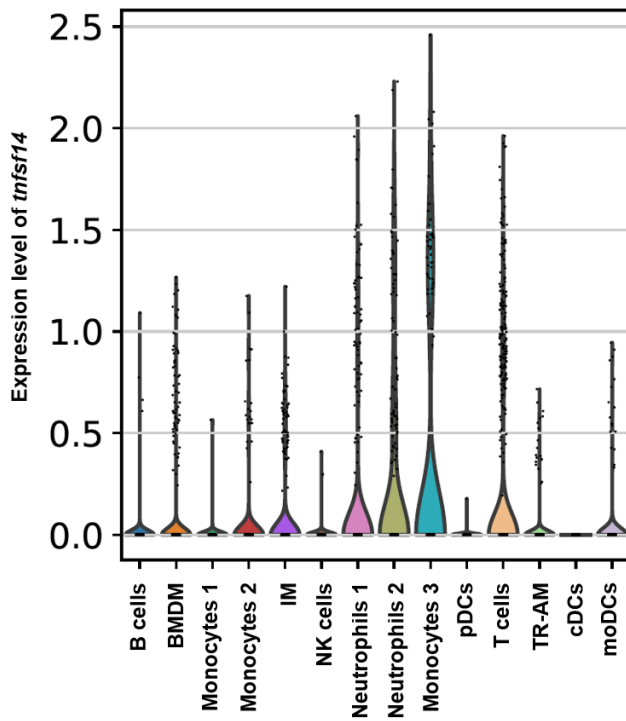


C.

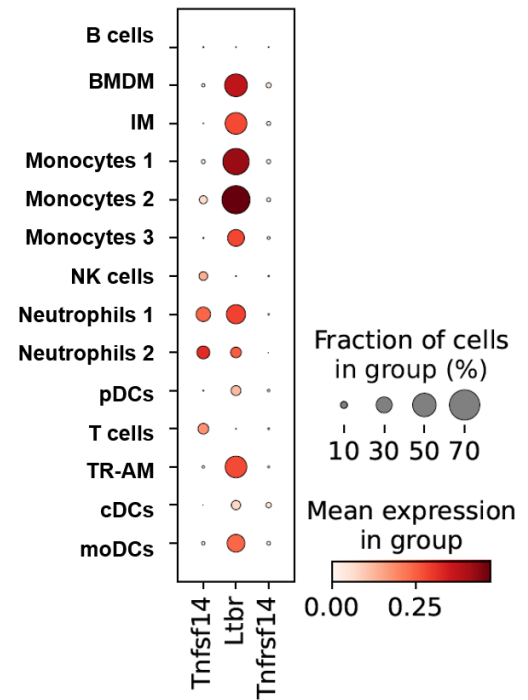
(i)



(ii)

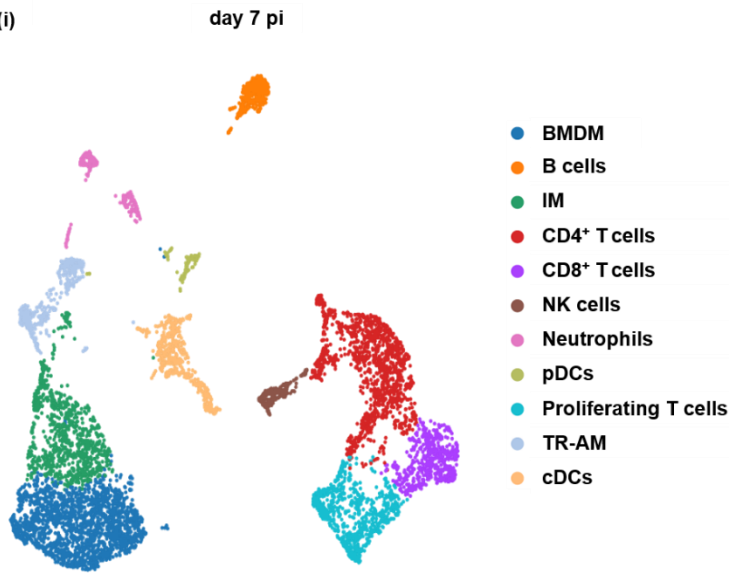


(iii)

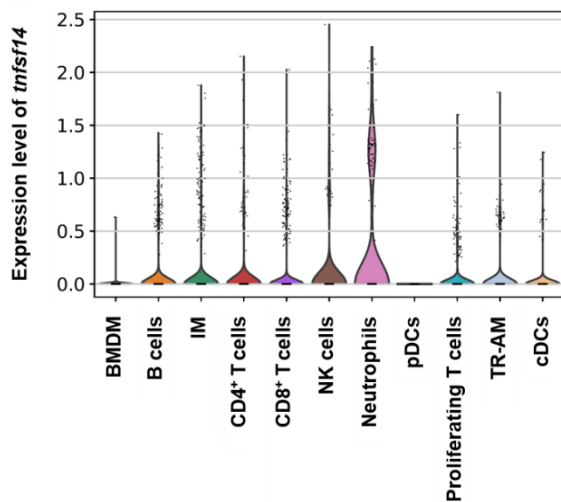


D.

(i)



(ii)



(iii)

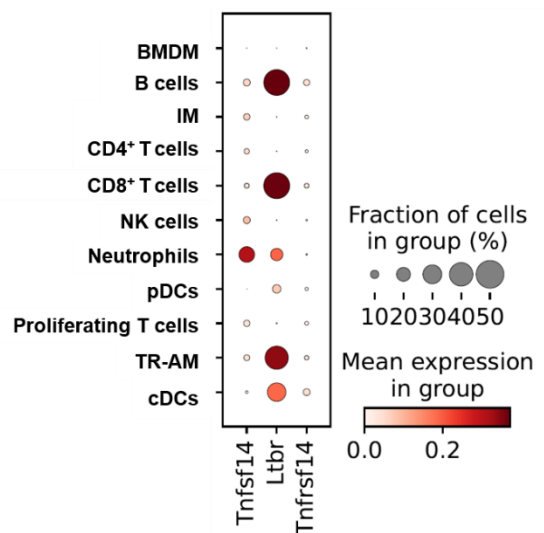


Figure 29. Neutrophils are the main cellular source of *tnfsf14*/light upon IAV infection. (A) *Tnfsf14*/light signal distribution in different histological areas of lung sections on day 7 pi following IAV infection, as shown by immunohistochemistry analysis. Graph represents means \pm SEM of $n=6$ animals. (B) ELISA for soluble *tnfsf14*/light in the serum of IAV-infected animals over the course of infection. Graph represents means \pm SEM of $n=3-5$ animals. (C-D) Single-cell RNA sequencing analysis on leukocytes sorted from the lungs of infected animals on day 3 pi and day 7 pi. Leukocytes were defined as live $CD45^+$ cells, 500,000 cells were sorted per time point. Analysis performed in 10,000 cells/sample, 4 samples per time point. On day 3 pi, 14 leukocyte clusters were identified (C i) and 11 clusters were identified on day 7 pi (D i). Violin plots depict *tnfsf14* expression levels among the different clusters (C ii, D ii),

dot plots demonstrate fractions of cells within each cluster (%) expressing *tnfsf14*, *tnfrsf14*, and *ltbr* (C iii, D iii), as well as expression levels within each cell group. (E) qPCR for *tnfsf14* regulation on murine neutrophils isolated from the blood on day 0 and from the blood and BALF of infected mice on day 2 pi. Data presented as dCt to the housekeeping gene *gapdh*. Graph represents means \pm SEM of n=4 mice per sample. (F) Tnfsf14/Light expression on the surface of BALF neutrophils on day 3 and day 7 pi, depicted as MFI normalized to an isotype control. Graph represents means \pm SEM of n=4-6 mice per time point. (G) qPCR for *TNFSF14* in neutrophils isolated from the BALF of patients with severe IV pneumonia compared to non-IV controls. Data presented as dCt to the housekeeping gene *RPS18*. Graph represents means \pm SEM of n=3-4 samples.

Based on these data, post-influenza TR-AM survival was evaluated after neutrophil depletion. To this end, IAV-infected mice were intraperitoneally treated with 200 μ g of a neutrophil-depleting antibody (anti-Ly6G, clone 1A8) or an isotype control (anti-IgG, clone 2A3) on days -1, 1, 3, and 5 pi, for analysis on day 7 pi. This experimental approach allowed for a nearly complete neutrophil depletion in the blood, spleen, BALF, and lung tissue of treated animals (**Figure 30** A-D).

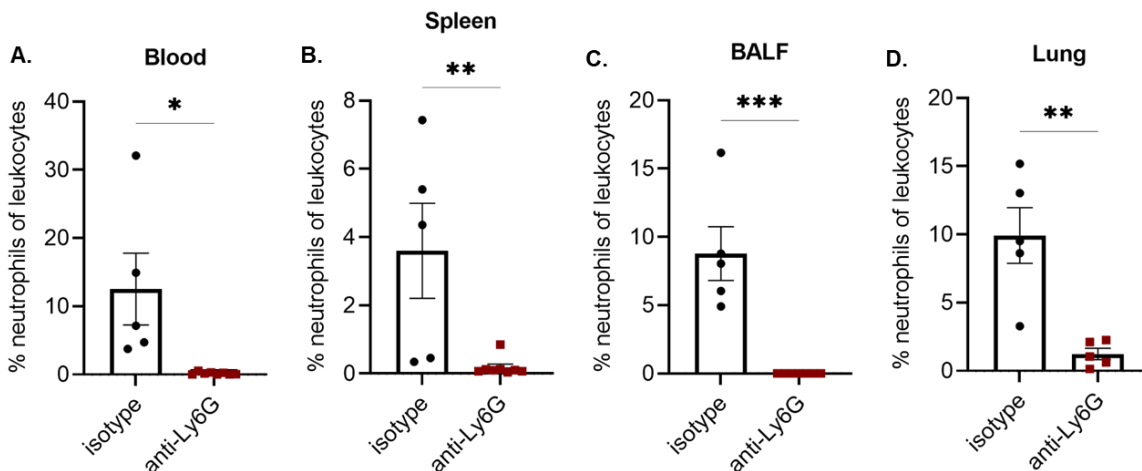


Figure 30. Neutrophil depletion can be achieved by systemic antibody administration in IAV-infected mice. (A-D) Quantification of neutrophils as percentage of leukocytes in the blood (A), spleen (B), BALF (C), and lung tissue (D) of infected animals upon neutrophil depletion. For this experiment, wild-type mice were infected with 500ffu IAV and received 200 μ g of a neutrophil-depleting antibody (anti-Ly6G) or an isotype control (clone 2A3) intraperitoneally every two days, starting one day prior to infection up to day 5 pi. Graphs represent means \pm SEM of n=5-8 animals per group, data pooled from three independent experiments.

Neutrophil-depleted mice showed a slight attenuated weight loss on day 6 pi and day 7 pi (**Figure 31** A) as well as higher BALF TR-AM numbers on day 7 pi, compared to the isotype-treated group (**Figure 31** B). Neutrophil depletion further led to a reduction in *tnfsf14* RNA levels and

tnfsf14/light protein expression in the lungs of these mice, as shown by qPCR analysis (**Figure 31 C**) and ELISA (**Figure 31 D**), respectively, further adding to the hypothesis that neutrophil-derived *tnfsf14*/light leads to TR-AM death over the course of IAV-induced pneumonia.

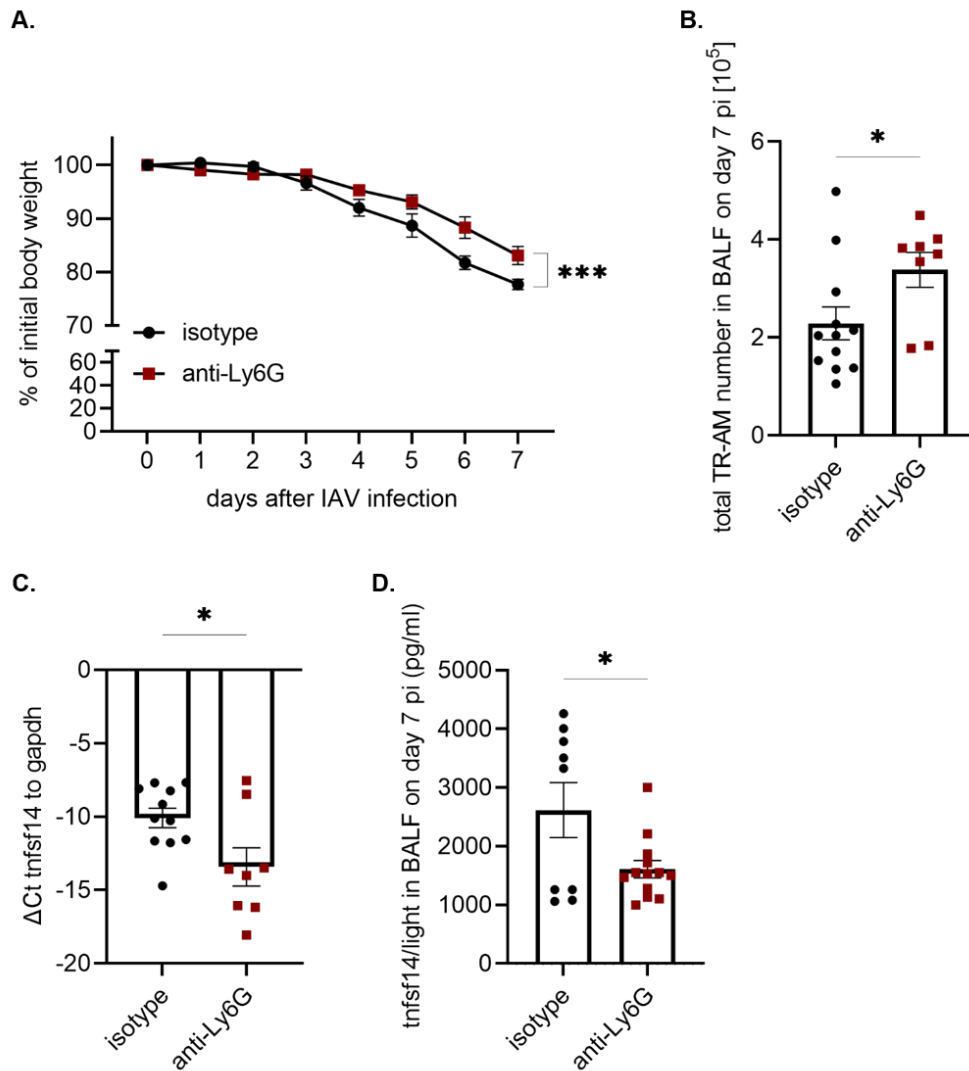


Figure 31. Neutrophil depletion attenuates TR-AM loss on day 7 pi post-IAV infection. (A) Body weight presented as percentage to initial weight upon infection and neutrophil-depleting antibody (anti-Ly6G) or isotype treatment up to day 7 pi, n=7-9 animals per group. (B) TR-AM numbers in the BALF of IAV-infected animals on day 7 pi following anti-Ly6G or isotype treatment. Graph represents means \pm SEM of n=8-12 animals per group. (C) qPCR analysis for *tnfsf14* in the lungs of anti-Ly6G- or isotype-treated animals on day 7 pi. Data represented as Δ Ct of *tnfsf14* over *gapdh*. Graph represents means \pm SEM of n=8-11 animals per group. (D) ELISA for soluble *tnfsf14*/light in the BALF of IAV-infected and anti-Ly6G- or isotype-treated animals on day 7 pi. Graph represents means \pm SEM of n=9-13 animals.

Tnfsf14/Light exerts its pro-apoptotic effect on TR-AM mainly via the $lt\beta r$ receptor following IAV infection

Tnfsf14/Light ligation on target cells involves two receptors, *tnfrsf14/hvem* and $lt\beta r$, with diverse outcomes, depending on receptor, cell type, and microenvironment [150, 151]. Tnfsf14/Hvem lacks a death domain and mainly initiates intracellular pro-inflammatory responses, which may indirectly lead to cell death, whereas $lt\beta r$ can directly act as a death receptor [150, 158, 159], raising the question which of the two receptors is mainly responsible for the pro-apoptotic effect of *tnfsf14/light* on TR-AM and whether their genetic deletion has any additional effect on the response to IAV infection. No differences could be detected between *tnfrsf14^{-/-}* and *ltβr^{-/-}* mice regarding EpCAM⁺ epithelial cell numbers (**Figure 32 A**) or viral titers (**Figure 32 B**) following IAV infection, which indicated that lack of either of the two receptors had no direct effect on viral propagation or virus-induced lung injury. However, leukocyte influx in the alveoli presented distinct patterns on day 7 pi: No differences could be detected in BALF neutrophil and NKT cell numbers (**Figure 32 C, D**). BMDM, NK, and T cells were considerably lower in *ltβr^{-/-}* mice than their *tnfrsf14^{-/-}* counterparts, while a significant increase in B cell numbers was observed in this group (**Figure 32 C, D**). More importantly, TR-AM loss was significantly attenuated in these mice (**Figure 32 E**), yet not completely abrogated, as observed in *tnfrsf14^{-/-}* mice (**Figure 23**). This hints at a potential role of *tnfrsf14/hvem* in IAV-induced TR-AM death, which is, however, predominantly governed by $lt\beta r$.

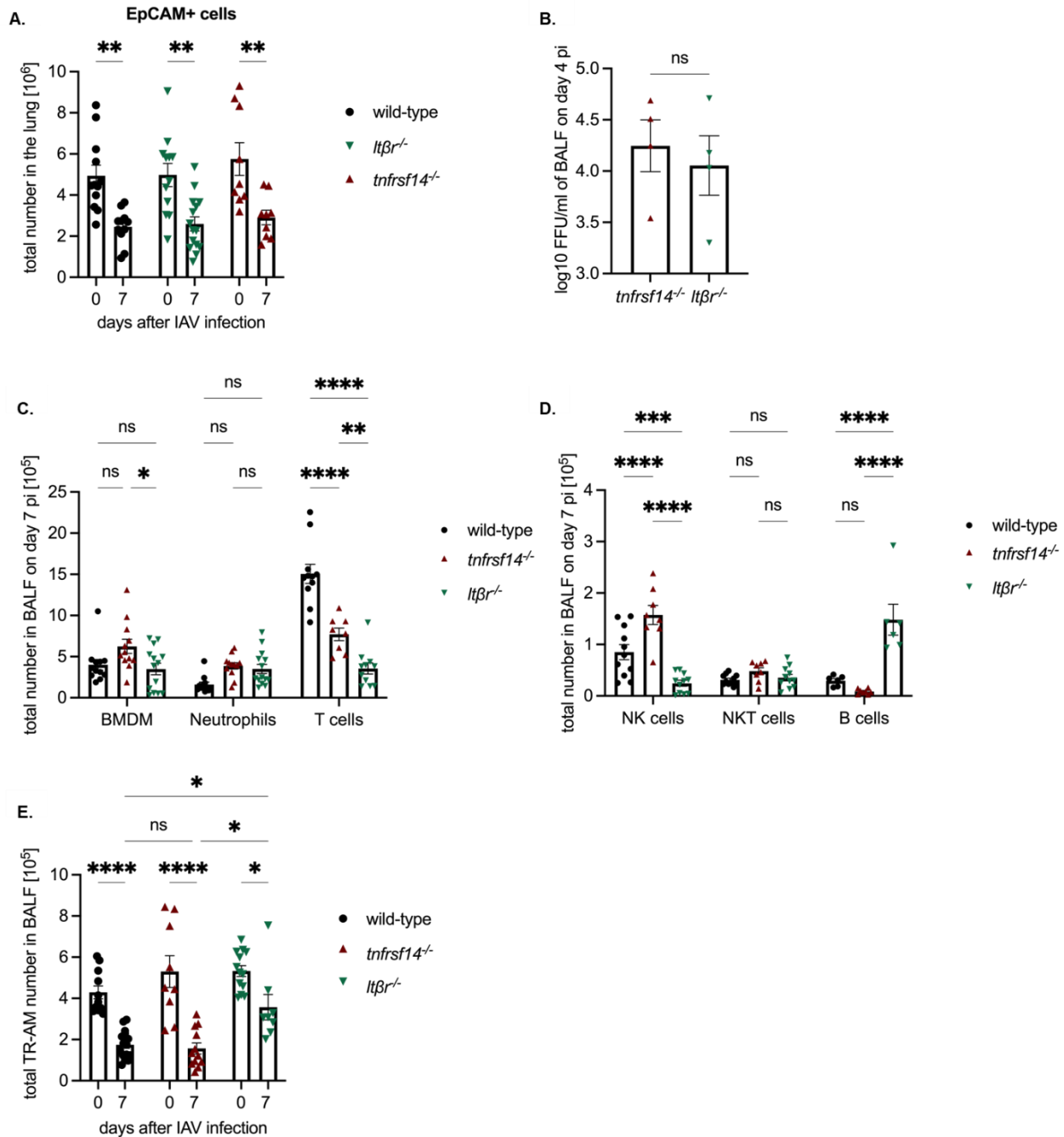


Figure 32. *Ltβr*^{-/-} but not *tnfrsf14*^{-/-} mice are characterized by an attenuated TR-AM loss upon IAV infection. (A) Quantification of EpCAM⁺ cells on day 0 and day 7 pi in the lungs of wild-type, *tnfrsf14*^{-/-}, and *ltβr*^{-/-} mice after infection with 500ffu IAV. Graph represents means ± SEM of n=9-15 animals per group. (B) Viral titers as measured in the BALF of IAV-infected *tnfrsf14*^{-/-} and *ltβr*^{-/-} mice on day 4 pi. Graph represents means ± SEM of n=4 animals per group. (C-D) Quantification of different immune cell populations, including BMDM, neutrophils, NK, NKT cells, T and B cells in the BALF of wild-type, *tnfrsf14*^{-/-}, and *ltβr*^{-/-} mice on day 7 pi following infection with 500ffu IAV. Graphs represent means ± SEM of n=9-16 animals per group. (E) Quantification of TR-AM numbers in the BALF of

wild-type, *tnfrsf14*^{-/-}, and *ltβr*^{-/-} mice on day 0 and day 7 pi. Graph represents means ± SEM of 9-15 mice per group, data pooled from 5 different experiments.

Loss of *tnfsf14*/light improves clinical outcome following post-IAV pneumococcal pneumonia

TR-AM depletion upon IAV-induced pneumonia was shown to be significantly attenuated through loss of the *tnfsf14*/light ligand. Since loss of the first line of lung defense paves the way towards the establishment of secondary bacterial pneumonia [119], the effect of improved TR-AM survival through *tnfsf14*/light loss was interrogated in the context of post-viral pneumococcal infection. To that end, wild-type and *tnfsf14*^{-/-} mice were subjected to a co-infection model, as described above (**Figure 10**). Loss of *tnfsf14*/light led to improved survival and attenuated weight loss following IAV and *Spn* co-infection (**Figure 33 A, B**). Bacterial load was lower in the BALF and in the lungs of co-infected *tnfsf14*^{-/-} mice (**Figure 33 C, D**) on day 9 pi, which was chosen as the first time point after co-infection mice had to be euthanized due to high clinical scoring, as described in the 'Methods' section. Additionally, higher BALF TR-AM numbers were observed in *tnfsf14*^{-/-} mice (**Figure 33 E**) on that time point. Since no difference could be detected regarding the phagocytosis capacity of TR-AM between wild-type and *tnfsf14*^{-/-} mice at the time point of pneumococcal infection (day 7 pi) (**Figure 33 F**), improved bacterial clearance in the *tnfsf14*^{-/-} mice could be explained by the preservation of the TR-AM pool demonstrated by that group. To exclude any other factor except TR-AM survival contributing to these findings, adoptive transfer of wild-type, *ltβr*^{-/-}, and *tnfrsf14*^{-/-} TR-AM from non-infected mice (300,000-500,000 cells/0.05ml PBS) was performed on day 3 after IAV infection, followed by pneumococcal superinfection on day 7 pi. No mice receiving PBS only or *tnfrsf14*^{-/-} TR-AM survived the co-infection, whereas transfer of *ltβr*^{-/-} TR-AM offered the highest probability of survival, even though no significant difference could be demonstrated to transfer of wild-type TR-AM (**Figure 33 G**). This finding once again suggests that *tnfrsf14*/hvem may play an indirect role in TR-AM death, which is, however, mainly linked to *ltβr* expression and *tnfsf14* ligation. In terms of a therapeutic approach, use of an anti-*tnfsf14*/light neutralizing antibody led to improved survival following co-infection, thus offering a promising candidate for future therapeutic strategies (**Figure 33 H**).

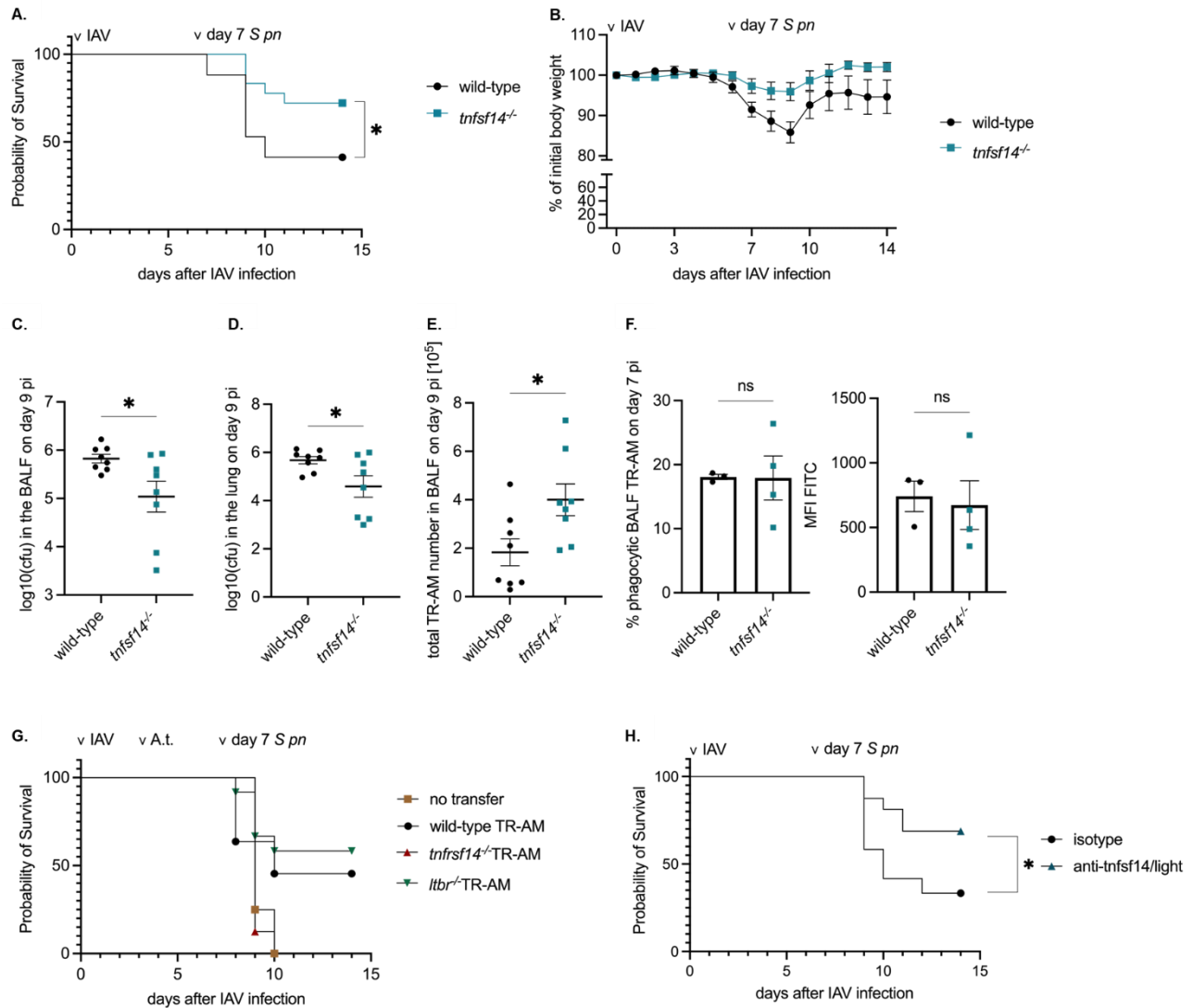


Figure 33. Loss of *tnfsf14/light* is linked to an improved clinical outcome upon IAV and *Spn* co-infection. (A-B)

Survival and weight curve expressed as percentage of initial body weight after infection of wild-type and *tnfsf14*^{-/-} mice with 250ffu IAV on day 0 pi and 20-50cfu *Spn* on day 7 pi. Graphs represent means ± SEM of n=17-18 animals per group. (C-D) Bacterial load in the BALF (C) and in the lungs (D) of wild-type and *tnfsf14*^{-/-} mice on day 9 pi following co-infection with 250ffu IAV (day 0) and 20-50cfu *Spn* (day 7 pi). Graphs represent means ± SEM of n=8 animals per group, data pooled from 4 different experiments. (E) TR-AM numbers in the BALF of wild-type and *tnfsf14*^{-/-} mice on day 9 pi following co-infection with 250ffu IAV (day 0) and 20-50cfu *Spn* (day 7 pi). Graph represents means ± SEM of n=3-4 animals per group. (F) Phagocytosis analysis of wild-type and *tnfsf14*^{-/-} TR-AM, as depicted by percentage of phagocytic TR-AM (l) and phagocytosis capacity (r). On day 7 pi, BALF-isolated cells from each mice group were incubated with GFP-stained *E. coli* at 4° and 37°C for 15min, followed by an additional 20min of surface marker staining, after which flow cytometry analysis was performed. Phagocytosis capacity was defined as (MFI_{stained}-MFI_{unstained})_{37°C}-(MFI_{stained}-MFI_{unstained})_{4°C} and combined with surface staining of BALF cells to identify

phagocytic TR-AM. Graphs represent means \pm SEM of n=3-4 animals per group. (G) Survival of wild-type mice upon co-infection (250ffu IAV on day 0, 20-50cfu *Spn* on day 7 pi) with adoptive transfer of 300,000-500,000 wild-type, *tnfrsf14*^{-/-} or *ltbr*^{-/-} TR-AM, or PBS treatment, on day 3 pi. Graph represents means \pm SEM of n=4-12 animals per group. (H) Survival following co-infection of wild-type mice and treatment with 500 μ g of a specific blocking anti-tnfsf14/light antibody or an isotype control on day 2 pi. Graph represents means \pm SEM of n=12-16 animals per group.

5. Discussion

Influenza A virus (IAV) infection can manifest in a broad spectrum of disease, from mild upper airway irritation to severe pneumonia, which may progress to ARDS [58, 60]. In the latter case, virus- and immune system-driven processes compromise the integrity of the blood-gas barrier, thereby endangering the exchange of oxygen and carbon dioxide and causing respiratory distress [45, 46]. A cascade of immunological events characterizes this phase. TR-AM depletion significantly compromises local immunity, as these cells initiate direct antiviral responses, orchestrate intercellular communication through extensive cytokine and chemokine release, support antibody production, drive repair of alveolar epithelial cells, and orchestrate the return to homeostasis, limiting inflammation and lung injury [77, 89, 91, 196]. Recruited leukocytes compensate for the loss of the first line of defense and eventually limit viral dissemination, clear the lung of virus particles and cell debris, establish infection memory, and eventually initiate tissue-repair mechanisms and the return to homeostasis [58, 60, 95, 109, 112, 197-199]. This highly inflammatory immune response, though beneficial for viral clearance, can also be associated with extensive lung injury [42, 101, 102, 200]. Cytokine- or death ligand-driven damage of the epithelial barrier has been the subject of many studies, in addition to epithelial cell death following intracellular viral replication [136, 144, 201-204]. The mechanisms driving TR-AM loss are, however, poorly understood in comparison.

In a mouse model of IAV infection, severe pneumonia was caused following orotracheal virus application. Even though mice are no natural hosts for IAV, several human strains, including the A/Puerto Rico/8/1934 (H1N1) isolate, have shown high infectivity in this model. However, certain parameters of human IAV infection, such as virus transmission or Th1/Th2 response, cannot be recapitulated or show discrepancies in the murine model [205]. Mouse strain further seems to play an important role in infection susceptibility, which could explain the discrepant results of studies on IAV infection in mice with different background [206-208]. Despite its limitations, the murine IAV infection model has been established as the method of choice for the study of the infection course and the specific pathways involved in IAV-induced pathology, due to handling ease, feasibility of genetic manipulation, and high reproducibility [205, 207].

In the current study, TR-AM were significantly decreased on day 3 pi, reaching their lowest numbers on day 7 pi after IAV infection. On day 14 pi, TR-AM had been completely restored, even exceeding original numbers, which is in accordance with previously published data [127, 145, 198,

206, 209]. As opposed to the drastically diminishing TR-AM population, other immune cell populations, such as bone marrow-derived macrophages (BMDM), neutrophils, natural killer cells, and lymphocytes, entered the alveoli in increasing numbers at distinct time points during the infection course and slowly returned to their baseline levels as inflammation subsided [101, 198]. A few days after infection, immune cell influx gradually declined, while TR-AM numbers were restored, mainly through the contribution of newly recruited BMDM [42, 95, 101, 116]. IAV-induced inflammation has been shown to cause diverse epigenetic changes on TR-AM, associated with long-term immunoparalysis [210]. In addition to that, infection-primed BMDM have been attributed a transient advantage over the original TR-AM regarding later infection with bacterial pathogens [116]. TR-AM death upon IAV infection could, therefore, be interpreted as the removal of virus-compromised cells in favor of their more pro-inflammatory counterparts, which are better suited for promoting virus containment and post-infection local immunity. However, TR-AM death can also contribute to viral dissemination through the loss of TR-AM antiviral properties (e.g. interferon production) as well as tissue damage, as released apoptotic bodies and cell debris are strong immunogenic response inducers [201, 211, 212]. Moreover, several studies have associated BMDM with an excessively pro-inflammatory phenotype during acute infection and the promotion of aberrant lung remodeling upon infection resolution [42, 80, 99, 100, 213-215]. Despite the fact that BMDM gradually shift from a pro-inflammatory to a pro-regenerative phenotype as they are gradually integrated into the TR-AM pool during late infection [42], lack of TR-AM and the highly injurious phenotype of BMDM during the acute phase create a window of immunological vulnerability, thus increasing susceptibility to secondary bacterial infection. Preservation of the original TR-AM pool in balance with BMDM influx could, therefore, mitigate local inflammation, accelerate the return to homeostasis, and protect from bacterial superinfection [124]. Elucidating the mechanisms involved in TR-AM death hence offers the opportunity to improve host defense in the context of subsequent lung infections, a rather common and highly relevant clinical entity in the era of emerging viral pathogens and widespread antibiotic resistance.

The depletion of the TR-AM niche was found to be associated with increasing numbers of apoptotic cells during the infection course. At the same time, a high upregulation of several apoptosis-related genes was observed in flow-sorted TR-AM from infected mice on day 3 and day 7 pi, compared to macrophages from non-infected mice. Though not as prominent as in the case of apoptosis, genes belonging to the autophagy and necrosis pathway were also upregulated, in line with previously

published data on TR-AM death in the context of sterile inflammation and bacterial infection [216, 217]. As direct viral infection leads to the apoptotic death of alveolar epithelial cells (AEC) upon IAV infection [201], a possible hypothesis was that this might be the case with TR-AM as well. However, IAV hemagglutinin-positive TR-AM numbers remained constant and quite low compared to hemagglutinin-negative TR-AM during the infection course, in line with the previously described abortive infection of TR-AM upon IAV infection [77] .

Viral infection, particularly with highly pathogenic viruses, has been shown to initiate the apoptosis pathway in several macrophage populations, including TR-AM, leading to cell death [79, 218-220]. The low number of directly infected TR-AM, however, hinted that an alternative mechanism was mainly responsible for driving TR-AM loss in this model of IAV-induced pneumonia. These results were corroborated by a series of *ex vivo* experiments, where treatment of naïve TR-AM with UV-inactivated BALF from infected mice drastically reduced survival and increased caspase-3 and caspase-8 activity 24h later. This raised the question whether caspase inhibition could attenuate TR-AM apoptosis.

The use of caspase inhibitors has been widely established in the context of IAV infection. Application of a caspase-10 inhibitor in a culture of human monocyte-derived macrophages infected with H5N1 was shown to decrease apoptotic rates [147], whereas caspase-3 inhibition has been demonstrated to decrease viral titers in the supernatant of MDCK, Vero, and A549 cells infected with influenza A H7N7 virus [192]. In the present model, post-treatment survival of TR-AM could be improved when a specific caspase-8 inhibitor was used, however, little effect was shown when a caspase-3 inhibitor was used. This may reflect the inevitability of cell death once the apoptosis pathway has been initiated, which can be prevented once the pathway is blocked at its beginning. Similar to the *in vitro* results, *in vivo* use of a caspase-8 inhibitor fully restored TR-AM numbers on day 3 pi as opposed to the DMSO control and significantly attenuated TR-AM loss on day 7 pi.

Apoptosis holds a versatile role in IAV infection [221]. During the early stages of the virus replication cycle, the virus manipulates the apoptotic machinery of the cell into inhibition of the pro-apoptotic pathway, since the prolongation of the cell's life enables longer viral propagation [65, 73, 192]. Viral proteins NS1, PB1-F2, and M2 have been identified as key manipulators of programmed cell death [65, 201]. Interestingly, apoptosis can prove beneficial during an intermediate phase of the replication cycle, as blocking of caspase-3 has been shown to hinder

efficient viral propagation through nuclear retention of viral RNP complexes [192]. As infection progresses and host immune response mechanisms are initiated, infected cells and phagocytes undergo an apoptotic death in order to secure viral clearance [222, 223], while the virus itself orchestrates the apoptotic death of immune cells as a form of escaping elimination [73].

Caspase-8 is a key molecule in mediating both the (extrinsic and intrinsic) apoptotic and the necrotic intracellular death pathway [193, 201]. The inability to completely prevent macrophage death despite the use of an apoptosis inhibitor may therefore be explained by the abundance of death signals present in the BALF of infected mice on day 7 pi, which could drive cell fate towards necrosis, once the apoptosis pathway is blocked. Targeting cell death-initiating mechanisms which precede the recruitment and activation of caspase-8, therefore, presented a more efficient solution for IAV-induced TR-AM depletion. As UV inactivation prior to BALF treatment of TR-AM excluded the interference of any living viral particles or cells, involvement of a soluble, death-inducing ligand was the most probable explanation for the decreased TR-AM survival after 24h of treatment.

The role of death-inducing ligands, particularly those belonging to the tumor necrosis factor superfamily (TNFSF), such as TRAIL and FasL, has been studied quite extensively in the context of IAV infection [99, 136, 145]. Gene expression analysis of flow-sorted TR-AM from infected mice revealed an upregulation of various members of the TNFSF at different infection time points. One receptor standing out was tumor necrosis factor receptor superfamily 14 or herpesvirus entry mediator (*tnfrsf14/hvem*), a receptor for tumor necrosis factor superfamily 14 (*tnfsf14* or 'light'). Since *tnfrsf14/hvem* competes for ligation to *tnfsf14/light* with the lymphotoxin beta receptor (*ltβr*) [150, 154], expression of both receptors on the surface of TR-AM was analyzed during the infection course. RNA levels of *ltβr*, a known apoptosis-inducing receptor with the ability to initiate canonical and non-canonical NF-κB pathways [158], remained relatively unchanged. However, protein expression on the surface of BALF TR-AM was increased on day 7 pi, compared to mock-infected mice. This may suggest mobilization from an intracellular compartment or enhanced translation upon infection. *Tnfrsf14/hvem* transcription was massively upregulated in the acute infection phase but returned to baseline as infection subsided. Protein levels of the receptor were also increased on day 7 pi, compared to non-infected animals. Of note, a third *tnfsf14/light* receptor, decoy receptor 3, can be found in all mammals except mice, which may suggest a different receptor regulation when these data are transferred to the human population [224]. *Tnfrsf14/hvem* is known

for initiating canonical and non-canonical NF- κ B pathways and driving immune responses, it has, however, no death-inducing domain [150, 157, 162]. Upregulation of this receptor could, therefore, enhance pro-inflammatory TR-AM abilities, support antigen presentation and T cell co-stimulation, counteract tnfsf14/light ligation to It β r, or indirectly orchestrate TR-AM death through crosstalk with a different, death-inducing receptor [225-227]. As *tnfrsf14*^{-/-} mice, however, failed to preserve their TR-AM pool 7 days post-IAV infection, while TR-AM loss was significantly attenuated in *It β r*^{-/-} mice, It β r seemed to be the main tnfsf14/light-related receptor linked to TR-AM death. Despite that, an indirect role of tnfrsf14/hvem in post-influenza TR-AM death cannot be excluded, since complete abrogation of TR-AM depletion could only be achieved in the case of *tnfsf14*^{-/-} mice. Active blocking of tnfsf14/light with a specific antibody reproduced the results of genetic deletion, offering a potential therapeutic opportunity for preserving TR-AM after IAV infection and thus improving the compromised host defense against secondary bacterial infections. Previous studies have addressed the role of tnfsf14/light in macrophage survival in a variety of models with different outcomes. Tnfsf14/Light promoted macrophage apoptosis in an It β r-dependent manner in a model of wound healing [228]. In contrast to that, it was shown to promote macrophage survival and accumulation in inflamed sites as well as the production of pro-fibrotic agents such as TGF- β , IL-1 β , IL-8 and IL-13, and the metalloproteinase MMP-9 in fibrosis models [229, 230]. Extensive studies on the role of tnfsf14/light in IAV-induced pneumonia and any implications on TR-AM survival have been, however, so far lacking.

Tnfsf14/Light is a ligand with a wide range of local environment-, disease context-, and receptor-defined functions, from lymphocyte priming to lung remodeling [172, 178, 182, 231, 232]. In this study, tnfsf14/light was highly expressed in the BALF, the parenchyma, and in the serum of infected mice. High soluble TNFSF14/LIGHT levels were also measured in the BALF of patients with severe H1N1 pneumonia or COVID-19. This is in accordance with a series of clinical studies which have demonstrated high levels of TNFSF14/LIGHT in patients with severe COVID-19 [185, 186]. Recently, a TNFSF14/LIGHT-neutralizing antibody was developed, targeting both the soluble and the membrane form of TNFSF14/LIGHT [233]. Use of this antibody was shown to reduce respiratory failure and mortality in patients with COVID-19 pneumonia (clinical trial NCT04412057) [234]. Further clinical trials are currently testing the effect of TNFSF14/LIGHT neutralization in non-eosinophilic asthma (National Library of Medicine, 2022a; NCT05288504) and Crohn's disease (National Library of Medicine, 2021; NCT03169894) [224]. With a role in

infection [185, 235-237], inflammation [170, 176, 238-240], metabolism [241, 242], and cancer [232, 243], further trials are underway, aiming at either neutralizing or exploiting the immunomodulatory properties of the ligand.

In the current study, neutrophils were identified as the main cellular source of tnfsf14/light during IAV infection. Neutrophil depletion reduced tnfsf14/light levels in the lungs of infected mice and led to an attenuated TR-AM loss on day 7 pi. Though tnfsf14/light can be expressed by several leukocyte populations [244], neutrophils have been previously implicated with tnfsf14/light production in the context of IAV infection [245] and COPD [231]. With such a deleterious effect on host defense, however, it remains unclear what drives release of tnfsf14/light by neutrophils during IAV infection. Tnfsf14/light has been shown to drive post-viral infection memory and promote antiparasitic and antibacterial inflammatory responses [153, 154, 235], which suggests a role in the establishment of efficient acute and adaptive immune response. However, lack of tnfsf14/light showed no effect on the establishment of CD8⁺ T cell memory or antibody production in a murine IAV model [177]. In the current study, *tnfsf14*^{-/-} mice presented no difference in viral titers, epithelial cell death, or cytokine profile, compared to wild-type mice. The attenuated weight loss which was, however, observed in the *tnfsf14*^{-/-} group, could be reflecting additional roles for tnfsf14/light in the lung upon IV infection, given the wide distribution of the ligand in structural and immune cell populations as well as its versatile functions, depending on the situation at hand. Tnfsf14/Light neutrophil release could alternatively reflect the highly pro-inflammatory state of these cells during severe IAV-induced pneumonia. Elevated serum TNFSF14/LIGHT levels positively correlated with disease severity and the transition to ARDS in patients who required hospitalization following severe COVID-19 [185, 186, 246, 247] or sepsis [248]. Neutrophils are among the first leukocytes to respond to pathogen invasion and as such utilize a variety of functions in order to prevent pathogen dissemination [95]. As a side effect, they can be strong inducers of lung injury, therefore neutrophil-driven post-IAV TR-AM death could be interpreted as collateral damage in the context of a dysregulated immune response to the pathogen [102], leading to increased susceptibility to further infections.

Bacterial superinfection is one of the most common and most dangerous complications of severe IAV-induced pneumonia [8, 117, 249]. IAV facilitates bacterial dissemination by revealing adhesion sites, increasing nutrient availability, and causing substantial tissue injury, which paves the way for excessive bacterial growth [249-253]. However, perhaps the most important IAV-

related factor allowing the transition to post-influenza bacterial pneumonia, is the dysregulation of host immune response, of which TR-AM depletion [93, 119, 127] and the establishment of a post-infection immunoparalysis state [210, 254, 255] are prominent examples.

TR-AM are cells with high phagocytic capacity, which can migrate towards invading pathogens and eliminate them while causing minimal tissue damage [256]. IAV infection not only drives TR-AM loss, but heavily impairs their bacterial uptake and killing capacity. Downregulation of scavenger receptors as a response to T cell-initiated interferon- γ signaling [130, 131, 257], involvement of the signal-transducer-and-activator-of-transcription (STAT)-2 pathway [258], and efferocytosis of dead cells (Better et al., preprint server BioRxiv) are among the mechanisms that mitigate the antibacterial properties of TR-AM in the aftermath of IAV infection. Moreover, targeted TR-AM migration is abrogated upon IAV infection, which leads to an inability of these cells to track and successfully engulf bacteria [256].

Despite the partially compromised bactericidal potential of TR-AM, preservation of the TR-AM pool during IAV pneumonia can offer a clinical advantage in the light of secondary bacterial infection. In a co-infection model of IAV and *Streptococcus pneumoniae*, IL-1 signaling was revealed to attenuate IAV-induced TR-AM loss and improve post-pneumococcal survival [259]. In the present work, mice presented improved survival, attenuated weight loss, and decreased bacterial titers in their lungs in the absence of *tnfsf14/light*, following post-influenza pneumococcal pneumonia. Since no differences were detected regarding TR-AM phagocytosis capacity or immune cell influx, the beneficial effect of *tnfsf14/light* deletion could be explained by the higher TR-AM numbers detected in the lungs of *tnfsf14*^{-/-} mice during the IAV infection course, which persisted even after secondary infection. Adoptive transfer of naïve *ltbr*^{-/-} TR-AM into wild-type mice also revealed a clear survival advantage over transfer of *tnfsf14*^{-/-} TR-AM in the co-infection model, emphasizing the different roles of the two *tnfsf14/light* receptors in TR-AM fate and IAV-induced disease outcome.

A new pathway involved in post-influenza depletion of the local TR-AM pool was identified in this study. During the acute infection phase, neutrophils release *tnfsf14/light*, leading to the apoptotic death of TR-AM, mainly through binding of the ligand to the *ltbr* receptor. This severely compromises host defense and enables pneumococcal dissemination in the aftermath of viral infection, which can be prevented by abrogation of *tnfsf14/light-ltbr* signaling.

6. Summary

Tissue-resident alveolar macrophage (TR-AM) depletion is a key event upon influenza A virus (IAV)-induced pneumonia and one of the most important contributors to the establishment of post-viral pneumococcal pneumonia, a common complication of severe IAV infection. However, the mechanisms behind TR-AM death remain largely unknown. In a mouse model of IAV pneumonia significant decrease in TR-AM numbers was first observed in the bronchoalveolar lavage fluid (BALF) of wild-type mice on day 3 post-infection (pi). Apoptosis was revealed as the main death-inducing pathway involved in TR-AM depletion. Treatment of naïve TR-AM with UV-inactivated BALF from infected mice resulted in significant increase in caspase-3 and caspase-8 activity after 24h, thus suggesting the involvement of a soluble, death-inducing ligand in post-influenza TR-AM loss. The TNFRSF14/HVEM receptor was highly upregulated on the surface of TR-AM over the course of infection. At the same time, the respective ligand, TNFSF14/LIGHT, was found to be highly expressed in the lungs of infected mice, but also in the BALF of patients with severe IV pneumonia. These results hinted at a potential role of the TNFSF14/LIGHT ligand/receptor pathway in TR-AM death. This was confirmed in a series of *in vivo* experiments, where infected *Tnfsf14*-deficient (*tnfsf14*^{-/-}) mice and wild-type mice treated with a blocking anti-TNFSF14/LIGHT antibody retained intact TR-AM numbers over the infection course, compared to their respective controls. In addition to that, lack of TNFSF14/LIGHT resulted in an improved clinical outcome upon post-viral pneumococcal infection. Single-cell sequencing analysis of flow-sorted lung leukocytes revealed neutrophils as the main cellular source of TNFSF14/LIGHT upon IAV infection. In line with that, neutrophil depletion led to an attenuated TR-AM loss on day 7 pi. Out of the two possible receptors for TNFSF14/LIGHT, TNFRSF14/HVEM and LTβR, LTβR was identified as the main TNFSF14/LIGHT-associated receptor driving TR-AM death, as *Ltβr*-deficient (*ltβr*^{-/-}) mice presented an attenuated macrophage loss and clinical scoring following IAV infection, whereas transfer of *ltβr*^{-/-} TR-AM improved survival of wild-type mice after co-infection, in comparison to transfer of TR-AM isolated from *Tnfrsf14*-deficient (*tnfrsf14*^{-/-}) mice. In conclusion, neutrophil-released TNFSF14/LIGHT led to the apoptotic death of TR-AM mainly through the LTβ receptor upon IAV infection, thus increasing susceptibility to secondary pneumococcal pneumonia (**Figure 34**).

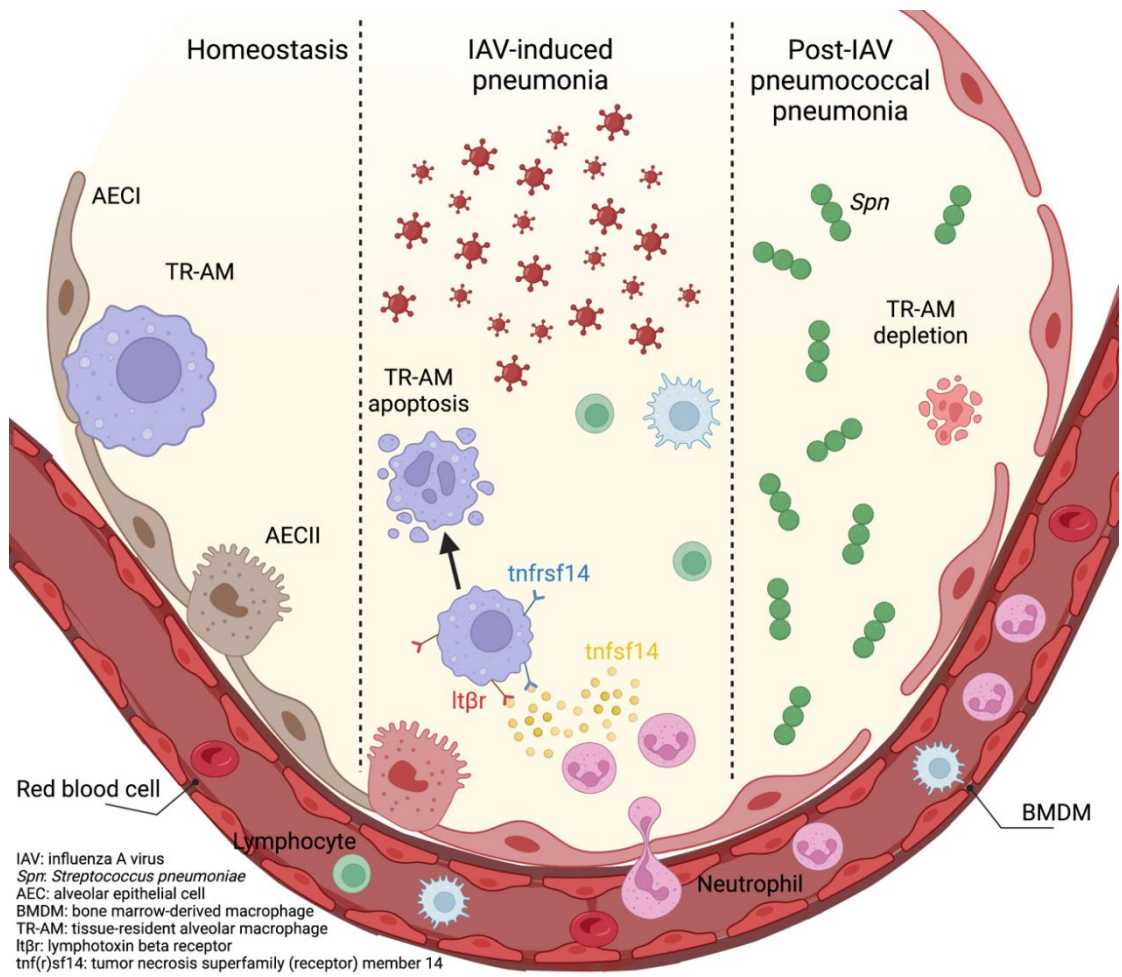


Figure 34. Synopsis of proposed mechanism of TR-AM death upon IAV-induced pneumonia. During homeostasis, TR-AM constitute the main leukocyte population of the lung (a). Upon IAV-induced pneumonia, neutrophils are recruited from the periphery, among other leukocyte populations, including BMDM and Lymphocytes. Neutrophils start releasing tnfsf14/light, which ligates to the surfaced-expressed tnfrsf14/hvem and Itβr receptors, leading to TR-AM apoptosis mainly through the latter. With the first line of defense gone, pneumococcal dissemination cannot be hindered, thus enabling the establishment of severe post-influenza pneumococcal pneumonia. Loss or blocking of tnfsf14/light, therefore, offers a promising therapeutic approach for the improvement of host defense in the light not only of IAV, but also post-viral bacterial pneumonia. Image created with BioRender.com.

7. Zusammenfassung

Die Depletierung der Geweberesidenten Alveolarmakrophagen (TR-AM) ist ein wichtiges Ereignis im Laufe der Influenza-A-Virus (IAV)-induzierten Pneumonie, die dahinterstehenden Mechanismen sind jedoch noch weitgehend unbekannt. In einem Mausmodell der IAV-Pneumonie wurde erstmals eine signifikante Abnahme der TR-AM-Zahlen in der bronchoalveolären Flüssigkeit (BALF) von Wildtyp-Mäusen am Tag 3 nach Infektion (pi) beobachtet. Apoptose wurde als der wichtigste zum Tod führende Weg identifiziert, der am Verlust der TR-AM beteiligt ist. Die Behandlung von naiven TR-AM mit UV-inaktivierter BALF aus infizierten Mäusen führte zu einem signifikanten Anstieg der Caspase-3- und Caspase-8-Aktivität 24 Stunden später, was auf die Beteiligung eines löslichen Liganden am TR-AM-Verlust nach IAV-Infektion hindeutet. Der TNFRSF14/HVEM-Rezeptor auf der Oberfläche von TR-AM war im Rahmen der Infektion stark hochreguliert. Gleichzeitig wurde auch der entsprechende Ligand, TNFSF14/LIGHT, in der Lunge infizierter Mäuse, aber auch in der BALF von Patienten mit schwerer IV-Pneumonie stark exprimiert. Diese Ergebnisse deuteten auf eine Rolle des TNFSF14/LIGHT-Ligand/Rezeptor-Signalwegs beim TR-AM-Tod hin. Dies wurde in einer Reihe von *in vivo* Experimenten im Mausmodell bestätigt. Bei infizierten *tnfsf14*^{-/-} Mäusen oder Wildtyp-Mäusen, die mit einem blockierenden anti-TNFSF14/LIGHT-Antikörper behandelt wurden, blieben im Vergleich zu ihren jeweiligen Kontrollen die TR-AM-Zahlen über den Infektionsverlauf hindurch gleich. Darüber hinaus führte der Mangel an TNFSF14/LIGHT zu einem verbesserten klinischen Verlauf nach einer postviralen Pneumokokkeninfektion. Die Single-cell-Sequenzierungsanalyse von durchflusssortierten Lungenleukozyten ergab, dass Neutrophile die wichtigste zelluläre Quelle von TNFSF14/LIGHT bei einer IAV-Infektion sind. Dementsprechend führte die Neutrophilendepletierung zu einem abgeschwächten TR-AM-Verlust am Tag 7 pi. Von den beiden möglichen Rezeptoren für TNFSF14/LIGHT, TNFRSF14/HVEM und LTβR, wurde LTβR als der wichtigste TNFSF14/LIGHT-assoziierte Rezeptor identifiziert, der den TR-AM-Tod vorantreibt, da *ltβr*^{-/-} Mäuse einen abgeschwächten Makrophagenverlust aufwiesen, während der adoptive Transfer von *ltβr*^{-/-} TR-AM das Überleben von Wildtyp-Tieren nach Co-Infektion vorantrieb, im Gegensatz zum TR-AM-Transfer von *tnfrsf14*^{-/-} Mäusen. Zusammenfassend lässt sich sagen, dass das von Neutrophilen freigesetzte TNFSF14/LIGHT bei einer IAV-Infektion hauptsächlich über den LTβ-Rezeptor zum apoptotischen Tod von TR-AM führt und damit die Anfälligkeit für sekundäre Pneumokokken-Pneumonie erhöht.

8. References

1. Hsia, C.C., D.M. Hyde, and E.R. Weibel, *Lung Structure and the Intrinsic Challenges of Gas Exchange*, in *Compr Physiol*. 2016. p. 827-95.
2. Weibel, E.R., *It takes more than cells to make a good lung*, in *Am J Respir Crit Care Med*. 2013. p. 342-6.
3. Weibel, E.R., *On the tricks alveolar epithelial cells play to make a good lung*, in *Am J Respir Crit Care Med*. 2015. p. 504-13.
4. Weibel, E.R., *Lung morphometry: the link between structure and function*, in *Cell Tissue Res*. 2017. p. 413-426.
5. Hogan, B.L., et al., *Repair and regeneration of the respiratory system: complexity, plasticity, and mechanisms of lung stem cell function*. *Cell Stem Cell*, 2014. **15**(2): p. 123-38.
6. Martin, T.R. and C.W. Frevert, *Innate immunity in the lungs*, in *Proc Am Thorac Soc*. 2005. p. 403-11.
7. Werner, J.L. and C. Steele, *Innate receptors and cellular defense against pulmonary infections*. *J Immunol*, 2014. **193**(8): p. 3842-50.
8. Okahashi, N., et al., *Secondary streptococcal infection following influenza*. *Microbiol Immunol*, 2022. **66**(6): p. 253-263.
9. Ginhoux, F. and S. Jung, *Monocytes and macrophages: developmental pathways and tissue homeostasis*. *Nat Rev Immunol*, 2014. **14**(6): p. 392-404.
10. Guillems, M., et al., *Dendritic cells, monocytes and macrophages: a unified nomenclature based on ontogeny*. *Nat Rev Immunol*, 2014. **14**(8): p. 571-8.
11. Ginhoux, F., et al., *New insights into the multidimensional concept of macrophage ontogeny, activation and function*. *Nat Immunol*, 2016. **17**(1): p. 34-40.
12. Epelman, S., K.J. Lavine, and G.J. Randolph, *Origin and functions of tissue macrophages*. *Immunity*, 2014. **41**(1): p. 21-35.
13. van de Laar, L., et al., *Yolk Sac Macrophages, Fetal Liver, and Adult Monocytes Can Colonize an Empty Niche and Develop into Functional Tissue-Resident Macrophages*. *Immunity*, 2016. **44**(4): p. 755-68.
14. Bleriot, C., S. Chakarov, and F. Ginhoux, *Determinants of Resident Tissue Macrophage Identity and Function*. *Immunity*, 2020. **52**(6): p. 957-970.
15. Perdiguerro, E.G., et al., *The Origin of Tissue-Resident Macrophages: When an Erythro-myeloid Progenitor Is an Erythro-myeloid Progenitor*. *Immunity*, 2015. **43**(6): p. 1023-4.
16. Evren, E., E. Ringqvist, and T. Willinger, *Origin and ontogeny of lung macrophages: from mice to humans*. *Immunology*, 2019.
17. Cohen, M., et al., *Lung Single-Cell Signaling Interaction Map Reveals Basophil Role in Macrophage Imprinting*. *Cell*, 2018. **175**(4): p. 1031-1044 e18.
18. Bonnardel, J. and M. Guillems, *Developmental control of macrophage function*. *Curr Opin Immunol*, 2018. **50**: p. 64-74.
19. Guillems, M. and C.L. Scott, *Does niche competition determine the origin of tissue-resident macrophages?* *Nat Rev Immunol*, 2017. **17**(7): p. 451-460.
20. Ginhoux, F. and M. Guillems, *Tissue-Resident Macrophage Ontogeny and Homeostasis*. *Immunity*, 2016. **44**(3): p. 439-449.
21. T'Jonck, W., M. Guillems, and J. Bonnardel, *Niche signals and transcription factors involved in tissue-resident macrophage development*. *Cell Immunol*, 2018. **330**: p. 43-53.

22. Dranoff, G., et al., *Involvement of granulocyte-macrophage colony-stimulating factor in pulmonary homeostasis*. *Science*, 1994. **264**(5159): p. 713-6.
23. Scott, C.L. and M. Guillemins, *Tissue Unit-ed: Lung Cells Team up to Drive Alveolar Macrophage Development*. *Cell*, 2018. **175**(4): p. 898-900.
24. Kopf, M., C. Schneider, and S.P. Nobs, *The development and function of lung-resident macrophages and dendritic cells*. *Nat Immunol*, 2015. **16**(1): p. 36-44.
25. Joshi, N., J.M. Walter, and A.V. Misharin, *Alveolar Macrophages*. *Cell Immunol*, 2018. **330**: p. 86-90.
26. Schneider, C., et al., *Induction of the nuclear receptor PPAR-gamma by the cytokine GM-CSF is critical for the differentiation of fetal monocytes into alveolar macrophages*. *Nat Immunol*, 2014. **15**(11): p. 1026-37.
27. Halstead, E.S. and Z.C. Chroneos, *Lethal influenza infection: Is a macrophage to blame?* *Expert Rev Anti Infect Ther*, 2015. **13**(12): p. 1425-8.
28. Ebina-Shibuya, R., et al., *The double knockout of Bach1 and Bach2 in mice reveals shared compensatory mechanisms in regulating alveolar macrophage function and lung surfactant homeostasis*. *J Biochem*, 2016. **160**(6): p. 333-344.
29. Scott, C.L., et al., *The Transcription Factor ZEB2 Is Required to Maintain the Tissue-Specific Identities of Macrophages*. *Immunity*, 2018. **49**(2): p. 312-325 e5.
30. Guillemins, M., et al., *Alveolar macrophages develop from fetal monocytes that differentiate into long-lived cells in the first week of life via GM-CSF*. *J Exp Med*, 2013. **210**(10): p. 1977-92.
31. Hussell, T. and T.J. Bell, *Alveolar macrophages: plasticity in a tissue-specific context*. *Nat Rev Immunol*, 2014. **14**(2): p. 81-93.
32. Xing, J., et al., *Identification of a role for TRIM29 in the control of innate immunity in the respiratory tract*. *Nat Immunol*, 2016. **17**(12): p. 1373-1380.
33. Morales-Nebreda, L., et al., *The heterogeneity of lung macrophages in the susceptibility to disease*. *Eur Respir Rev*, 2015. **24**(137): p. 505-9.
34. Ural, B.B., et al., *Identification of a nerve-associated, lung-resident interstitial macrophage subset with distinct localization and immunoregulatory properties*. *Sci Immunol*, 2020. **5**(45).
35. Westphalen, K., et al., *Sessile alveolar macrophages communicate with alveolar epithelium to modulate immunity*. *Nature*, 2014. **506**(7489): p. 503-6.
36. Wynn, T.A., A. Chawla, and J.W. Pollard, *Macrophage biology in development, homeostasis and disease*. *Nature*, 2013. **496**(7446): p. 445-55.
37. Aggarwal, N.R., L.S. King, and F.R. D'Alessio, *Diverse macrophage populations mediate acute lung inflammation and resolution*. *Am J Physiol Lung Cell Mol Physiol*, 2014. **306**(8): p. L709-25.
38. Misharin, A.V., et al., *Flow cytometric analysis of macrophages and dendritic cell subsets in the mouse lung*. *Am J Respir Cell Mol Biol*, 2013. **49**(4): p. 503-10.
39. Gordon, S., A. Pluddemann, and F. Martinez Estrada, *Macrophage heterogeneity in tissues: phenotypic diversity and functions*. *Immunol Rev*, 2014. **262**(1): p. 36-55.
40. Murray, P.J. and T.A. Wynn, *Protective and pathogenic functions of macrophage subsets*. *Nat Rev Immunol*, 2011. **11**(11): p. 723-37.
41. Hashimoto, D., et al., *Tissue-resident macrophages self-maintain locally throughout adult life with minimal contribution from circulating monocytes*. *Immunity*, 2013. **38**(4): p. 792-804.

42. Li, F., et al., *Monocyte-derived alveolar macrophages autonomously determine severe outcome of respiratory viral infection*. *Sci Immunol*, 2022. **7**(73): p. eabj5761.
43. McQuattie-Pimentel, A.C., et al., *The lung microenvironment shapes a dysfunctional response of alveolar macrophages in aging*. *J Clin Invest*, 2021. **131**(4).
44. Schneider, J.L., et al., *The aging lung: Physiology, disease, and immunity*. *Cell*, 2021. **184**(8): p. 1990-2019.
45. Matthay, M.A., et al., *Acute respiratory distress syndrome*. *Nat Rev Dis Primers*, 2019. **5**(1): p. 18.
46. Umbrello, M., et al., *Current Concepts of ARDS: A Narrative Review*. *Int J Mol Sci*, 2016. **18**(1).
47. Matthay, M.A. and R.L. Zemans, *The acute respiratory distress syndrome: pathogenesis and treatment*. *Annu Rev Pathol*, 2011. **6**: p. 147-63.
48. Calfee, C.S., et al., *Subphenotypes in acute respiratory distress syndrome: latent class analysis of data from two randomised controlled trials*. *Lancet Respir Med*, 2014. **2**(8): p. 611-20.
49. Short, K.R., et al., *Pathogenesis of influenza-induced acute respiratory distress syndrome*. *Lancet Infect Dis*, 2014. **14**(1): p. 57-69.
50. Berthiaume, Y. and M.A. Matthay, *Alveolar edema fluid clearance and acute lung injury*. *Respir Physiol Neurobiol*, 2007. **159**(3): p. 350-9.
51. Michalski, J.E., J.S. Kurche, and D.A. Schwartz, *From ARDS to pulmonary fibrosis: the next phase of the COVID-19 pandemic?* *Transl Res*, 2022. **241**: p. 13-24.
52. George, P.M., A.U. Wells, and R.G. Jenkins, *Pulmonary fibrosis and COVID-19: the potential role for antifibrotic therapy*. *Lancet Respir Med*, 2020. **8**(8): p. 807-815.
53. Bharat, A., et al., *Lung transplantation for patients with severe COVID-19*. *Sci Transl Med*, 2020. **12**(574).
54. Herold, S., et al., *Inhaled granulocyte/macrophage colony-stimulating factor as treatment of pneumonia-associated acute respiratory distress syndrome*. *Am J Respir Crit Care Med*, 2014. **189**(5): p. 609-11.
55. Tzotzos, S.J., et al., *Incidence of ARDS and outcomes in hospitalized patients with COVID-19: a global literature survey*. *Crit Care*, 2020. **24**(1): p. 516.
56. Biehl, M., et al., *The Incremental Burden of Acute Respiratory Distress Syndrome: Long-term Follow-up of a Population-Based Nested Case-Control Study*. *Mayo Clin Proc*, 2018. **93**(4): p. 445-452.
57. Malainou, C. and S. Herold, *[Influenza]*. *Internist (Berl)*, 2019. **60**(11): p. 1127-1135.
58. Peteranderl, C., S. Herold, and C. Schmoldt, *Human Influenza Virus Infections*. *Semin Respir Crit Care Med*, 2016. **37**(4): p. 487-500.
59. Kreijtz, J.H., R.A. Fouchier, and G.F. Rimmelzwaan, *Immune responses to influenza virus infection*. *Virus Res*, 2011. **162**(1-2): p. 19-30.
60. Herold, S., et al., *Influenza virus-induced lung injury: pathogenesis and implications for treatment*. *Eur Respir J*, 2015. **45**(5): p. 1463-78.
61. Subbarao, K. and T. Joseph, *Scientific barriers to developing vaccines against avian influenza viruses*. *Nat Rev Immunol*, 2007. **7**(4): p. 267-78.
62. Tong, S., et al., *New world bats harbor diverse influenza A viruses*. *PLoS Pathog*, 2013. **9**(10): p. e1003657.
63. Wu, Y., et al., *Bat-derived influenza-like viruses H17N10 and H18N11*. *Trends Microbiol*, 2014. **22**(4): p. 183-91.

64. Reuther, P., et al., *Generation of a variety of stable Influenza A reporter viruses by genetic engineering of the NS gene segment*. Sci Rep, 2015. **5**: p. 11346.
65. Herold, S., et al., *Apoptosis signaling in influenza virus propagation, innate host defense, and lung injury*. J Leukoc Biol, 2012. **92**(1): p. 75-82.
66. Dawson, W.K., M. Lazniewski, and D. Plewczynski, *RNA structure interactions and ribonucleoprotein processes of the influenza A virus*. Brief Funct Genomics, 2018. **17**(6): p. 402-414.
67. Rossman, J.S. and R.A. Lamb, *Influenza virus assembly and budding*. Virology, 2011. **411**(2): p. 229-36.
68. Jiang, H., et al., *Influenza virus nonstructural protein 1 inhibits the production of interferon beta of alveolar epithelial cells upon the infection of influenza A H1N1*. Mol Med Rep, 2017. **16**(4): p. 4553-4560.
69. Meischel, T., et al., *Influenza A virus interactions with macrophages: Lessons from epithelial cells*. Cell Microbiol, 2020. **22**(5): p. e13170.
70. Kumar, A., et al., *Influenza virus exploits tunneling nanotubes for cell-to-cell spread*. Sci Rep, 2017. **7**: p. 40360.
71. Iwasaki, A. and P.S. Pillai, *Innate immunity to influenza virus infection*. Nat Rev Immunol, 2014. **14**(5): p. 315-28.
72. Maelfait, J., et al., *A20 Deficiency in Lung Epithelial Cells Protects against Influenza A Virus Infection*. PLoS Pathog, 2016. **12**(1): p. e1005410.
73. Martinez, I., et al., *Apoptosis, Toll-like, RIG-I-like and NOD-like Receptors Are Pathways Jointly Induced by Diverse Respiratory Bacterial and Viral Pathogens*. Front Microbiol, 2017. **8**: p. 276.
74. Pothlichet, J., et al., *Type I IFN triggers RIG-I/TLR3/NLRP3-dependent inflammasome activation in influenza A virus infected cells*. PLoS Pathog, 2013. **9**(4): p. e1003256.
75. Allen, I.C., et al., *The NLRP3 inflammasome mediates in vivo innate immunity to influenza A virus through recognition of viral RNA*. Immunity, 2009. **30**(4): p. 556-65.
76. Yu, W.C., et al., *Viral replication and innate host responses in primary human alveolar epithelial cells and alveolar macrophages infected with influenza H5N1 and H1N1 viruses*. J Virol, 2011. **85**(14): p. 6844-55.
77. Tate, M.D., et al., *Critical role of airway macrophages in modulating disease severity during influenza virus infection of mice*. J Virol, 2010. **84**(15): p. 7569-80.
78. Wang, J., et al., *Differentiated human alveolar type II cells secrete antiviral IL-29 (IFN-lambda 1) in response to influenza A infection*. J Immunol, 2009. **182**(3): p. 1296-304.
79. van Riel, D., et al., *Highly pathogenic avian influenza virus H5N1 infects alveolar macrophages without virus production or excessive TNF-alpha induction*. PLoS Pathog, 2011. **7**(6): p. e1002099.
80. Roberts, N.J., Jr., *Diverse and Unexpected Roles of Human Monocytes/Macrophages in the Immune Response to Influenza Virus*. Viruses, 2020. **12**(4).
81. Westenius, V., et al., *Highly Pathogenic H5N1 Influenza A Virus Spreads Efficiently in Human Primary Monocyte-Derived Macrophages and Dendritic Cells*. Front Immunol, 2018. **9**: p. 1664.
82. Etensohn, D.B., et al., *Human Alveolar Macrophages May Not Be Susceptible to Direct Infection by a Human Influenza Virus*. J Infect Dis, 2016. **214**(11): p. 1658-1665.
83. Londrigan, S.L., et al., *Infection of Mouse Macrophages by Seasonal Influenza Viruses Can Be Restricted at the Level of Virus Entry and at a Late Stage in the Virus Life Cycle*. J Virol, 2015. **89**(24): p. 12319-29.

84. Marvin, S.A., et al., *Influenza Virus Overcomes Cellular Blocks To Productively Replicate, Impacting Macrophage Function*. J Virol, 2017. **91**(2).
85. Londrigan, S.L., et al., *IFITM3 and type I interferons are important for the control of influenza A virus replication in murine macrophages*. Virology, 2020. **540**: p. 17-22.
86. Ma, J.Z., et al., *Unique Transcriptional Architecture in Airway Epithelial Cells and Macrophages Shapes Distinct Responses following Influenza Virus Infection Ex Vivo*. J Virol, 2019. **93**(6).
87. Ghosh, S., et al., *MARCO regulates early inflammatory responses against influenza: a useful macrophage function with adverse outcome*. Am J Respir Cell Mol Biol, 2011. **45**(5): p. 1036-44.
88. Wang, J., et al., *Innate immune response of human alveolar macrophages during influenza A infection*. PLoS One, 2012. **7**(3): p. e29879.
89. Cardani, A., et al., *Alveolar Macrophages Prevent Lethal Influenza Pneumonia By Inhibiting Infection Of Type-1 Alveolar Epithelial Cells*. PLoS Pathog, 2017. **13**(1): p. e1006140.
90. Wong, C.K., et al., *Aging Impairs Alveolar Macrophage Phagocytosis and Increases Influenza-Induced Mortality in Mice*. J Immunol, 2017. **199**(3): p. 1060-1068.
91. Schneider, C., et al., *Alveolar macrophages are essential for protection from respiratory failure and associated morbidity following influenza virus infection*. PLoS Pathog, 2014. **10**(4): p. e1004053.
92. Kim, H.M., et al., *Alveolar macrophages are indispensable for controlling influenza viruses in lungs of pigs*. J Virol, 2008. **82**(9): p. 4265-74.
93. Purnama, C., et al., *Transient ablation of alveolar macrophages leads to massive pathology of influenza infection without affecting cellular adaptive immunity*. Eur J Immunol, 2014. **44**(7): p. 2003-12.
94. Kim, H.M., et al., *The severe pathogenicity of alveolar macrophage-depleted ferrets infected with 2009 pandemic H1N1 influenza virus*. Virology, 2013. **444**(1-2): p. 394-403.
95. Lamichhane, P.P. and A.E. Samarasinghe, *The Role of Innate Leukocytes during Influenza Virus Infection*. J Immunol Res, 2019. **2019**: p. 8028725.
96. Weiss, I.D., et al., *IFN-gamma treatment at early stages of influenza virus infection protects mice from death in a NK cell-dependent manner*. J Interferon Cytokine Res, 2010. **30**(6): p. 439-49.
97. Ho, L.P., et al., *Activation of invariant NKT cells enhances the innate immune response and improves the disease course in influenza A virus infection*. Eur J Immunol, 2008. **38**(7): p. 1913-22.
98. Herold, S., et al., *Lung epithelial apoptosis in influenza virus pneumonia: the role of macrophage-expressed TNF-related apoptosis-inducing ligand*. J Exp Med, 2008. **205**(13): p. 3065-77.
99. Ellis, G.T., et al., *TRAIL+ monocytes and monocyte-related cells cause lung damage and thereby increase susceptibility to influenza-Streptococcus pneumoniae coinfection*. EMBO Rep, 2015. **16**(9): p. 1203-18.
100. Lin, K.L., et al., *CCR2+ monocyte-derived dendritic cells and exudate macrophages produce influenza-induced pulmonary immune pathology and mortality*. J Immunol, 2008. **180**(4): p. 2562-72.
101. Perrone, L.A., et al., *H5N1 and 1918 pandemic influenza virus infection results in early and excessive infiltration of macrophages and neutrophils in the lungs of mice*. PLoS Pathog, 2008. **4**(8): p. e1000115.

102. Tang, B.M., et al., *Neutrophils-related host factors associated with severe disease and fatality in patients with influenza infection*. Nat Commun, 2019. **10**(1): p. 3422.
103. Brandes, M., et al., *A systems analysis identifies a feedforward inflammatory circuit leading to lethal influenza infection*. Cell, 2013. **154**(1): p. 197-212.
104. Aaboud, M., et al., *Search for Low-Mass Dijet Resonances Using Trigger-Level Jets with the ATLAS Detector in pp Collisions at $\sqrt{s}=13$ TeV*. Phys Rev Lett, 2018. **121**(8): p. 081801.
105. Abdul-Careem, M.F., et al., *Critical role of natural killer cells in lung immunopathology during influenza infection in mice*. J Infect Dis, 2012. **206**(2): p. 167-77.
106. Nussing, S., et al., *Innate and adaptive T cells in influenza disease*. Front Med, 2018. **12**(1): p. 34-47.
107. Unkel, B., et al., *Alveolar epithelial cells orchestrate DC function in murine viral pneumonia*. J Clin Invest, 2012. **122**(10): p. 3652-64.
108. Helft, J., et al., *Cross-presenting CD103+ dendritic cells are protected from influenza virus infection*. J Clin Invest, 2012. **122**(11): p. 4037-47.
109. Brincks, E.L., et al., *CD8 T cells utilize TRAIL to control influenza virus infection*. J Immunol, 2008. **181**(7): p. 4918-25.
110. Zhou, J., et al., *Functional tumor necrosis factor-related apoptosis-inducing ligand production by avian influenza virus-infected macrophages*. J Infect Dis, 2006. **193**(7): p. 945-53.
111. Califano, D., et al., *IFN-gamma increases susceptibility to influenza A infection through suppression of group II innate lymphoid cells*. Mucosal Immunol, 2018. **11**(1): p. 209-219.
112. Monticelli, L.A., et al., *Innate lymphoid cells promote lung-tissue homeostasis after infection with influenza virus*. Nat Immunol, 2011. **12**(11): p. 1045-54.
113. Cheng, P., S. Li, and H. Chen, *Macrophages in Lung Injury, Repair, and Fibrosis*. Cells, 2021. **10**(2).
114. Allard, B., A. Panariti, and J.G. Martin, *Alveolar Macrophages in the Resolution of Inflammation, Tissue Repair, and Tolerance to Infection*. Front Immunol, 2018. **9**: p. 1777.
115. Narasaraju, T., et al., *MCP-1 antibody treatment enhances damage and impedes repair of the alveolar epithelium in influenza pneumonitis*. Am J Respir Cell Mol Biol, 2010. **42**(6): p. 732-43.
116. Aegerter, H., et al., *Influenza-induced monocyte-derived alveolar macrophages confer prolonged antibacterial protection*. Nat Immunol, 2020. **21**(2): p. 145-157.
117. Lim, Y.K., et al., *Impact of bacterial and viral coinfection in community-acquired pneumonia in adults*. Diagn Microbiol Infect Dis, 2019. **94**(1): p. 50-54.
118. Hanada, S., et al., *Respiratory Viral Infection-Induced Microbiome Alterations and Secondary Bacterial Pneumonia*. Front Immunol, 2018. **9**: p. 2640.
119. McCullers, J.A., *The co-pathogenesis of influenza viruses with bacteria in the lung*. Nat Rev Microbiol, 2014. **12**(4): p. 252-62.
120. Morens, D.M., J.K. Taubenberger, and A.S. Fauci, *Predominant role of bacterial pneumonia as a cause of death in pandemic influenza: implications for pandemic influenza preparedness*. J Infect Dis, 2008. **198**(7): p. 962-70.
121. Habibzay, M., G. Weiss, and T. Hussell, *Bacterial superinfection following lung inflammatory disorders*. Future Microbiol, 2013. **8**(2): p. 247-56.
122. Braciale, T.J., J. Sun, and T.S. Kim, *Regulating the adaptive immune response to respiratory virus infection*. Nat Rev Immunol, 2012. **12**(4): p. 295-305.

123. Siegel, S.J., A.M. Roche, and J.N. Weiser, *Influenza promotes pneumococcal growth during coinfection by providing host sialylated substrates as a nutrient source*. Cell Host Microbe, 2014. **16**(1): p. 55-67.
124. Kash, J.C. and J.K. Taubenberger, *The role of viral, host, and secondary bacterial factors in influenza pathogenesis*. Am J Pathol, 2015. **185**(6): p. 1528-36.
125. McAuley, J.L., et al., *Expression of the 1918 influenza A virus PB1-F2 enhances the pathogenesis of viral and secondary bacterial pneumonia*. Cell Host Microbe, 2007. **2**(4): p. 240-9.
126. Connolly, E. and T. Hussell, *The Impact of Type 1 Interferons on Alveolar Macrophage Tolerance and Implications for Host Susceptibility to Secondary Bacterial Pneumonia*. Front Immunol, 2020. **11**: p. 495.
127. Ghoneim, H.E., P.G. Thomas, and J.A. McCullers, *Depletion of alveolar macrophages during influenza infection facilitates bacterial superinfections*. J Immunol, 2013. **191**(3): p. 1250-9.
128. Smith, A.M. and A.P. Smith, *A Critical, Nonlinear Threshold Dictates Bacterial Invasion and Initial Kinetics During Influenza*. Sci Rep, 2016. **6**: p. 38703.
129. Nickerson, C.L. and G.J. Jakab, *Pulmonary antibacterial defenses during mild and severe influenza virus infection*. Infect Immun, 1990. **58**(9): p. 2809-14.
130. Wu, M., et al., *Immunomodulators targeting MARCO expression improve resistance to postinfluenza bacterial pneumonia*. Am J Physiol Lung Cell Mol Physiol, 2017. **313**(1): p. L138-L153.
131. Sun, K. and D.W. Metzger, *Inhibition of pulmonary antibacterial defense by interferon-gamma during recovery from influenza infection*. Nat Med, 2008. **14**(5): p. 558-64.
132. Robinson, K.M., J.K. Kolls, and J.F. Alcorn, *The immunology of influenza virus-associated bacterial pneumonia*. Curr Opin Immunol, 2015. **34**: p. 59-67.
133. Rynda-Apple, A., K.M. Robinson, and J.F. Alcorn, *Influenza and Bacterial Superinfection: Illuminating the Immunologic Mechanisms of Disease*. Infect Immun, 2015. **83**(10): p. 3764-70.
134. FitzGerald, E.S., N.F. Luz, and A.M. Jamieson, *Competitive Cell Death Interactions in Pulmonary Infection: Host Modulation Versus Pathogen Manipulation*. Front Immunol, 2020. **11**: p. 814.
135. Kist, M. and D. Vucic, *Cell death pathways: intricate connections and disease implications*. EMBO J, 2021. **40**(5): p. e106700.
136. Peteranderl, C. and S. Herold, *The Impact of the Interferon/TNF-Related Apoptosis-Inducing Ligand Signaling Axis on Disease Progression in Respiratory Viral Infection and Beyond*. Front Immunol, 2017. **8**: p. 313.
137. Walczak, H., *Death receptor-ligand systems in cancer, cell death, and inflammation*. Cold Spring Harb Perspect Biol, 2013. **5**(5): p. a008698.
138. Ward-Kavanagh, L.K., et al., *The TNF Receptor Superfamily in Co-stimulating and Co-inhibitory Responses*. Immunity, 2016. **44**(5): p. 1005-19.
139. D'Arcy, M.S., *Cell death: a review of the major forms of apoptosis, necrosis and autophagy*. Cell Biol Int, 2019. **43**(6): p. 582-592.
140. Kuai, J., et al., *Endogenous association of TRAF2, TRAF3, cIAP1, and Smac with lymphotoxin beta receptor reveals a novel mechanism of apoptosis*. J Biol Chem, 2003. **278**(16): p. 14363-9.

141. Rodrigue-Gervais, I.G., et al., *Cellular inhibitor of apoptosis protein cIAP2 protects against pulmonary tissue necrosis during influenza virus infection to promote host survival*. Cell Host Microbe, 2014. **15**(1): p. 23-35.
142. Bertheloot, D., E. Latz, and B.S. Franklin, *Necroptosis, pyroptosis and apoptosis: an intricate game of cell death*. Cell Mol Immunol, 2021. **18**(5): p. 1106-1121.
143. Sauler, M., I.S. Bazan, and P.J. Lee, *Cell Death in the Lung: The Apoptosis-Necroptosis Axis*. Annu Rev Physiol, 2019. **81**: p. 375-402.
144. Hogner, K., et al., *Macrophage-expressed IFN-beta contributes to apoptotic alveolar epithelial cell injury in severe influenza virus pneumonia*. PLoS Pathog, 2013. **9**(2): p. e1003188.
145. Janssen, W.J., et al., *Fas determines differential fates of resident and recruited macrophages during resolution of acute lung injury*. Am J Respir Crit Care Med, 2011. **184**(5): p. 547-60.
146. Peteranderl, C., et al., *Macrophage-epithelial paracrine crosstalk inhibits lung edema clearance during influenza infection*. J Clin Invest, 2016. **126**(4): p. 1566-80.
147. Ekchariyawat, P., et al., *Apoptosis induced by avian H5N1 virus in human monocyte-derived macrophages involves TRAIL-inducing caspase-10 activation*. Innate Immun, 2012. **18**(3): p. 390-7.
148. Herold, S., et al., *Alveolar epithelial cells direct monocyte transepithelial migration upon influenza virus infection: impact of chemokines and adhesion molecules*. J Immunol, 2006. **177**(3): p. 1817-24.
149. Fujikura, D., et al., *Type-I interferon is critical for FasL expression on lung cells to determine the severity of influenza*. PLoS One, 2013. **8**(2): p. e55321.
150. Ware, C.F., *Targeting the LIGHT-HVEM pathway*. Adv Exp Med Biol, 2009. **647**: p. 146-55.
151. Steinberg, M.W., T.C. Cheung, and C.F. Ware, *The signaling networks of the herpesvirus entry mediator (TNFRSF14) in immune regulation*. Immunol Rev, 2011. **244**(1): p. 169-87.
152. del Rio, M.L., et al., *HVEM/LIGHT/BTLA/CD160 cosignaling pathways as targets for immune regulation*. J Leukoc Biol, 2010. **87**(2): p. 223-35.
153. Cai, H., et al., *Deficiency of LIGHT signaling pathway exacerbates Chlamydia psittaci respiratory tract infection in mice*. Microb Pathog, 2016. **100**: p. 250-256.
154. Stanley, A.C., et al., *Critical roles for LIGHT and its receptors in generating T cell-mediated immunity during Leishmania donovani infection*. PLoS Pathog, 2011. **7**(10): p. e1002279.
155. Hsieh, S.L. and W.W. Lin, *Decoy receptor 3: an endogenous immunomodulator in cancer growth and inflammatory reactions*. J Biomed Sci, 2017. **24**(1): p. 39.
156. Chen, W., et al., *Hematopoietic stem/progenitor cell differentiation towards myeloid lineage is modulated by LIGHT/LIGHT receptor signaling*. J Cell Physiol, 2018. **233**(2): p. 1095-1103.
157. Shui, J.W. and M. Kronenberg, *HVEM: An unusual TNF receptor family member important for mucosal innate immune responses to microbes*. Gut Microbes, 2013. **4**(2): p. 146-51.
158. Rooney, I.A., et al., *The lymphotoxin-beta receptor is necessary and sufficient for LIGHT-mediated apoptosis of tumor cells*. J Biol Chem, 2000. **275**(19): p. 14307-15.
159. Banach-Orlowska, M., et al., *Cholesterol restricts lymphotoxin beta receptor-triggered NF-kappaB signaling*. Cell Commun Signal, 2019. **17**(1): p. 171.
160. Heo, S.K., et al., *LIGHT (TNFSF14) Increases the Survival and Proliferation of Human Bone Marrow-Derived Mesenchymal Stem Cells*. PLoS One, 2016. **11**(11): p. e0166589.

161. Zhang, M.C., et al., *LIGHT sensitizes IFN-gamma-mediated apoptosis of HT-29 human carcinoma cells through both death receptor and mitochondria pathways*. Cell Res, 2004. **14**(2): p. 117-24.
162. del Rio, M.L., et al., *Immunotherapeutic targeting of LIGHT/LTbetaR/HVEM pathway fully recapitulates the reduced cytotoxic phenotype of LIGHT-deficient T cells*. MAbs, 2016. **8**(3): p. 478-90.
163. Otterdal, K., et al., *Platelet-derived LIGHT induces inflammatory responses in endothelial cells and monocytes*. Blood, 2006. **108**(3): p. 928-35.
164. del Rio, M.L., et al., *LIGHT/HVEM/LTbetaR interaction as a target for the modulation of the allogeneic immune response in transplantation*. Am J Transplant, 2013. **13**(3): p. 541-51.
165. Kinchen, J., et al., *Structural Remodeling of the Human Colonic Mesenchyme in Inflammatory Bowel Disease*. Cell, 2018. **175**(2): p. 372-386 e17.
166. Yuan, X., et al., *LIGHT is increased in patients with coronary disease and regulates inflammatory response and lipid metabolism in oxLDL-induced THP-1 macrophages*. Biochem Biophys Res Commun, 2017. **490**(3): p. 732-738.
167. Hsu, C.Y., et al., *Circulating TNFSF14 (Tumor Necrosis Factor Superfamily 14) Predicts Clinical Outcome in Patients With Stable Coronary Artery Disease*. Arterioscler Thromb Vasc Biol, 2019. **39**(6): p. 1240-1252.
168. Halvorsen, B., et al., *LIGHT/TNFSF14 is increased in patients with type 2 diabetes mellitus and promotes islet cell dysfunction and endothelial cell inflammation in vitro*. Diabetologia, 2016. **59**(10): p. 2134-44.
169. Otterdal, K., et al., *Increased Serum Levels of LIGHT/TNFSF14 in Nonalcoholic Fatty Liver Disease: Possible Role in Hepatic Inflammation*. Clin Transl Gastroenterol, 2015. **6**: p. e95.
170. Gindzienska-Sieskiewicz, E., et al., *Increased expression of the TNF superfamily member LIGHT/TNFSF14 and its receptors (HVEM and LTssR) in patients with systemic sclerosis*. Rheumatology (Oxford), 2019. **58**(3): p. 502-510.
171. Herro, R., et al., *LIGHT-HVEM signaling in keratinocytes controls development of dermatitis*. J Exp Med, 2018. **215**(2): p. 415-422.
172. Anand, S., et al., *Essential role of TNF family molecule LIGHT as a cytokine in the pathogenesis of hepatitis*. J Clin Invest, 2006. **116**(4): p. 1045-51.
173. Wang, W., et al., *Excess LIGHT contributes to placental impairment, increased secretion of vasoactive factors, hypertension, and proteinuria in preeclampsia*. Hypertension, 2014. **63**(3): p. 595-606.
174. Edwards, J.R., et al., *LIGHT (TNFSF14), a novel mediator of bone resorption, is elevated in rheumatoid arthritis*. Arthritis Rheum, 2006. **54**(5): p. 1451-62.
175. Kim, W.J., et al., *LIGHT is involved in the pathogenesis of rheumatoid arthritis by inducing the expression of pro-inflammatory cytokines and MMP-9 in macrophages*. Immunology, 2005. **114**(2): p. 272-9.
176. Mehta, A.K., et al., *Tumor necrosis factor family member LIGHT acts with IL-1beta and TGF-beta to promote airway remodeling during rhinovirus infection*. Allergy, 2018. **73**(7): p. 1415-1424.
177. Sedgmen, B.J., et al., *LIGHT is dispensable for CD4+ and CD8+ T cell and antibody responses to influenza A virus in mice*. Int Immunol, 2006. **18**(5): p. 797-806.
178. Seo, G.Y., et al., *LIGHT-HVEM Signaling in Innate Lymphoid Cell Subsets Protects Against Enteric Bacterial Infection*. Cell Host Microbe, 2018. **24**(2): p. 249-260 e4.

179. Okwor, I., et al., *Deficiency of CD40 Reveals an Important Role for LIGHT in Anti-Leishmania Immunity*. J Immunol, 2015. **195**(1): p. 194-202.
180. Doherty, T.A., et al., *The tumor necrosis factor family member LIGHT is a target for asthmatic airway remodeling*. Nat Med, 2011. **17**(5): p. 596-603.
181. Zhang, H., et al., *TNFSF14, a novel target of miR-326, facilitates airway remodeling in airway smooth muscle cells via inducing extracellular matrix protein deposition and proliferation*. Kaohsiung J Med Sci, 2020. **36**(7): p. 508-514.
182. Herro, R., et al., *Tumor necrosis factor superfamily 14 (LIGHT) controls thymic stromal lymphopoietin to drive pulmonary fibrosis*. J Allergy Clin Immunol, 2015. **136**(3): p. 757-68.
183. da Silva Antunes, R., et al., *TNFSF14 (LIGHT) Exhibits Inflammatory Activities in Lung Fibroblasts Complementary to IL-13 and TGF-beta*. Front Immunol, 2018. **9**: p. 576.
184. Kotani, T., et al., *Increased Serum LIGHT Levels Correlate with Disease Progression and Severity of Interstitial Pneumonia in Patients with Dermatomyositis: A Case Control Study*. PLoS One, 2015. **10**(10): p. e0140117.
185. Arunachalam, P.S., et al., *Systems biological assessment of immunity to mild versus severe COVID-19 infection in humans*. Science, 2020. **369**(6508): p. 1210-1220.
186. Perlin, D.S., et al., *Levels of the TNF-Related Cytokine LIGHT Increase in Hospitalized COVID-19 Patients with Cytokine Release Syndrome and ARDS*. mSphere, 2020. **5**(4).
187. Scheu, S., et al., *Targeted disruption of LIGHT causes defects in costimulatory T cell activation and reveals cooperation with lymphotoxin beta in mesenteric lymph node genesis*. J Exp Med, 2002. **195**(12): p. 1613-24.
188. Wang, Y., et al., *The role of herpesvirus entry mediator as a negative regulator of T cell-mediated responses*. J Clin Invest, 2005. **115**(3): p. 711-7.
189. Fütterer, A., et al., *The lymphotoxin beta receptor controls organogenesis and affinity maturation in peripheral lymphoid tissues*. Immunity, 1998. **9**(1): p. 59-70.
190. Gui, R. and Q. Chen, *Molecular Events Involved in Influenza A Virus-Induced Cell Death*. Front Microbiol, 2021. **12**: p. 797789.
191. Dong, H.P., et al., *Evaluation of cell surface expression of phosphatidylserine in ovarian carcinoma effusions using the annexin-V/7-AAD assay: clinical relevance and comparison with other apoptosis parameters*. Am J Clin Pathol, 2009. **132**(5): p. 756-62.
192. Wurzer, W.J., et al., *Caspase 3 activation is essential for efficient influenza virus propagation*. EMBO J, 2003. **22**(11): p. 2717-28.
193. Fritsch, M., et al., *Caspase-8 is the molecular switch for apoptosis, necroptosis and pyroptosis*. Nature, 2019. **575**(7784): p. 683-687.
194. He, B., et al., *Vascular targeting of LIGHT normalizes blood vessels in primary brain cancer and induces intratumoural high endothelial venules*. J Pathol, 2018. **245**(2): p. 209-221.
195. Sandberg, W.J., et al., *Inflammatory interaction between LIGHT and proteinase-activated receptor-2 in endothelial cells: potential role in atherogenesis*. Circ Res, 2009. **104**(1): p. 60-8.
196. He, W., et al., *Alveolar macrophages are critical for broadly-reactive antibody-mediated protection against influenza A virus in mice*. Nat Commun, 2017. **8**(1): p. 846.
197. Quantius, J., et al., *Influenza Virus Infects Epithelial Stem/Progenitor Cells of the Distal Lung: Impact on Fgfr2b-Driven Epithelial Repair*. PLoS Pathog, 2016. **12**(6): p. e1005544.
198. Seo, S.U., et al., *Type I interferon signaling regulates Ly6C(hi) monocytes and neutrophils during acute viral pneumonia in mice*. PLoS Pathog, 2011. **7**(2): p. e1001304.

199. Gaya, M., et al., *Initiation of Antiviral B Cell Immunity Relies on Innate Signals from Spatially Positioned NKT Cells*. *Cell*, 2018. **172**(3): p. 517-533 e20.
200. Schmit, T., et al., *Interferon-gamma promotes monocyte-mediated lung injury during influenza infection*. *Cell Rep*, 2022. **38**(9): p. 110456.
201. Atkin-Smith, G.K., et al., *The induction and consequences of Influenza A virus-induced cell death*. *Cell Death Dis*, 2018. **9**(10): p. 1002.
202. Husain, M. and K.S. Harrod, *Influenza A virus-induced caspase-3 cleaves the histone deacetylase 6 in infected epithelial cells*. *FEBS Lett*, 2009. **583**(15): p. 2517-20.
203. Muhlbauer, D., et al., *Influenza virus-induced caspase-dependent enlargement of nuclear pores promotes nuclear export of viral ribonucleoprotein complexes*. *J Virol*, 2015. **89**(11): p. 6009-21.
204. Wang, Y., et al., *Influenza Virus Infection Induces ZBP1 Expression and Necroptosis in Mouse Lungs*. *Front Cell Infect Microbiol*, 2019. **9**: p. 286.
205. Nguyen, T.Q., R. Rollon, and Y.K. Choi, *Animal Models for Influenza Research: Strengths and Weaknesses*. *Viruses*, 2021. **13**(6).
206. Califano, D., Y. Furuya, and D.W. Metzger, *Effects of Influenza on Alveolar Macrophage Viability Are Dependent on Mouse Genetic Strain*. *J Immunol*, 2018. **201**(1): p. 134-144.
207. Roubidoux, E.K. and S. Schultz-Cherry, *Animal Models Utilized for the Development of Influenza Virus Vaccines*. *Vaccines (Basel)*, 2021. **9**(7).
208. Alberts, R., et al., *Gene expression changes in the host response between resistant and susceptible inbred mouse strains after influenza A infection*. *Microbes Infect*, 2010. **12**(4): p. 309-18.
209. Cole, S.L., et al., *M1-like monocytes are a major immunological determinant of severity in previously healthy adults with life-threatening influenza*. *JCI Insight*, 2017. **2**(7): p. e91868.
210. Roquilly, A., et al., *Alveolar macrophages are epigenetically altered after inflammation, leading to long-term lung immunoparalysis*. *Nat Immunol*, 2020. **21**(6): p. 636-648.
211. Shotland, A.M., A.P. Fontenot, and A.S. McKee, *Pulmonary Macrophage Cell Death in Lung Health and Disease*. *Am J Respir Cell Mol Biol*, 2021. **64**(5): p. 547-556.
212. Wein, A.N., et al., *IL-36gamma Protects against Severe Influenza Infection by Promoting Lung Alveolar Macrophage Survival and Limiting Viral Replication*. *J Immunol*, 2018. **201**(2): p. 573-582.
213. Wendisch, D., et al., *SARS-CoV-2 infection triggers profibrotic macrophage responses and lung fibrosis*. *Cell*, 2021. **184**(26): p. 6243-6261 e27.
214. Schulte-Schrepping, J., et al., *Severe COVID-19 Is Marked by a Dysregulated Myeloid Cell Compartment*. *Cell*, 2020. **182**(6): p. 1419-1440 e23.
215. Szabo, P.A., et al., *Longitudinal profiling of respiratory and systemic immune responses reveals myeloid cell-driven lung inflammation in severe COVID-19*. *Immunity*, 2021. **54**(4): p. 797-814 e6.
216. Dagvadorj, J., et al., *Lipopolysaccharide Induces Alveolar Macrophage Necrosis via CD14 and the P2X7 Receptor Leading to Interleukin-1alpha Release*. *Immunity*, 2015. **42**(4): p. 640-53.
217. Huang, H.R., et al., *RIPK3 Activates MLKL-mediated Necroptosis and Inflammasome Signaling during Streptococcus Infection*. *Am J Respir Cell Mol Biol*, 2021. **64**(5): p. 579-591.
218. Cen, M., et al., *FBXO6 regulates the antiviral immune responses via mediating alveolar macrophages survival*. *J Med Virol*, 2022.

219. Mok, C.K.P., et al., *Differential onset of apoptosis in influenza A virus H5N1- and H1N1-infected human blood macrophages*. J Gen Virol, 2007. **88**(Pt 4): p. 1275-1280.
220. Chang, P., et al., *Early apoptosis of porcine alveolar macrophages limits avian influenza virus replication and pro-inflammatory dysregulation*. Sci Rep, 2015. **5**: p. 17999.
221. Mehrbod, P., et al., *The roles of apoptosis, autophagy and unfolded protein response in arbovirus, influenza virus, and HIV infections*. Virulence, 2019. **10**(1): p. 376-413.
222. Mok, C.K., et al., *Differential onset of apoptosis in influenza A virus H5N1- and H1N1-infected human blood macrophages*. J Gen Virol, 2007. **88**(Pt 4): p. 1275-80.
223. Nogusa, S., et al., *RIPK3 Activates Parallel Pathways of MLKL-Driven Necroptosis and FADD-Mediated Apoptosis to Protect against Influenza A Virus*. Cell Host Microbe, 2016. **20**(1): p. 13-24.
224. Ware, C.F., M. Croft, and G.A. Neil, *Realigning the LIGHT signaling network to control dysregulated inflammation*. J Exp Med, 2022. **219**(7).
225. Heo, S.K., et al., *LIGHT enhances the bactericidal activity of human monocytes and neutrophils via HVEM*. J Leukoc Biol, 2006. **79**(2): p. 330-8.
226. Granger, S.W. and S. Rickert, *LIGHT-HVEM signaling and the regulation of T cell-mediated immunity*. Cytokine Growth Factor Rev, 2003. **14**(3-4): p. 289-96.
227. Bechill, J. and W.J. Muller, *Herpesvirus entry mediator (HVEM) attenuates signals mediated by the lymphotoxin beta receptor (LTbetaR) in human cells stimulated by the shared ligand LIGHT*. Mol Immunol, 2014. **62**(1): p. 96-103.
228. Petreaca, M.L., et al., *Vascular endothelial growth factor promotes macrophage apoptosis through stimulation of tumor necrosis factor superfamily member 14 (TNFSF14/LIGHT)*. Wound Repair Regen, 2008. **16**(5): p. 602-14.
229. Herro, R. and M. Croft, *The control of tissue fibrosis by the inflammatory molecule LIGHT (TNF Superfamily member 14)*. Pharmacol Res, 2016. **104**: p. 151-5.
230. Mikami, Y., et al., *Lymphotoxin beta receptor signaling induces IL-8 production in human bronchial epithelial cells*. PLoS One, 2014. **9**(12): p. e114791.
231. Conlon, T.M., et al., *Inhibition of LTbetaR signalling activates WNT-induced regeneration in lung*. Nature, 2020. **588**(7836): p. 151-156.
232. Skeate, J.G., et al., *TNFSF14: LIGHTing the Way for Effective Cancer Immunotherapy*. Front Immunol, 2020. **11**: p. 922.
233. Zhang, M., L. Perrin, and P. Pardo, *A Randomized Phase I Study to Assess the Safety and Pharmacokinetics of the Subcutaneously Injected Anti-LIGHT Antibody, SAR252067*. Clin Pharmacol Drug Dev, 2017. **6**(3): p. 292-301.
234. Perlin, D.S., et al., *Randomized, double-blind, controlled trial of human anti-LIGHT monoclonal antibody in COVID-19 acute respiratory distress syndrome*. J Clin Invest, 2022. **132**(3).
235. Desai, P., et al., *The TNF Superfamily Molecule LIGHT Promotes the Generation of Circulating and Lung-Resident Memory CD8 T Cells following an Acute Respiratory Virus Infection*. J Immunol, 2018. **200**(8): p. 2894-2904.
236. Park, S.J., et al., *Herpesvirus Entry Mediator Binding Partners Mediate Immunopathogenesis of Ocular Herpes Simplex Virus 1 Infection*. mBio, 2020. **11**(3).
237. Xu, W., et al., *Transcriptome Sequencing Identifies Novel Immune Response Genes Highly Related to the Severity of Human Adenovirus Type 55 Infection*. Front Microbiol, 2019. **10**: p. 130.
238. Manresa, M.C., et al., *A Deficiency in the Cytokine TNFSF14/LIGHT Limits Inflammation and Remodeling in Murine Eosinophilic Esophagitis*. J Immunol, 2022.

239. Hirano, T., et al., *Abundant TNF-LIGHT expression in the airways of patients with asthma with persistent airflow limitation: Association with nitrative and inflammatory profiles*. *Respir Investig*, 2021. **59**(5): p. 651-660.
240. Bienkowska, J., et al., *Lymphotoxin-LIGHT pathway regulates the interferon signature in rheumatoid arthritis*. *PLoS One*, 2014. **9**(11): p. e112545.
241. Kou, Y.B., et al., *LIGHT (TNFSF14) inhibits glucose uptake of adipocytes by downregulating GLUT4 expression via AKT signaling pathway*. *Biochem Biophys Res Commun*, 2021. **583**: p. 106-113.
242. Herrero-Cervera, A., et al., *Genetic inactivation of the LIGHT (TNFSF14) cytokine in mice restores glucose homeostasis and diminishes hepatic steatosis*. *Diabetologia*, 2019. **62**(11): p. 2143-2157.
243. Jazowiecka-Rakus, J., et al., *Myxoma Virus Expressing LIGHT (TNFSF14) Pre-Loaded into Adipose-Derived Mesenchymal Stem Cells Is Effective Treatment for Murine Pancreatic Adenocarcinoma*. *Cancers (Basel)*, 2021. **13**(6).
244. Savage, A.K., et al., *Multimodal analysis for human ex vivo studies shows extensive molecular changes from delays in blood processing*. *iScience*, 2021. **24**(5): p. 102404.
245. Zhang, J., et al., *Two waves of pro-inflammatory factors are released during the influenza A virus (IAV)-driven pulmonary immunopathogenesis*. *PLoS Pathog*, 2020. **16**(2): p. e1008334.
246. Haljasmagi, L., et al., *Longitudinal proteomic profiling reveals increased early inflammation and sustained apoptosis proteins in severe COVID-19*. *Sci Rep*, 2020. **10**(1): p. 20533.
247. Tan, Y., et al., *Integrating longitudinal clinical laboratory tests with targeted proteomic and transcriptomic analyses reveal the landscape of host responses in COVID-19*. *Cell Discov*, 2021. **7**(1): p. 42.
248. Qu, H.Q., et al., *Circulating LIGHT (TNFSF14) and Interleukin-18 Levels in Sepsis-Induced Multi-Organ Injuries*. *Biomedicines*, 2022. **10**(2).
249. Macias, A.E., et al., *The disease burden of influenza beyond respiratory illness*. *Vaccine*, 2021. **39** Suppl 1: p. A6-A14.
250. Tam, V.C., et al., *PPARalpha exacerbates necroptosis, leading to increased mortality in postinfluenza bacterial superinfection*. *Proc Natl Acad Sci U S A*, 2020. **117**(27): p. 15789-15798.
251. Cipolla, E.M., B.R. Huckestein, and J.F. Alcorn, *Influenza sequelae: from immune modulation to persistent alveolitis*. *Clin Sci (Lond)*, 2020. **134**(13): p. 1697-1714.
252. Karwelat, D., et al., *Influenza virus-mediated suppression of bronchial Chitinase-3-like 1 secretion promotes secondary pneumococcal infection*. *FASEB J*, 2020. **34**(12): p. 16432-16448.
253. Okamoto, S., et al., *Influenza A virus-infected hosts boost an invasive type of Streptococcus pyogenes infection in mice*. *J Virol*, 2003. **77**(7): p. 4104-12.
254. Roquilly, A., et al., *Local Modulation of Antigen-Presenting Cell Development after Resolution of Pneumonia Induces Long-Term Susceptibility to Secondary Infections*. *Immunity*, 2017. **47**(1): p. 135-147 e5.
255. Shirey, K.A., et al., *Influenza "Trains" the Host for Enhanced Susceptibility to Secondary Bacterial Infection*. *mBio*, 2019. **10**(3).
256. Neupane, A.S., et al., *Patrolling Alveolar Macrophages Conceal Bacteria from the Immune System to Maintain Homeostasis*. *Cell*, 2020. **183**(1): p. 110-125 e11.

257. Verma, A.K., et al., *Influenza Infection Induces Alveolar Macrophage Dysfunction and Thereby Enables Noninvasive Streptococcus pneumoniae to Cause Deadly Pneumonia*. J Immunol, 2020.
258. Gopal, R., et al., *STAT2 Signaling Regulates Macrophage Phenotype During Influenza and Bacterial Super-Infection*. Front Immunol, 2018. **9**: p. 2151.
259. Bansal, S., et al., *IL-1 Signaling Prevents Alveolar Macrophage Depletion during Influenza and Streptococcus pneumoniae Coinfection*. J Immunol, 2018. **200**(4): p. 1425-1433.

9. Supplement

List of Figures

Figure 1. Depiction of the successive waves of fetal hematopoiesis.	9
Figure 2. Composition of the TR-AM pool during life.	12
Figure 3. Different pathophysiological mechanisms contribute to ARDS pathology.	14
Figure 4. Influenza A virion structure.	17
Figure 5. Replication cycle of influenza virus in the lung epithelium.	18
Figure 6. IV-induced pneumonia is characterized by a complex intra-alveolar inflammatory response.	22
Figure 7. Post-influenza TR-AM depletion enables the establishment of secondary bacterial pneumonia.	26
Figure 8. Apoptosis can be the endpoint of the intrinsic, extrinsic, or granzyme-associated programmed cell death pathway.	28
Figure 9. Depiction of TNFSF14/LIGHT and TNFSF14/LIGHT receptor signaling in lymphoid cells.	31
Figure 10. Pre-existing IAV pneumonia enables the establishment of post-influenza pneumococcal pneumonia.	53
Figure 11. Gating strategy for flow cytometry analysis of different immune cell populations in the BALF and lung tissue over the course of IAV-induced pneumonia.	55
Figure 12. Kinetics of different immune cell populations in the BALF of infected mice over the course of IAV infection.	57
Figure 13. Kinetics of immune cell populations in lavaged lungs (A-L) of infected mice over the course of IAV infection.	58
Figure 14. TR-AM depletion can occur independently of direct viral infection upon IAV-induced pneumonia.	60
Figure 15. Flow cytometry analysis of Annexin V⁺ 7-AAD⁻ TR-AM over the course of IAV infection.	61
Figure 16. TR-AM death in IAV-induced pneumonia is linked to caspase-dependent apoptosis.	62
Figure 17. Apoptosis inhibition attenuates TR-AM depletion upon IAV-induced pneumonia.	64

Figure 18. Gene expression analysis of flow-sorted TR-AM reveals an upregulation of various members of the <i>tnfsf</i> after IAV infection.	66
Figure 19. <i>Tnfsf14</i>/Light receptors on TR-AM follow distinct expression kinetics upon IAV-induced pneumonia.	68
Figure 20. Pulmonary <i>tnfsf14</i>/light levels increase during the course of IAV-induced pneumonia.	70
Figure 21. Treatment with r<i>Tnfsf14</i>/Light drives TR-AM apoptosis upon IAV infection. ...	71
Figure 22. Orotracheal administration of r<i>Tnfsf14</i>/Light aggravates TR-AM loss on day 3 pi.	72
Figure 23. Loss of <i>tnfsf14</i>/light preserves the TR-AM pool over the course of IAV infection.	73
Figure 24. Gene expression analysis of flow-sorted wild-type and <i>tnfsf14</i>^{-/-} TR-AM over the course of IAV infection.	75
Figure 25. Characterization of the injury degree and the inflammatory response of wild-type and <i>tnfsf14</i>^{-/-} mice following IAV infection.	79
Figure 26. Cytokine profile as measured in the BALF of wild-type and <i>tnfsf14</i>^{-/-} mice on day 7 pi per multiplex analysis.	80
Figure 27. Post-influenza clinical score is improved in <i>tnfsf14</i>^{-/-} mice compared to wild-type mice.	81
Figure 28. Therapeutic blocking of <i>tnfsf14</i>/light attenuates TR-AM loss upon IAV infection.	82
Figure 29. Neutrophils are the main cellular source of <i>tnfsf14</i>/light upon IAV infection.	86
Figure 30. Neutrophil depletion can be achieved by systemic antibody administration in IAV-infected mice.	87
Figure 31. Neutrophil depletion attenuates TR-AM loss on day 7 pi post-IAV infection.	88
Figure 32. <i>Ltβr</i>^{-/-} but not <i>tnfsf14</i>^{-/-} mice are characterized by an attenuated TR-AM loss upon IAV infection.	90
Figure 33. Loss of <i>tnfsf14</i>/light is linked to an improved clinical outcome upon IAV and <i>Spn</i> co-infection.	92
Figure 34. Synopsis of proposed mechanism of TR-AM death upon IAV-induced pneumonia.	102

List of Tables

Table 1. Experimental scoring for <i>in vivo</i> experiments.	34
Table 2. Staining protocol for TR-AM sorting:	41
Table 3. Primer pairs used for qPCR.....	45
Table 4. Staining protocol for immune and structural cell population analysis from BALF and lung tissue.....	49

Materials

Chemicals and consumables

Chemical/consumable	Manufacturer
Acridine orange (AO)/4',6-diamidino-2-phenylindole (DAPI) dye (Solution 18)	ChemoMetec, Allerød (DEN)
Atropin	B.Braun, Melsungen (GER)
Avicel	AMC-Biopolymers, Brussels (BEL)
Blood agar plates with sheep blood	Oxoid, Munich (GER)
BSA	Sigma-Aldrich, Taufkirchen (GER)
Calcium chloride	Sigma-Aldrich, Taufkirchen (GER)
Cell culture flasks 75cm ²	Greiner, Nürtingen (GER)
Cell culture plates, single- and multi- well	Greiner, Nürtingen (GER)
Cell nylon filters 20µM	Merck Millipore, Darmstadt (GER)
Cell strainer filters 40 and 100µm	BD Biosciences, San Jose (USA)
Clodronate liposomes and control liposomes	Liposoma, Amsterdam (NL)
DAPI	Life Technologies, Carlsbad (USA)
DEAE dextran	Thermo Scientific, Waltham (USA)
DMEM	Gibco BRL, Karlsruhe (GER)
DMSO	Sigma-Aldrich, Taufkirchen (GER)
dNTPs	Thermo Scientific, Waltham (USA)
EDTA	Roth, Karlsruhe (GER)
Ethanol	Sigma-Aldrich, Taufkirchen (GER)
FCS	Life Technologies, Carlsbad (USA)

Gamunex-C	Grifols, Los Angeles (USA)
GentleMACS C tubes	Miltenyi Biotec, Bergisch Gladbach (GER)
Hamilton® RN syringe	Hamilton Company, Reno (USA)
HBSS	Gibco BRL, Karlsruhe (GER)
HEPES	Merck Millipore, Darmstadt (GER)
Horse serum	Sigma-Aldrich, Taufkirchen (GER)
Inoculation loops, sterile	Roth, Karlsruhe (GER)
Ketamin hydrochloride (Ketavet)	Pharmacia & Upjohn, Peapack (USA)
L-glutamine [200mM]	Gibco BRL, Karlsruhe (GER)
Magnesium sulfate	Sigma-Aldrich, Taufkirchen (GER)
Parafilm	American National, Greenwich (USA)
Paraformaldehyde	Merck Millipore, Darmstadt (GER)
PBS	Life Technologies, Carlsbad (USA)
PBS ⁺⁺ (containing MgCl)	PAN-Biotech, Aidenbach (GER)
Penicillin/streptomycin [5000 U/ml]	Gibco BRL, Karlsruhe (GER)
pHrodo™ Green <i>E. coli</i> BioParticles™ Phagocytosis Kit for Flow Cytometry	Invitrogen, Waltham (USA)
PMMA kuvettes	Merck Millipore, Darmstadt (GER)
Polystyrene round-bottom tubes 5ml	BD Biosciences, San Jose (USA)
Potassium chloride	Sigma-Aldrich, Taufkirchen (GER)
Protein concentrators, cut-off 3kDa	Thermo Scientific, Waltham (USA)
Reaction tubes 0.5ml and 1.5ml	Eppendorf, Hamburg (GER)
RPMI	Gibco BRL, Karlsruhe (GER)
Sandoglobulin	Novartis, Basel (CH)
Sodium azide	Roth, Karlsruhe (GER)
Sodium chloride	Roth, Karlsruhe (GER)
Sodium hydrogen carbonate	Sigma-Aldrich, Taufkirchen (GER)
SYBR Green I	Life Technologies, Carlsbad (USA)
SYBR ROX	Qiagen, Hilden (GER)

Syringe 10ml and 20ml	Braun, Melsungen (GER)
Sytox™ blue	Thermo Scientific, Waltham (USA)
Todd-Hewitt broth	Sigma-Aldrich, Taufkirchen (GER)
Triton-X-100	Roth, Karlsruhe (GER)
True Blue™ Peroxidase Substrate	PKL, Gaithersburg (USA)
Tween 80	Sigma-Aldrich, Taufkirchen (GER)
Xylazine hydrochloride (Rompun)	Bayer AG, Leverkusen (GER)
Yeast extract	Sigma-Aldrich, Taufkirchen (GER)
aMEM	Gibco BRL, Karlsruhe (GER)

Reaction kits

Caspase-Glo® 3/7 Assay System	Promega, Madison (USA)
Caspase-Glo® 8 Assay System	Promega, Madison (USA)
RT ² PreAMP cDNA Synthesis Kit	Qiagen, Hilden (GER)
RT ² Profiler™ PCR Array and Primer Mix Mouse Antibacterial Response	Qiagen, Hilden (GER)
RT ² Profiler™ PCR Array and Primer Mix Mouse Cell Death PathwayFinder	Qiagen, Hilden (GER)
RT ² Profiler™ PCR Array and Primer Mix Mouse TNF Signaling Pathway	Qiagen, Hilden (GER)

Enzymes, recombinant proteins, and inhibitors

Enzyme/recombinant protein/inhibitor	Manufacturer
Accutase	Corning Life Sciences, Tewksbury (USA)
Dispase	Corning Life Sciences, Tewksbury (USA)
DNase I	Serva, Heidelberg (GER)
human recombinant TNFSF14/LIGHT	R&D Systems, Minneapolis (USA)
mouse recombinant tnfsf14/light	R&D Systems, Minneapolis (USA)
MLV-RT	Life Technologies, Carlsbad (USA)
Trypsin-EDTA	Merck Millipore, Darmstadt (GER)

Trypsin-TPCK	Worthington Biochemical, Lakewood (USA)
Z-DEVD-FMK caspase-3 inhibitor	R&D Systems, Minneapolis (USA)
Z-IETD-FMK caspase-8 inhibitor	R&D Systems, Minneapolis (USA)

Antibodies

Antibody	Manufacturer
CD11b FITC, Pacific Blue (clone M1/70)	BioLegend, San Diego (USA)
CD11c FITC, PE/Cy7 (clone N418)	BioLegend, San Diego (USA)
CD19 PE (clone 6D5)	BioLegend, San Diego (USA)
CD206 APC (clone C068C2)	BioLegend, San Diego (USA)
CD24 PE/Cy7 (clone M1/69)	BioLegend, San Diego (USA)
CD270 HVEM PE (clone HMHV-1B18)	BioLegend, San Diego (USA)
CD3e FITC (clone 500A2)	BioLegend, San Diego (USA)
CD45 PE, PE/Cy7, APC/Cy7, FITC, APC (clone 30-F11)	BioLegend, San Diego (USA)
Goat polyclonal to influenza A Virus (clone ab20841)	Abcam, Cambridge (UK)
	Invitrogen, Carlsbad (USA)
Goat anti-Rabbit IgG (H+L) Secondary Antibody, HRP	Thermo Scientific, Waltham (USA)
Influenza A virus nucleoprotein (NP)	Kindly provided by the group of Professor Stephan Pleschka, Justus Liebig University of Giessen, Giessen (GER)
Isotype IgG2a anti-trinitrophenol 2A3	BioXCell, Lebanon (USA)
Isotype IgG2b, κ , clone MPC-11	BioLegend, San Diego (USA)
Light blocking antibody	Kindly provided by the group of Professor Jose Ignacio Rodríguez Barbosa, University of León, León (ES)
Lymphotoxin beta receptor antibody APC (clone 5G11)	BioLegend, San Diego (USA)

Ly-6G (clone 1A8)	BioXCell, Lebanon (USA)
Ly-6G APC (clone 1A8)	BioLegend, San Diego (USA)
Ly-6G/Ly-6C (Gr-1) PE/Cy7 (clone RB6-8C5)	BioLegend, San Diego (USA)
NK1.1 APC (clone PK136)	BD Biosciences, San Jose (USA)
SiglecF PE, BV421 (clone E50-2440)	BD Biosciences, San Jose (USA)

ELISA and Multiplex kits

ELISA/multiplex kit	Manufacturer
Human TNSF14/LIGHT, detection limit 16.5 pg/ml	R&D Systems, Minneapolis (USA)
Mouse tnfsf14/light, detection limit 250 pg/ml	R&D Systems, Minneapolis (USA)
xMAP® multiplex kit for GM-CSF, IL-1b, IL-4, IL-6, IL-10, IFN γ , KC, MCP-1, MIP-1a, MIP-1b, RANTES, TNF- α	Luminex, Austin (USA)

List of Abbreviations

5'-PPP	5' triphosphorylated
7-AAD	7-aminoactinomycin D
a	anti
Ad tr	Adoptive transfer
AEC	Alveolar epithelial cells
ANOVA	Analysis of variance
AO	Acridine orange
APC	Allophycocyanin
ARDS	Acute Respiratory Distress Syndrome
ATPase	Adenosintriphosphatase
BACH2	B lymphoid transcriptional repressor broad complex-tramtrack-bric á brac and Cap'n'collar homology 2
BALF	Bronchoalveolar lavage fluid
BALT	Bronchus-associated lymphoid tissue
BCL-2	B cell lymphoma 2
BID	BH3-interacting domain death agonist
BMDM	Bone marrow-derived macrophages
BSA	Bovine serum albumin
BTLA	B and T lymphocyte attenuator
BV	Brilliant violet
°C	Celsius
Ca	Calcium
Caspase	Cysteine-aspartic protease
CaspI	Caspase inhibitor
CCK-8	Cell counting kit-8
CCL-2	C-C motif chemokine ligand 2
CCR-2	C-C motif chemokine receptor 2
CD	Cluster of differentiation
cDNA	Complementary DNA

cFLAR	Casp8 and FADD-like apoptosis regulator
Cfu	Colony forming units
Cl	Chloride
cm	Centimeter
c-Maf	V-maf musculoaponeurotic fibrosarcoma oncogene homolog
CO ₂	Carbon dioxide
COVID-19	Coronavirus-induced disease 2019
CXCL10	C-X-C motif chemokine ligand 10
DAB	3,3-diaminobenzidine
DAPI	4',6-diamidino-2-phenylindole
DCs	Dendritic cells
dCt	Delta Ct
DEVD	Asp-Glu-Val-Asp
dH ₂ O	Deionized water
DAMP	Danger-associated molecular pattern
DcR3	Decoy receptor 3
DEAE	Diethylaminoethyl
DIABLO	Direct IAP binding protein with low pI
DISC	Death-inducing signaling complex
DMEM	Dulbecco's modified Eagle's medium
DMSO	Dimethylsulfoxide
DNA	Desoxyribonucleic Acid
dNTP	Desoxynucleosidtriphosphate
dpi	Days post infection
DR5	Death receptor 5
dsRNA	Double stranded RNA
DTT	Dithiotreitol
ECDC	European Center for Disease Control
EDTA	Ethylendinitrilotetraacetic acid
ELISA	Enzyme Linked Immunosorbent Assay

EMPs	Erythro-myeloid precursors
EpCAM	Epithelial cell adhesion molecule
FACS	Fluorescence-activated cell sorting
FADD	FS-7-associated surface antigen (Fas)-associated protein with death domain
FasL	Fas ligand
FCS	Fetal calf serum
FFU	Foci forming units
FiO ₂	Fraction of inspired oxygen
FITC	Fluorescein-5-isothiocyanate
FP	Forward primer
FSC-A	Forward scatter- area
FSC-H	Forward scatter- height
G	Gauge
g	G-force
GAPDH	Glyceraldehyde-3-Phosphate Dehydrogenase
gr	Gramms
GFP	Green fluorescent protein
GM-CSF	Granulocyte-macrophage colony-stimulating factor
h	Hours
H ₂ O ₂	Hydrogen peroxide
HA	Hemagglutinin
HBSS	Hank's buffered salt solution
HE	Hematoxylin and eosin
HEPES	4-(2-hydroxyethyl)-1-piperazineethanesulfonic acid
HRP	Horseradish peroxidase
HSC	Hematopoietic stem cells
HVEM	Herpesvirus entry mediator
IETD	Ile-Glu-Thr-Asp
IFN	Type I interferon
IFN α	Interferon alpha

IFN β	Interferon beta
IFN γ	Interferon gamma
IHC	Immunohistochemistry
IL	Interleukin
Ig	Immunoglobulin
IAV	Influenza A virus
ILC	Innate lymphoid cells
IM	Interstitial macrophages
in	Intranasally
ip	Intraperitoneally
IRF	Interferon regulatory factor
IVC	Individually ventilated cages, conventional
it	Orotracheally
IU	International units
K	Potassium
KC	Keratinocyte chemoattractant
kDa	Kilodalton
Kg	Kilogram
l	Liter
LH	Lung homogenate
LIGHT	Homologous to lymphotoxin, exhibits inducible expression and competes with HSV glycoprotein D for binding to herpesvirus entry mediator, a receptor expressed on T lymphocytes
LT α	Lymphotoxin alpha
LT β R	Lymphotoxin beta receptor
Ly6C	Lymphocyte antigen 6 complex, locus C
Ly6G	Lymphocyte antigen 6 complex, locus G6D
m	Milli
M	Molar
M1	Matrix protein 1

M2	Matrix protein 2
mAb	Murine antibody
MARCO	Macrophage receptor with collagenous structure
MAVS	Mitochondrial antiviral signaling proteins
MC	Mesenchymal cells
MCP-1	Monocyte chemotactic protein 1
M-CSF	Colony-stimulating factor 1
MDCK	Madin Darbey Canine Kidney
MEM	Minimal Essential Medium
Mertk	Proto-oncogene tyrosine-protein kinase MER
MgCl ₂	Magnesium chloride
min	Minute
MIP	Macrophage inflammatory protein
MLKL	Mixed lineage kinase domain-like
mol	Mol
MOI	Multiplicity of infection
MoMf	Monocytes/Macrophages
MPTP	Mitochondrial permeability transition pore
mRNA	Messenger RNA
Myb	Myeloblastosis proto-oncogene
n	Nano
Na	Sodium
NA	Neuraminidase
NaAz	Sodium azide
NaCl	Sodium chloride
NaHCO ₃	Sodium bicarbonate
NCTC	National Collection of Type Cultures
NF-κB	Nuclear factor kappa beta
NK	Natural killer
NO	Nitric oxide

NOD	Nucleotide-binding oligomerization domain-containing protein
NP	Nucleocapsid protein
NS-1	Non-structural protein 1
NS-2	Non-structural protein 2
nt	Nucleotide
OD	Optical density
PA	Polymerase protein, acidic
PAMP	Pathogen-associated molecular pattern
PaO ₂	Partial pressure of oxygen at sea level
PAP	Pulmonary alveolar proteinosis
PARP-1	Poly-ADP-ribose (PAR) polymerase 1
PB	Pacific blue
PB1	Polymerase protein basic 1
PB2	Polymerase protein basic 2
PBMCs	Peripheral blood mononuclear cells
PBS	Phosphate buffered saline
PCA	Principal component analysis
pCO ₂	Partial pressure carbon dioxide
PCR	Polymerase chain reaction
PDGF	Platelet-derived growth factor
PE	Phycoerythrin
PEEP	Positive end-expiratory pressure
PerCP Cy5.5	Peridinin chlorophyll cyanine 5.5
PFA	Paraformaldehyde
pfu	Plaque forming units
pH	Potentia hydrogenii
PI	Propidium iodide
pi	Post infectionem
PLET1	Placenta expressed transcript 1

PMMA	Polymethyl methacrylate
pO ₂	Partial pressure oxygen
PPAR- γ	Peroxisome proliferator-activated receptor γ
P-Sp	Para-aortic splachnopleura
PR8	Influenza virus A/Puerto Rico/8/34 (H1N1)
qRT-PCR	Quantitative real time polymerase chain reaction
r	Recombinant
RANTES	Regulated on activation, normal T cell expressed and secreted
RIG-I	Retinoic acid inducible gene-I
RIP-1	Receptor-interacting serine/threonine-protein kinase 1
RLU	Relative light units
ROS	Reactive oxygen species
RP	Reverse primer
RNA	Ribonucleic acid
RNP	Ribonucleoprotein
rpm	Rounds per minute
RSV	Respiratory syncytial virus
RT	Room temperatue
s	Seconds
SA	Sialic acid
SARS-CoV-2	Severe acute respiratory stress syndrome coronavirus 2
SEM	Standard error of the mean
SMAC	Second mitochondria-derived activator of caspases
SP-A	Surfactant protein A
SP-D	Surfactant protein D
SPF	Specific pathogen-free
<i>Spn</i>	<i>Streptococcus pneumoniae</i>
SSC-A	Side scatter-area
TGF- β	Transforming growth factor beta

THY	Todd-Hewitt Broth powder/yeast extract
TLR	Toll-like receptors
TNF- α	Tumor necrosis factor alpha
TNF(R)SF	Tumor necrosis superfamily (receptor)
TPCK	Tosyl phenylalanyl chloromethyl ketone
TRAF	TNF receptor-associated factors
TRAIL	TNF-related apoptosis-inducing ligand
TR-AM	Tissue-resident alveolar macrophages
U	Units
Umap	Uniform manifold approximation and projection for dimension reduction
VEGF	Vascular endothelial growth factor
WST-8	2-(2-methoxy-4-nitrophenyl)-3-(4-nitrophenyl)-5-(2,4-disulfophenyl)-2H-tetrazolium
wt	Wild-type
XIAP	X-linked inhibitor of apoptosis protein
YS	Yolk sac
Zeb2	Zinc finger E box binding homeobox 2
μ	Micro

Affirmation

I declare that I have completed this dissertation single-handedly without the unauthorized help of a second party and only with the assistance acknowledged therein. I have appropriately acknowledged and referenced all text passages that are derived literally from or are based on the content of published or unpublished work of others, and all information that relates to verbal communications. I have abided by the principles of good scientific conduct laid down in the charter of the Justus Liebig University of Giessen in carrying out the investigations described in the dissertation.

Place, Date

Original Signature

Curriculum vitae

Acknowledgements

I am glad you are here with me. Here at the end of all things. `

J.R.R. Tolkien, *The Return of the King*.

I would like to thank my supervisor, Prof. Susanne Herold, for giving me the opportunity to enter the world of basic research, while simultaneously supporting my growth as an Infectious Diseases clinician scientist. Her work ethic, unyielding scientific interest, and masterful grasp of both worlds of research and clinic set the standards I measure my progress by. My gratitude to Prof. Lohmeyer, who remembered the interest I had expressed in doing science during my fresh-from-the-university interview back in the day and offered me a PhD project despite my lack of previous research experience. Thank you for entrusting me your patients and your scientific questions.

Many thanks to Christin Peteranderl for her immense patience, kind words, and tireless guidance. You believed in this project before it took shape and saw its potential when my impatient nature could not. Thank you for teaching me not only scientific methods but also scientific etiquette.

To all my lab mates who have borne witness to struggles, successes, countless experimental hours, and endless writing sessions, I would not have been able to do this without your help and moral support. Margarida Barroso, Theresa Schäfer, Mohammad Estiri, Julian Better, I am proud to be sharing the office, the sweets, and the tea with you. Ana Ivonne Vazquez-Armendariz, Irina Kuznetsova, Learth Oruqaj-Pervizaj, Monika Heiner, it is comforting to know that the best advice one can get, the funniest jokes, and of course, a lifesaving FlowJo dongle, are always one door away. Martin Langelage, Michael Wettstein, Anna-Lena Ament, Marie Heßler, Blanche Nganko, Julia Bespalowa, it's a privilege to have worked with all of you.

To our wonderful technicians, Stefanie Jarmer, Larissa Hamann, Florian Lück, Julia Stark, Maria Gross, Josephine Guth, I am humbled by your continuous support both inside and outside the lab. You offer so much more than technical assistance. You are the stronghold of our lab.

To my friends and colleagues at IBioBA, Buenos Aires, Balachandar Selvakumar and Maximiliano Ferrero, all the scientific and technical staff there, I am truly grateful that through your tireless efforts this work was made possible.

Special thanks to my MBML mates and friends from other working groups here at UGMLC for sharing the PhD experience with me, offering valuable scientific input, and showing me the fun

part of science. Stefan Hadzic, Ettore Lignelli, Cheng Yu-Wu, Andrés Alberro-Brage, Despina Myti, I wish you the best in all your scientific endeavors.

To my colleagues in the clinic, those who are still there, and those who had been, I am most grateful to you for holding the castle when I'm away trying to figure out a tiny part of the biology behind the diseases you treat. Vera Kantelhardt, Ulla Albrecht, Arne Appunn, Shahadat Hossain, you are great doctors and amazing people to work with. To my consultants, Thomas Discher, Janina Trauth, Ulrich Matt, you are constant sources of knowledge and inspiration, and each one of you is a role model I never cease to learn from.

It is hard to find suitable words to thank my friends here in Giessen and in Greece for their support since day one. Vassia Bariami, Eleni Tzima, Olga Sideri, Antigoni Michalopoulou, Vangelis Pavlakis, Katherina Gavrielatou, Petros Stathopoulos, Anna Kalfountzou, Kostas Panagiotidis, Father Arsenios Karatzas, you are no friends. You are family.

To my parents, Fotios, and Eleni, my sister Eleftheria, my aunt Vassiliki, my godmother Aikaterini, a mere thanks is not enough to express my gratitude for your love, your trust in my decisions and abilities even when I doubt them myself, your discreet reassurance you are always there for me, your patience, and your prayers. Everything I have accomplished so far; all I aspire to be and do is because of you. I love and cherish you all.

Τέλος και τω Θεώ δόξα.